Optimization of two-photon excited fluorescence for volumetric imaging

Pubudu Thilanka Galwaduge

Submitted in partial fulfillment of the
requirements for the degree of
Doctor of Philosophy
in the Graduate School of Arts and Sciences

COLUMBIA UNIVERSITY

2017

ABSTRACT

Optimization of two-photon excited fluorescence for volumetric imaging

Pubudu Thilanka Galwaduge

Two-photon microscopy is often used in biological imaging due to its optical sectioning and depth penetration capabilities. These characteristics have made two-photon microscopy especially useful for neurobiological studies where imaging a volume at single cell resolution is typically required. This dissertation focuses on the optimization of two-photon excited fluorescence for volumetric imaging of biological samples, with special attention to imaging the mouse brain.

Chapter 2 presents wavefront manipulation as a way of optimizing two-photon excited fluorescence. We show, through numerical simulations and experiments, that the magnitude of the two-photon fluorescence signal originating from cell-sized objects can be used as a metric of beam quality. We also show that the cranial window used in mouse experiment is a major source of aberrations, which can readily be represented in the Zernike basis. Finally, we implement a modal wavefront optimization scheme that optimizes the wavefront based entirely on the magnitude of the fluorescence. Along with this scheme, Zernike functions are found to be a useful basis for correcting aberrations encountered in mouse brain imaging while the Hadamard basis is found to be useful for scattering compensation. Corrections performed in mouse brain using Zernike functions are found to be useful over hundreds of microns, allowing a single correction to be applied to a whole volume. Finally, we show that the wavefront correction system can double as a wavefront encoding system for experiments that require custom point-spread-functions.

Chapter 3 presents work that aims to significantly improve the volume imaging rate of two-photon microscopy. The imaging speed is improved by combining two-photon excitation with scanning confocally-aligned planar excitation microscopy (SCAPE). Numerical simulations, analytical arguments, and experiments reveal that the standard method of combining nano-joule pulses with 80 MHz repetition rates is inadequate for two-photon light-sheet excitation. We use numerical simulations and experiments to explore the possibility of achieving fast volumetric imaging using axial line and sheet excitation. Given that two-photon excitation requires high photon-flux-densities near the focus, achieving high enough fluorescence has to be balanced with restrictions placed by saturation, photodamage, photobleaching and sample heating effects. Finally, we experimentally study light sheet excitation at various pulse repetition rates with femtosecond pulses and find that repetition rates near 100 kHz allow imaging of nonbiological samples of ~200x300x300 μm^3 volume at 20 volumes per second while balancing the above constraints. This work paves the way for achieving fast, volumetric two-photon imaging of the mouse brain.

Table of Contents

List of Figures

List of Tables

Acknowledgements

I would like to express my gratitude towards my advisor, Prof. Elizabeth Hillman for providing me with the opportunity of joining her laboratory and providing years of support in turning ideas into meaningful projects.

Professors Irving Herman and Nanfang Yu for providing useful comments during the planning of the dissertation.

Lauren Grosberg and Matthew Bouchard for the training they provided during my first years.

Sharon Kim for her part in the many experiments we performed together, and also for helping proof-read this dissertation.

Venkatakaushik Voleti for sharing his knowledge on setting up off-axis experiments.

Hang Yu for his contributions in light-sheet experiments.

Teresa Zhao and Kripa Patel for proof-reading this dissertation.

Mohammed Shaik and Ying Ma for their support both in deed and spirit.

Other members of the lab who have been supportive over the years.

My family for their support through the years.

Michael Maikowski of Spectra Physics for sharing his expertise and lending support with laser systems.

Background

1.1 Introduction

Optical microscopy has historically been a sought after technology by biologists. While wide-field microscopes are still used extensively today in research settings, other types of microscopes that utilize linear and nonlinear excitation processes, such as confocal and two-photon laser scanning microscopy are now commonplace in neurobiology labs.

The popularity of optical microscopes is the result of their ability to provide sub-cellular resolution along with a wide array of contrast mechanisms. One of the commonly used contrast mechanisms used in microscopy is fluorescence. There is an active community of researchers developing both fluorescent probes as well as improved microscopes to image them. The popularity of fluorescence as a contrast mechanism is due to several reasons. For one, many biological samples contain chemical species that have inherent fluorescent contrast [1]. Secondly, for cases where such intrinsic contrast is not present, it is possible to introduce external contrast agents during in-vivo experiments [2]. In many cases, it is now common to use genetically encoded fluorescent proteins to study the structure as well as the function of the brain. The development of fluorescent probes that change fluorescence as result of Calcium activity [3, 4] or electric potential changes [5] now allows fluorescence imaging of neuronal activity in in-vivo settings. Given the utility of microscopy, there is merit in studying their optimization. This dissertation explores the optimization of two aspects of two photon microscopy – wavefront optimization and pulse energy optimization.

Chapter 1 introduces the fundamentals of microscopy and two-photon excitation, with special attention to various ray and wave models that will be utilized throughout the rest of this work.

Chapter 2 introduces wavefront error as a source of sub-optimal performance in two-photon microscopy. Numerical simulations are used to quantify the wavefront error expected during mouse brain experiments and the simulations are used to develop an experimental method of wavefront correction. The method proposed utilizes the properties of two-photon excited fluorescence to perform wavefront optimization without any direct or indirect wavefront measurements.

Chapter 3 introduces the speed-limitations of point-scanning two-photon microscopy in the context of limitations of the fluorophores as well as hardware parameters. This is followed by numerical simulations and experimental results demonstrating the advantage of an axially extended two-photon excitation scheme. Optimal spatial and temporal laser pulse parameters are then explored in the context of the fluorescence signal, photo damage and saturation. This is followed by a demonstration of two-photon imaging at 20 volumes-per-second speed, roughly 100 times faster than a point-scanning two-photon microscope.

1.2 Wave Equation and Light-Matter Interactions

As will be elaborated in later sections, this work focuses on optimization of two-photon excited fluorescence. The fundamental approach to optimizing fluorescence is to control the delivery of optical energy in space and time to the molecules that are being excited. Hence, when performing this type of work, it is essential to have access to models of optical field propagation in various media. Optical field propagation in a homogenous, isotropic dielectric medium can be described by the following wave equation [6].

$$\nabla^2 \boldsymbol{E} - \frac{1}{c^2}\frac{\partial^2 \boldsymbol{E}}{\partial t^2} = \mu_0 \frac{\partial^2 \boldsymbol{P}}{\partial t^2} \quad (1.1)$$

Here, **E** is the electric field vector, **P** is the polarization density vector, c is the speed of light in vacuum and μ_0 is the permeability of free space. The polarization density **P**, can be represented as a series expansion as follows. χ is the electric susceptibility.

$$P(E) \approx \epsilon_0 \chi E + 2dE^2 + 4\chi^{(3)}E^3 + \ldots \quad (1.2)$$

Equations 1.1 and 1.2 describe the type of phenomena observed in linear and nonlinear optical microscopes. The linear and nonlinear terms in the cases with non-zero $\boldsymbol{P}(E)$ describe various effects that occur within the sample, including single-photon and two-photon absorption processes. In many cases, the non-linearity is only evident in the limit of large electric fields, as in the case of two-photon excitation of fluorophores.

1.3 Light Propagation Models

Optical microscope design requires modeling of how an input light field propagates through the different elements of the microscope to the sample. Depending on the type of microscope, light transmission to the detector might also have an impact on properties such as resolution and signal to noise ratio. While a rigorous method of characterizing performance would be to solve the wave

equation introduced earlier, methods that are analytically and computationally less challenging can often be utilized.

1.3.1 Ray Propagation

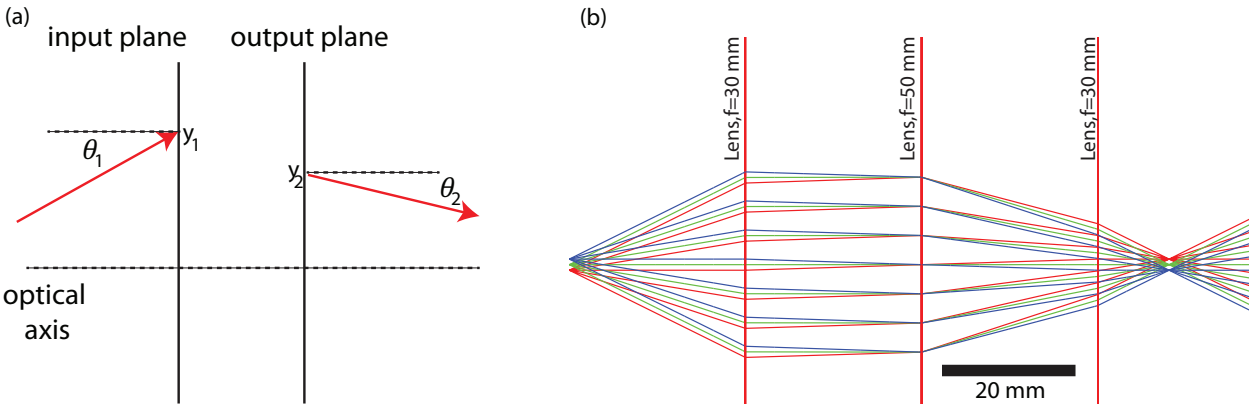

Figure 1: Ray Propagation.

(a) An optical element or system can be characterized by how it operates on a ray. (b) Ray propagation example using ray-transfer matrices for an optical system with 3 thin lenses. Each color represents a different point source.

Ray propagation methods perform ray tracing through the optical system and provide an intuitive description of the performance of an optical system. In general, the ray approximation is valid in the limiting case of $\lambda \to 0$, and is governed by the Eikonal equation below.

$$|\boldsymbol{\nabla} S|^2 = n^2 \quad (1.3)$$

The ray trajectories are along the gradient of the Eikonal S, and n is the refractive index . In most optical elements encountered in microscopy, the refractive index is homogenous inside the element, and the ray trajectories can be computed by solving for direction changes at each boundary. As shown in figure 1, a ray is described by a spatial coordinate as well as an angle. For many simple optical elements, the relationship between the input and output rays are described by a 2x2 matrix known as the ray transfer matrix or the ABCD matrix M. Knowing the input ray position y_1 the angle θ_1 and the ray transfer matrix elements A, B, C and D of an optical element allows the calculation of the output ray from the element as follows.

$$\begin{bmatrix} y_2 \\ \theta_2 \end{bmatrix} = M \begin{bmatrix} y_1 \\ \theta_1 \end{bmatrix} \qquad (1.4)$$

$$M = \begin{bmatrix} A & B \\ C & D \end{bmatrix} \qquad (1.5)$$

For a system that contains many optical elements, the ray transfer matrix of the whole system can be generated by multiplying the ray transfer matrix of each element starting from right to left [6, 7]. The ray transfer matrix approach then forms a powerful tool when designing optical systems. figure 1(b) shows ray propagation through an optical system made up of 3 thin lenses under the paraxial approximation computed using ray transfer matrices. The ray trace can be used to identify the location of the image plane which appears to the right of the third lens as well as the diameter of the ray bundle at each point in the optical system. Diagrams of this nature can be used decide on the optimal focal length and the diameter of optical elements used in a complex design.

While this above example assumed thin lenses, real-world lenses perform differently from the thin lens approximation. The ray transfer matrix approach can be extended to thick lenses since a thick lens can be modeled as series of simple surfaces. Ray propagation through thick lenses can be used perform more rigorous analysis of optical systems as they can display imperfect performance due deviation from the thin lens model. These deviations, known as ray aberrations, will be discussed in chapter 2.

1.3.2 Scalar Wave Propagation

While ray propagation can reveal many details about the system, rays do not model the behavior of optical fields that are localized. When the extent of the optical field becomes comparable to the wavelength, as is the case near the focus of a high numerical aperture imaging system, wave effects become dominant. For example, ray propagation through a thin lens shows all rays focusing to a

single point whereas, in reality, wave effects dictate that the beam size at the focus is finite. Hence, it is often useful to supplement ray propagation with wave models.

In order to develop a wave model, the problem to be solved is concerned with the propagation of electromagnetic radiation. In the context of microscopy, the optical field at one plane ($z = 0$ plane) is known and the problem is to find the field at some distance z away from this plane. The rigorous approach here is to solve the electromagnetic wave equation. Assuming the region of space that the radiation is propagating is a linear, isotropic, homogeneous and nondispersive dielectric, the problem can be greatly simplified. Observing that in this case, each vector component satisfies the same equation, it is possible to replace the vector equation with a single scalar equation [8]. Finally, separating the space and time parts yields the Helmholtz equation, which can be cast in the form below. The above approximation, known as the scalar approximation, will remain valid provided the size of the diffracting aperture is large compared to the wavelength λ [8].

$$\frac{\partial^2 E}{\partial x^2} + \frac{\partial^2 E}{\partial y^2} + \frac{\partial^2 E}{\partial z^2} - 2ik\,\frac{\partial E}{\partial z} = 0 \qquad (1.6)$$

Here E represents the scalar field amplitude and $k = \frac{2\pi}{\lambda}$. Assuming that the quantity $|\frac{\partial^2 E}{\partial z^2}|$ is much smaller than $|\frac{\partial^2 E}{\partial x^2}|$, $|\frac{\partial^2 E}{\partial y^2}|$ or $|2k\,\frac{\partial E}{\partial z}|$ yields the paraxial wave equation below [7].

$$\frac{\partial^2 E}{\partial x^2} + \frac{\partial^2 E}{\partial y^2} - 2ik\,\frac{\partial E}{\partial z} = 0 \qquad (1.7)$$

The physical interpretation of the paraxial approximation is that the field variation in z is slow compared to the field variation in x and y. In terms of ray angles, this translates to the requirement that $\theta \leq 30°$ [7]. Note that for a wave propagating in water ($n = 1.33$) this condition will only

be violated for rays exceeding a numerical aperture of 0.64, and hence the paraxial approximation can be used even for tightly focused beams.

1.3.2.1 *Huygens-Fresnel Diffraction Integral*

Knowing the scalar field at the input plane $E(x, y, z = 0)$, the above equation can be used to numerically propagate the field in z. This can be achieved by numerical differentiation and integration of the scalar wave equation. While the above approach can be used to propagate fields, it is expensive in terms of computation. Microscopists typically use other scalar diffraction approaches to propagate scalar fields. One such approach uses the Huygens principle.

As depicted in figure 2, the Huygens principle assumes that the field at $z = 0$ is generated by a series of 'secondary-sources', each one emitting a spherical wave that propagates to the observation plane. Note that this does not imply that there are physical emitters at $z = 0$. In this case, the field at a point on the observation plane will be a coherent superposition of the effects of each secondary source as seen from the observation point.

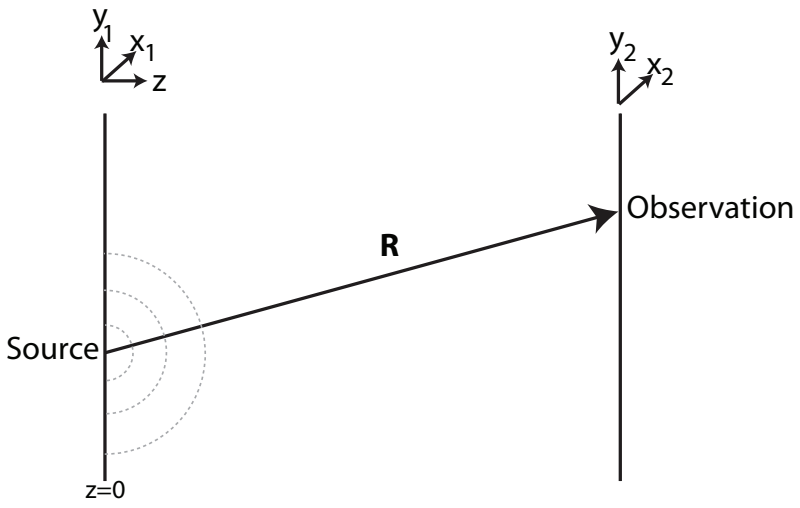

Figure 2: Huygens Principle.

Each point in the input plane is thought to be radiating a spherical wave. The field at the observation point is a summation of the fields emitted by all points in the input plane.

This principle can be expressed as an integral of the form below [6, 9, 10]. The integral is simply a sum of spherical waves emitted at different spatial locations on the source plane evaluated at the observation point.

$$E(x_2, y_2, z) = -\frac{i}{\lambda}\int E(x_1, y_1, 0)\frac{exp(ikR)}{R}cos(\theta)\, dx_1 dy_1 \qquad (1.8)$$

Here, $k = \frac{2\pi}{\lambda}$, R is the distance between the source and the observation points, and θ is the angle the between the optical axis and the line connecting the source and observation points. The wavelength λ in a medium is related to the vacuum wavelength λ_0 through $\lambda = \frac{\lambda_0}{n}$, where n is the refractive index. The above can be further simplified by assuming the Fresnel approximation ($[x_2^2 + y_2^2]^2 \ll \lambda z^3$) is valid. In this case the spherical waves emitted by the point sources can be replaced by paraxial spherical waves [6]. This yields the following equation, known as the Fresnel diffraction integral [6, 10, 11].

$$E(x_2, y_2, z) = -\frac{i}{\lambda z}exp(ikz)\int E(x_1, y_1, 0)\, ex\, p[\frac{ik}{2z}\{(x_2 - x_1)^2 + (y_2 - y_1)^2\}]\, dx_1 dy_1 \quad (1.9)$$

Observing that equation above takes the form of a convolution integral, the same results can be expressed either as equation 1.10 or equation 1.11 [10].

$$E(x, y, z) = h(x, y, z) \otimes E(x, y, 0) \quad (1.10)$$

$$\hat{E}(k_x, k_y; z) = H(k_x, k_y; z)\, \hat{E}(k_x, k_y; 0) \quad (1.11)$$

$$h(x, y) == -\frac{i}{\lambda z}exp(ikz)\, exp\left(\frac{ikr^2}{2z}\right) \quad (1.12)$$

$$H(k_x, k_y, z) = exp(ikz)\, exp[-\frac{i\lambda z}{2}(k_x^2 + k_y^2)] \quad (1.13)$$

The symbol $\otimes$ implies the convolution operator and the symbol $\widehat{\ }$ implies the 2-dimensional Fourier transform operator with $r^2 = x^2 + y^2$. $h(x, y)$ is the impulse response function and $H(k_x, k_y)$ is the trasnfer function corresponding to free-space field propagation subject to the Fresnel approximation. Equations 1.10 and 1.11 allow easy implementation of numerical field propagation as convolution and Fourier transform operations that are well implemented in many programing languages.

A special case of Fresnel diffraction occurs when computing the field at the focus of a thin lens. For the case where the lens is placed at $z = 0$ and the observation plane is the focal plane of the lens ($z = f$), the output field is given by the following relation [6, 10].

$$E(x, y, f) = -\frac{i}{\lambda f} exp(ikf)\, exp\left[\frac{i\pi(x^2+y^2)}{\lambda f}\right] \hat{F}(\frac{x}{\lambda f}, \frac{y}{\lambda f}, 0) \quad (1.14)$$

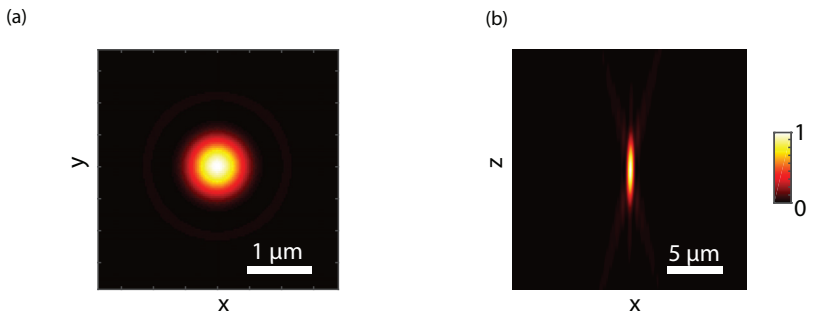

Figure 3: Normalized optical intensity distributions computed using Fresnel diffraction.

(a) x-y plane. (b) x-z plane. $\lambda = 850$ nm, n=1.33, numerical aperture NA =0.6.

where $\hat{F}$ is the 2-dimensional Fourier transform of the field at the lens pupil. Equation 1.14 directly establishes the field at the focal plane in terms of the field at the lens plane and can be computed as a single 2-dimensional Fourier transform operation. Combined with equations 1.10 or 1.11, this allows the computation of the 3-dimensional field distribution in the vicinity of the focus of a

microscope. For fluorescence microscopy, optical intensity I is more useful than the scalar field E and and can be computed as $I(x,y,z) = |E(x,y,z)|^2$. Figure 3 shows an example of the optical intensity near the focus of a high numerical aperture focusing system computed using Fresnel diffraction discussed above. The incident field was assumed to be a plane wave impinging on a lens with a circular aperture. The intensity distribution near the focus comprises of an axially elongated structure that is not evident in the ray trace diagrams. In addition, weak ring-shaped side lobes are seen in the lateral beam profile which are the result of diffraction from the aperture. Since wave models provides information about the intensity distribution near the focus, they are used to compute the resolution of microscopes.

Gaussian beam propagation

Laser sources used for microscopy typically operate in the TEM_{00} mode, which has a Gaussian spatial profile. Knowing all the beam parameters at a single plane, it is possible to analytically propagate the beam in free space. The field of the Gaussian beam is given by the following equation [6, 12].

$$E(x,y,z) = \frac{E_0}{q(z)} exp[-\frac{ik(x^2+y^2)}{2q(z)}]exp(-ikz) \quad (1.15)$$

The quantity $q(z)$, known as the q-parameter, is related to the wavefront radius curvature $R(z)$, $1/e^2$ beam radius $w(z)$ and the confocal parameter z_0 as follows.

$$\frac{1}{q(z)} = \frac{1}{R(z)} - i\frac{\lambda}{\pi w^2(z)} = \frac{1}{z+iz_0} \quad (1.16)$$

For fluorescence microscopy, the quantity of interest is the beam intensity. Then the intensity distribution of a Gaussian beam can be expressed as:

$$I(x,y,z) = \frac{2P_0}{\pi w^2(z)} exp[-\frac{2(x^2+y^2)}{w^2(z)}] \quad (1.17)$$

P_0 is the beam power. The propagation of Gaussian beams in free-space is governed by the equations presented in Appendix 1. However, it is more convenient to use the ABCD matrix method to propagate Gaussian beams through optical systems. If the ABCD matrix for a system or an element is known, the q-parameter at the input q_1 and at the output q_2 are related through the following equation.

$$q_2 = \frac{Aq_1+B}{Cq_1+D} \quad (1.18)$$

Thus, Gaussian beams can be propagated through multi-element optical systems using ABCD matrices similar to how rays were propagated in section 1.3.1. Gaussian beams can be generalized to a case of an astigmatic beam, where the x and y dimensions propagate differently. Astigmatic Gaussian beams will be explored in Chapter 3.

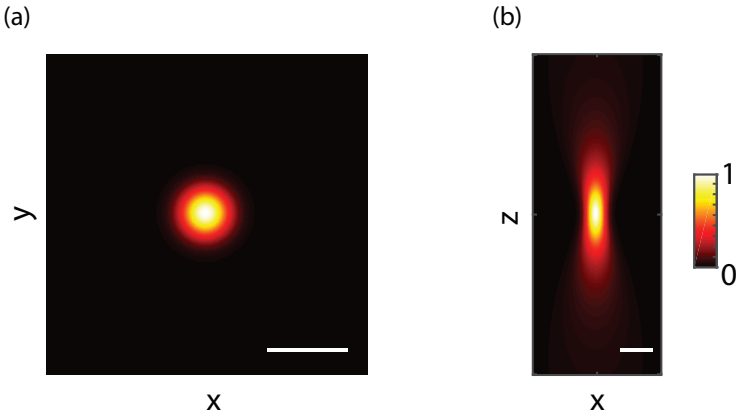

Figure 4: Normalized Gaussian beam intensity distribution for a tightly focused beam.

(a) x-y plane at the beam waist and (b) in the x-z plane. $\lambda = 800$ nm. n=1.33. Effective numerical aperture NA=0.6. Scalebar = 1 μm.

Figure 4 shows the intensity profiles for a tightly focused Gaussian beam. The axial extent of the beam is larger than the lateral extent. It will be seen that in the microscopes discussed in this work,

the lateral resolution will be far superior to the axial resolution. This relationship is not a property of the Gaussian beam but a result of diffraction. The same effect can be seen for a plane wave focused with a lens. For a Gaussian beam, the lateral beam radius and the Rayleigh range are related by $z_0 = \frac{n\pi w_0^2}{\lambda_0}$, where the axial full-width at half maximum (FWHM) is $2z_0$. While having an extended axial depth is usually not desirable, Chapter 3 will present a case when this relationship between lateral and axial extents can be exploited to create large two-photon excitation volumes.

While the real output from a laser deviates from the perfect Gaussian beam case, Gaussian beams nevertheless offer a convenient tool for estimating the spatial extents of the microscope point-spread-function. The deviation a real laser beam from the ideal case is characterized by the $\mathbb{M}^2$ factor, which is the ratio between the waist-diameter-divergence product of the beam to that of an ideal gaussian beam [6]. The laser sources used in this work have an $\mathbb{M}^2$ factor of less than 1.2, and hence the deviation from the ideal is not of great concern.

In systems where aberrations are not expected, Gaussian beam propagation allows the characterization of the optical system. This is computationally less expensive than numerical propagation using Fresnel diffraction. In addition, the convenient form of a Gaussian simplifies raising to powers required for nonlinear excitation and integration used to compute fluorescence and can be used to derive analytical relations describing a number of different excitation schemes.

1.4 Absorption and Fluorescence

Microscopes are used to visualize a wide array of phenomena. Central to the process of image generation is the contrast mechanism. For two-photon microscopy, the contrast mechanism is fluorescence. As described below, fluorescence generates an optical signal that can be tied to the

presence of some molecule. Analysis of the strength and the emission wavelengths of the fluorescence can be used to identify the presence of various chemical species [13].

Fluorescence occurs when a molecule absorbs energy from an excitation light source and releases a part of that energy while relaxing back to the ground state. Figure 5(a) shows a simplified energy level diagram describing this process.

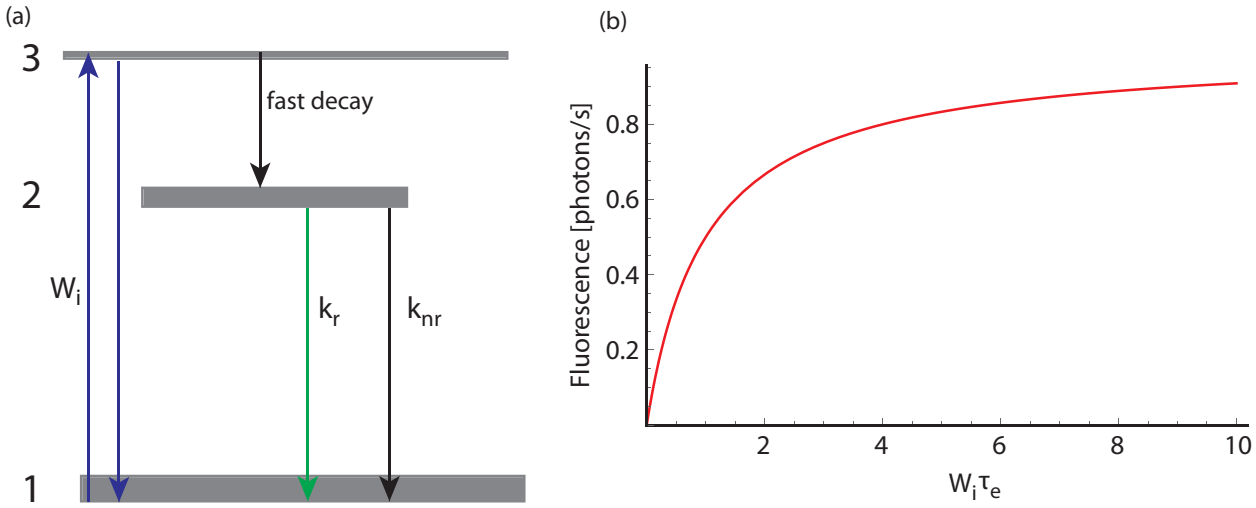

Figure 5: Absorption and fluorescence.

(a) Energy level diagram of a three-level system. The system is optically pumped from the ground state (level 1) to level 3 and then rapidly decays to the long-lived level 2. Radiative decay from level 2 to 1 emits fluorescent light. (b) Saturation behavior: Fluorescence approaches a maximum value in the limit of strong pumping.

1.4.1 Rate Equations

The molecules are excited from level 1 to 3 at a rate W_i through optical excitation. Molecules in level 3 can decay to the ground state at the same rate W_i through stimulated emission. However, real molecules typically decay rapidly performing the 3→2 transition, which means that stimulated emission from level 3 does not play a significant role in many cases [10]. Because of this, population accumulation will occur in level 2. Molecules in level 2 can then decay to the ground state through radiative and non-radiative decay at rates k_r and k_{nr} respectively. When the radiative decay causes optical emission, the process is known as fluorescence. Because the fluorescent light

is emitted from the 2→1 transition and not the 3→1 transition, the fluorescence is red-shifted (or stokes-shifted) compared to the excitation light. In this case, the rate equations for the system are as follows [10].

$$\frac{dn_1}{dt} = -\frac{dn_2}{dt} = -W_i n_1 + \left(\frac{1}{\tau_r} + \frac{1}{\tau_{nr}}\right) n_2 \quad (1.19)$$

where n_1 and n_2 are probability of states 1 and 2 being occupied, while τ_r and τ_{nr} are the decay times associated with the rates k_r and k_{nr}. Note that $n_1 + n_2 = 1$. In thermal equilibrium, the occupation between two states is given by $\frac{n_2}{n_1} = \exp(-\frac{\mathrm{E}_2 - E_1}{k_B T})$ (ignoring degeneracy) where E_1 and E_2 are the energies associated with states 1 and 2 respectively, k_B is the Boltzmann constant and T is the temperature [6]. A transition in the visible spectrum is associated with energy ~2.5 eV and $k_B T \sim 25$ meV at room temperature, hence it can be assumed that the excited states are unoccupied at thermal equilibrium. Because some of the energy will contribute to non-radiative processes, it is useful to define the quantum efficiency η, which is the efficiency with which the molecule converts absorbed energy to fluorescence. Another quantity of interest is the excited state lifetime τ_e. On average, an excited molecule takes time τ_e to decay back to the ground state.

$$\eta = \frac{\frac{1}{\tau_r}}{\frac{1}{\tau_r} + \frac{1}{\tau_{nr}}} \quad (1.20)$$

$$\tau_e = \frac{1}{\frac{1}{\tau_r} + \frac{1}{\tau_{nr}}} \quad (1.21)$$

Solving equation 1.19 for the steady state case yields the steady state probability $n_{2,SS}$ and the related fluorescence rate $S = n_{2,ss}/\tau_r$. If the excitation is weak ($w_i \tau_e \ll 1$), the fluorescence S is

a linear function of W_i. For strong excitation, S becomes non-linear in W_i and reaches a maximum value. This behavior is shown in Figure 5(b).

$$n_{2,ss} = \frac{W_i \tau_e}{1 + W_i \tau_e} \quad (1.22)$$

Finally, fluorescence can be seen as originating from many individual dipole oscillators, each radiating with a random phase offset [7]. This means that unlike the excitation light, which is a beam, fluorescent light is emitted in all directions. Increasing the collection efficiency of a fluorescence microscope then requires increasing the solid-angle captured and relayed onto the detector. This is one reason why high numerical aperture objectives are preferred for fluorescence imaging.

1.4.2 Two-Photon Excited Fluorescence

So far, no distinction has been made between single and two-photon absorption processes. As depicted in figure 6(a), a single photon absorption event occurs when the energy from a single excitation photon is used to excite a molecule.

In a two-photon absorption process, the transition can be seen to be mediated by a virtual state (depicted as V in Figure 6(b)), with the first absorbed photon resulting in a 1→V transition and the second absorbed photon resulting in a V→2 transition. The virtual state lifetime is in the order of femtoseconds [14], and hence two-photon absorption events are rare except in the case of very high photon flux densities that will facilitate near simultaneous absorption of two-photons. Two-photon excitation was first predicted by Göppert-Mayer in 1931 [15] and experimentally demonstrated in 1961 [16]. The first two-photon microscope was demonstrated in 1990 [17].

In two-photon microscopy, the photons contributing to the excitation process are typically at the same wavelength, yielding degenerate two-photon excitation. While it is possible to use photons of two different wavelengths to achieve two-photon excitation, such schemes are not typically utilized in biological imaging and hence this work does not explore such a scheme.

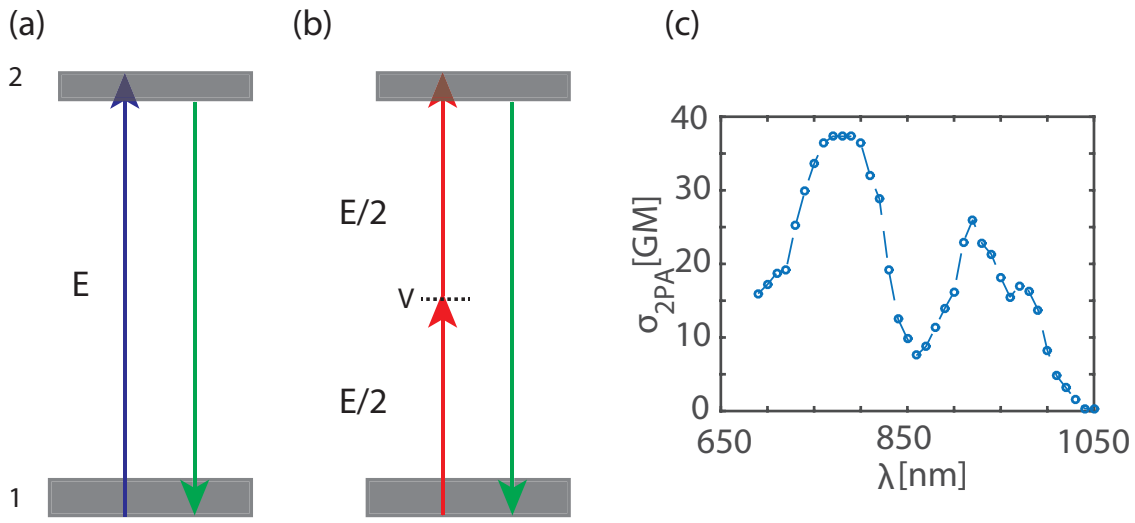

Figure 6: Two Photon Absorption.

(a) Energy level diagram for single photon excitation where a photon of energy E is absorbed (b) Energy level diagram for two-photon absorption where two photons of energy E/2 are absorbed. (c) Two-photon action cross-section for Fluorescein in water (data source : [18]).

In general, the two-photon absorption spectra cannot be estimated using single-photon absorption spectra as the selection rules for two-photon absorption differ from that of single-photon absorption [14]. However, the two-photon absorption cross-section spectra of many fluorophores and fluorescent proteins have been measured. Given that many fluorophores have wide absorption bands, they can be subjected to two-photon excitation using a Ti:Sapphire laser, which is tunable in the $700\,nm - 1000\,nm$ wavelength band. The wide absorption bands also allow multiple fluorophores to be excited at the same time [2].

The transition rate for single and two photon absorption are given by $W_i = \sigma_a \frac{I}{\hbar\omega}$ [10] and $W_i = \sigma_{2PA} \frac{I^2}{2\hbar\omega}$ [19] respectively, where σ_a is the absorption cross-section and σ_{2PA} is the two-photon absorption cross section. Equation 1.22 shows that for single-photon absorption, the fluorescence scales linearly with beam intensity for single-photon absorption and the square of the beam intensity for two-photon absorption provided the excitation intensity is low. In both cases, saturation occurs for strong excitation.

The treatment above ignores some details of the energy levels in realistic molecules. There are two additional types of decay paths to be considered. Once in the excited state, the system can undergo an intersystem crossing and enter the triplet state. The triplet state lifetimes are in the order of μs while the the excited state lifetimes described above are in the order of ns. Thus, a molecule entering the triplet state will, on average be unavailable for fluorescence generation for the triplet state lifetime. Also, additional decay pathways can lead to a process known as photobleaching, which can also place the molecule in a state where it is not available for fluorescence generation. The effects of an intersystem crossing are temporary, while photobleaching is permanent [10].

1.5 Scattering

Another light-matter interaction that is especially relevant for imaging biological tissue is elastic light scattering. Scattering can be seen as an effect of an external electric field inducing polarization in the particles making up the material [20]. The induced polarization will emit a 'scattered' radiation field that is not necessarily pointing in the direction of propagation of the incident beam.

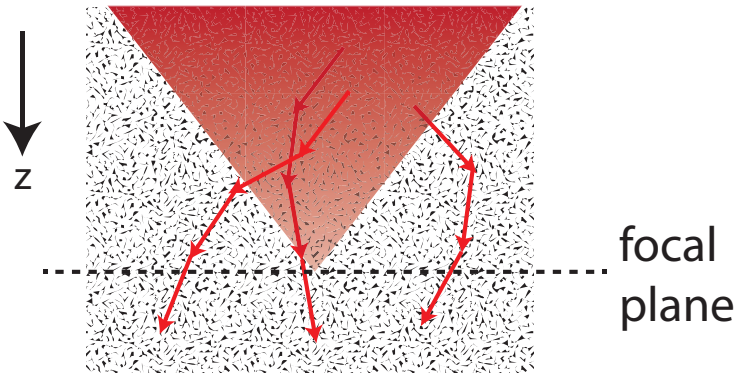

Figure 7: Schematic depicting elastic light scattering

The challenge in 3-dimensional fluorescence microscopy is in delivering optical intensity to a specific spatial location within the sample. While microscopes can be designed to provide a high-quality focus in a homogenous medium, biological media are not homogenous. Figure (7) shows a schematic of a beam entering a scattering sample. The solid cone represents the incident beam from the microscope. As the beam travels through the sample, some parts of the beam will be scattered as depicted by the arrows. This scattering phenomenon results in two effects. The first one is that the incident beam will lose power as it penetrates deep into the sample. The second effect is that the lost power is distributed in various directions inside the sample. The optical intensity at the focal plane will then have two components [21].

$$I_{focus}(x, y) = I_{ballistic} + I_s \qquad (1.23)$$

Here $I_{ballistic}$ is the input beam propagating in the medium and I_s is the scattered component of light depicted as arrows in figure 7. Given that scattering has a strong effect on the excitation beam, it is useful to have a quantitative and qualitative understanding of its effects. In many samples, there is both scattering and absorption. Similar to absorption, the 'strength' of scattering is quantified using a cross-section. The total cross-section for a particular type of particle, referred

to as the extinction cross section σ_e can be represented interms of the absorption cross-section σ_a and the scattering cross-section σ_s as $\sigma_e = \sigma_a + \sigma_s$ [10]. It is also useful to define the following:

$$\mu_s = c\sigma_s \quad (1.24)$$

$$\mu_a = c\sigma_a \quad (1.25)$$

$$\mu_e = \mu_a + \mu_s \quad (1.26)$$

where μ_s, μ_a and μ_e are the scattering, absorption and extinction coefficients respectively having units of $\frac{1}{m}$ with c being the concentration of the particles having units of $\frac{1}{m^3}$. For a beam propagating through such a sample with thickness z, the ballistic power at the output P_{out} and input P_{in} are related by the Beer-Lambert law [10]:

$$P_{out} = P_{in}exp(-\mu_e z) \quad (1.27)$$

Note that the above equation only represents the power lost from the beam due to scattering and absorption and not the power carried in the scattered light. Another quantity of interest is the reduced scattering coefficient [22].

$$\mu_s' = \mu_s(1 - g) \quad (1.28)$$

Here $g =< \cos(\theta) >$ is the scattering anisotropy factor and is an average over many scattering events. Hence $g \approx 1$ represent a medium that scatters mostly in the forward direction. Characteristic lengths of $l_s = 1/\mu_s$ which is the scattering mean free path represents the average distance a photon travels before being scattered and the transport mean free path and $l_t = 1/\mu_s'$

represents the average distance after which the photon directions can be considered randomized. The value of $g \approx 0.9$ for biological tissue [22] indicates that scattering occurs mainly in the forward direction.

For scattering from a collection of dielectric particles which are small compared to λ, the scattering cross-section follows the Rayleigh scattering relationship $\sigma_s \propto \frac{1}{\lambda^4}$v [23]. However, biological tissue is better approximated by scatters of various sizes [22]. For brain tissue, the variation scales as $\sigma_s \propto \frac{1}{\lambda^{1.3}}$ [24].

In microscopy applications, the scattered light intensity I_s forms an unintentional fluorescence background signal. When the fluroescence generated from the background becomes comparable to the signal generated from the ballistic light, contrast is lost [25]. Two-photon microscopy excels at suppressing this out-of-focus background. More details will be discussed in the next section.

1.6 Two-Photon Microscopy and Volumetric Imaging

A two-photon microscope exploits two-photon excited fluorescence as the contrast mechanism. These microscopes are typically point-scanning systems. This section will introduce point-scanning two-photon microscopy, formally known as two-photon laser scanning microscopy (2PLSM).

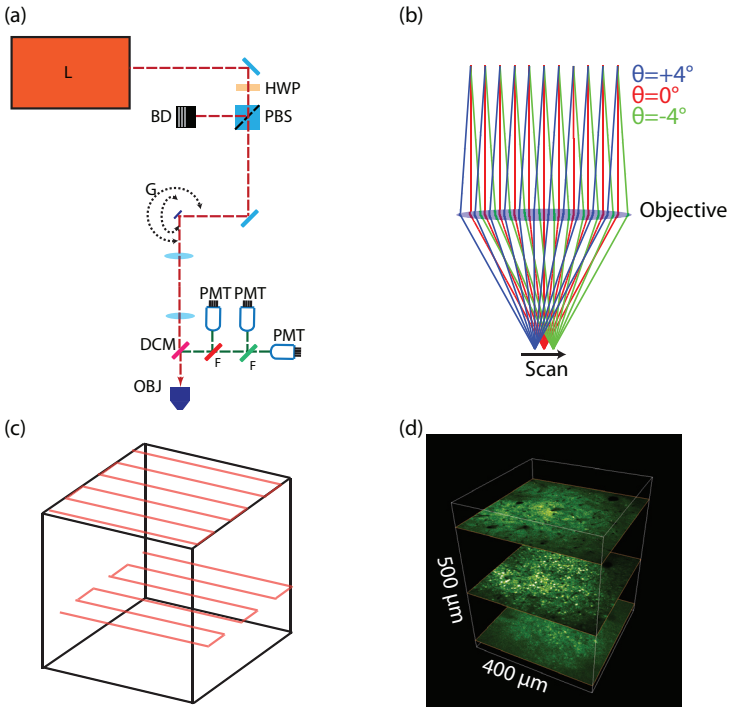

Figure 8: Two-Photon Laser Scanning Microscopy.

(a) Typical Setup. L: Laser, HWP: Half-wave plane PBS: Polarizing beam splitter, BD: Beam-dump, G: x-y scanning mirrors DCM: Dichroic mirror, OBJ: Objective, F: Filter, PMT: Photomultiplier tube. (b) Point scanning: lateral scanning achieved by changing the incoming beam angle. The three colors representing three ray angles focus to three different lateral location in the sample. Axial scanning is achieved by moving the sample or the objective along the z-axis. (c) Scan pattern: Often the beam is scanned in a raster pattern to sample a single plane. This is repeated for many planes to form a 3-dimensional image. (d) Example 2PLSM image stack shows GCaMP labeled mouse brain.

As discussed in the previous sections, two-photon absorption from molecular fluorophores is a rare event and thus two-photon microscopes typically operate in a point-scanning configuration. This allows the photon flux density to be high at a single point inside the sample. A 3-dimensional image as shown in figure 8(d), is formed by spatially sampling the object being imaged by scanning the excitation spot through the sample. The excitation arm of the microscope consists of a laser beam that is scanned along the x and y dimensions by two scanning mirrors. The beam, along with the scan patterns, is relayed on to the objective using relay optics. The ABCD matrix describing light propagation from the objective pupil to the focal plane is given by $M = \begin{bmatrix} 0 & f \\ -1/f & 1 \end{bmatrix}$. Changing the ray angle at the objective pupil causes the beam to deviate laterally at the focal plane

and hence the x and y mirrors perform a lateral scan at the sample. Axial scanning can be performed by either moving the sample or the objective. A typical volume image is acquired by raster scanning the beam through sections of the sample, with each scan generating a lateral 2-dimensional image as shown in Figure 8(c). Acquiring many 2-dimensional images at regular intervals along z allows the construction of a 3-dimensional image as shown in Figure 8(d). The following sections will detail the differences between single and two-photon microscopy.

1.6.1 Optical sectioning

One major characteristic of two-photon excitation is its inherent optical sectioning ability. Figure 9(a) shows the obvious difference between single photon (visible light) excitation vs. two-photon (near infrared light) excitation of a dye solution. In the case of single-photon excitation, fluorescent light is seen to originate from all z-planes of the beam. For two-photon excitation, the fluorescent light is generated at the focus of the beam. The localization of two-photon excited fluorescence means that the fluorescence can be captured on a single element detector, and a 3-dimensional image can be constructed by scanning the focal spot in 3-dimension within the sample. What follows is a rigorous description of the optical sectioning ability of a two-photon microscopy.

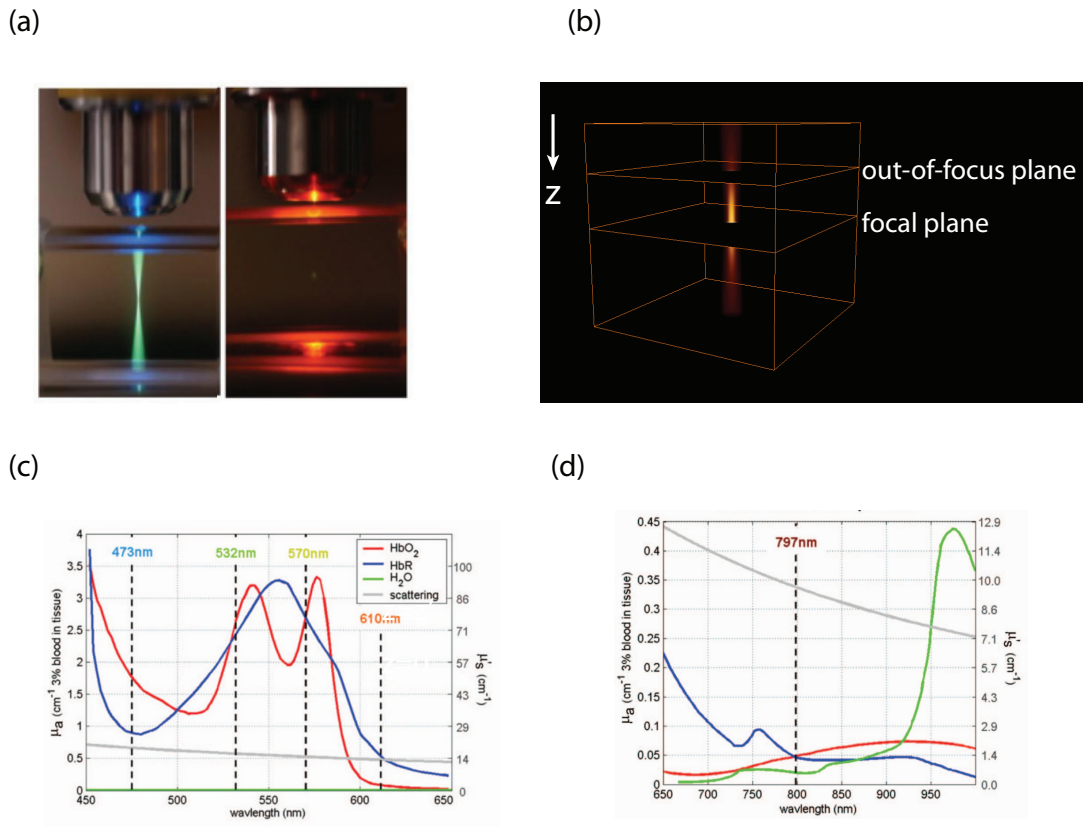

Figure 9: Optical sectioning and depth penetration.

(a) Single photon (blue light) vs two-photon (near IR light) excitation. With single photon excitation, there is out-of-focus fluorescence. In two-photon excitation, out-of-focus excitation is suppressed. Image source: Ref. [26] (b) reference figure for out of focus excitation argument. (c) & (d) Reduced scattering coefficient and absorption coefficient of the brain tissue and blood. Both quantities are low in the near-infrared wavelengths. Source: [24].

For a beam propagating in a non-scattering medium, the single-photon excited fluorescence S in space is given by, $S_{1P}(x,y,z) = \sigma I(x,y,z)$ while the two-photon excited fluorescence is given by $S_{2P} = \sigma_{2P} I^2(x,y,z)$ with σ being the fluorescence cross-section in units of m^2 and σ_{2P} being the two-photon action cross-section in units of $\frac{m^4}{W}$ respectively. The optical sectioning ability can be computed by considering the fluorescence signal generated by an infinitesimally thin fluorescence sheet placed outside the Rayleigh range of a Gaussian beam ($z \gg z_0$, where z_0 is the confocal parameter of the beam) as shown in figure 9(b). The one-photon fluorescence S_{1p} and the

two-photon fluorescence S_{2P} generated by such sheet with a fluorophore concentration of c, illuminated with a gaussian beam is given by:

$$S_{1P}(z) = c\sigma \int I(x,y,z)\, dxdy = c\sigma P \quad (1.29)$$

$$S_{2P}(z) = c\sigma_{2P} \int I^2(x,y,z)\, dxdy \propto \frac{c\sigma_{2P}P^2}{w^2(z)} \propto \frac{1}{z^2} \quad (1.30)$$

Above results were obtained assuming that the beam waist is at the focus of the lens at $z = 0$ and using the relation $\int I\, dxdy = P$, where P is the power. For single photon excitation, fluorescence is generated equally from all z planes, while for two-photon excitation, the fluorescence generation decays rapidly with z for out of-focus planes. Hence, two-photon excitation provides inherent optical sectioning. For single photon excitation, a different scheme is required provide optical sectioning. One such example is confocal microscopy where a pinhole is used to reject out-of-focus light.

1.6.2 Depth Penetration

Another advantage of two-photon excitation comes from the longer penetration depth associated with near-infrared excitation. As described previously, the scattering coefficient in brain tissue scales as $1/\lambda^{1.3}$, and hence the scattering coefficients at near-infrared wavelengths are lower compared to visible wavelengths. In addition, the absorption coefficient of blood is smaller at near-infrared wavelengths compared to visible wavelengths. The scattering and absorption coefficient for brain and blood are shown in figure 9(c) and 9(d). This allows the near infrared excitation beam to penetrate deeper into the tissue compared to visible light excitation used in single-photon microscopy.

1.6.3 Background Suppression

The final advantage of two photon microscopy is its ability to suppress background fluorescence. This effect also originates from the I^2 dependence of two-photon excited fluorescence. Given that scattered light is spatially diluted, the contribution of the scattered background is largely mitigated. Assuming the microscope is not limited by average power, the depth limit is reached when the background excitation becomes comparable to the fluorescence generated at the focus [25]. This depends on both the scattering properties as well as the absorption properties of the sample [12].

1.6.4 Optical setup

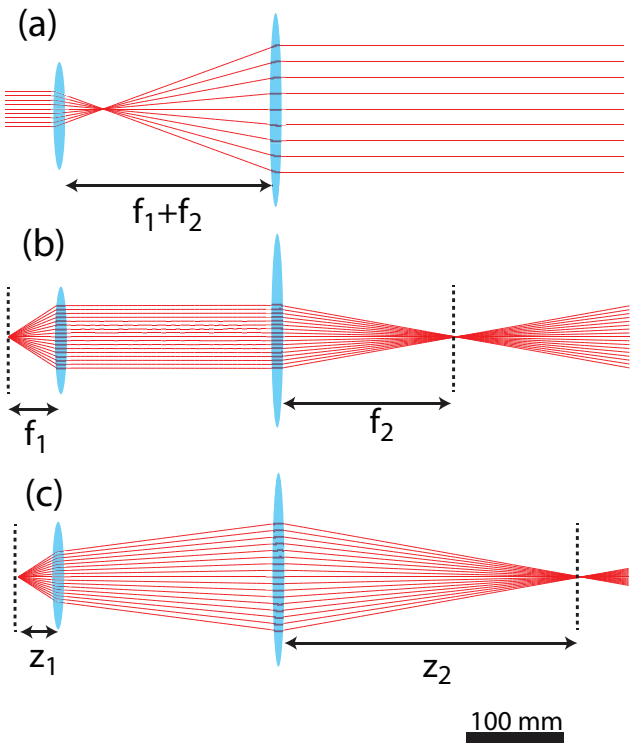

Figure 10: Scan Telescope.

The scan telescope is designed to obey the 'collimation condition' and the 'imaging condition'. (a) Ray diagram showing the collimation condition, where a parallel incoming ray bundle exits as a parallel ray bundle. (b) A special case of the imaging condition where the object is placed a focal length away from the first lens and the image forms at the focal plane of the second lens. (c) The general case of the imaging condition where an object placed a distance z_1 from the first lens forms an image a distance z_2 from the second lens. The ralationship between z_1 and z_2 are governed by ray transfer matrices or equivalantly, the thin lens equation.

The basic elements of the excitation path of the microscope include a laser beam that is scanned by two mirrors scanning in the x and y directions. As described above and shown in figure 8(b), scanning at the sample is achieved by changing the beam angle at the back aperture of the objective. Proper scanning is achieved by carefully choosing the two lenses (scan lens and tube lens respectively) which form a telescope between the scanning mirrors and the objective.

The scan telescope serves two purposes. First, it must change the magnification of the beam going into the objective while maintaining collimation. In most cases, this telescope will be designed so that the back aperture of the objective lens will be over-filled by the excitation beam. The second condition ensures that the galvanometer scanning mirror or some other optical element is imaged onto the back aperture or the back focal plane of the objective. If this condition is met, scanning the mirrors causes the beam angle to change at the back of the objective without any translation of the beam.

Figure 10(a) shows a paraxial thin lens system where the first condition, called the 'collimation condition' is met. A parallel ray bundle that impinges on the telescope exists as a magnified parallel ray bundle. In order for this condition to be true, the spacing between the lenses must be equal to their focal lengths. Figure 10(b) and 10(c) show two cases where the second condition mentioned above, called the 'imaging condition', is met. For a lens system that meets the collimation condition, the easiest way to meet the imaging condition is to place the object at the focal plane of the first lens. Then the image plane will be at the focal plane of the second lens. The ray-transfer matrix for such a system is given by $M = \begin{bmatrix} m_t & 0 \\ 0 & 1/m_t \end{bmatrix}$ where $m_t = -f_2/f_1$ is the transverse magnification.

In practice, space constraints might prevent setting up the microscope as shown in figure 10(b). It is still possible to satisfy the imaging condition under spatial constraints as shown in figure 10(c). In this case, the approach would be to use either ray transfer matrices or the thin lens equation to find z_1 where z_2 is constrained to some value (or vice versa).

1.6.5 Pulsed Excitation and Fluorescence Generation

The 2PEF power generated by a single molecule is given by $S(x,y,z,t) = \sigma_{2P} I^2(x,y,z,t)$. The values of σ_{2P} are generally small, and it is typically not possible to generate sufficient two-photon excitation using continuous wave laser sources. For this reason, two-photon microscopes utilize pulsed laser sources which can deliver high peak intensities. Assuming a square wave pulse with a repetition rate of f_l, and a pulse width of τ_p, the peak intensity I_{peak} and the time-averaged intensity I_0 are related by $I_{peak} = \frac{I_0}{f_l \tau_p}$. 2PEF signal (power) generated by a single molecule is then given by [10]:

$$S(t) = \sigma_{2P} I(t)^2 \quad (1.31)$$

For a square wave pulse, the fluorescence energy per pulse is given by

$$S_{pulse} = \sigma_{2P} \tau_p I_{peak}^2 = \frac{\sigma_{2P} I_0^2}{f_l^2 \tau_p} \quad (1.32)$$

The time averaged fluorescence power is given by,

$$\langle S \rangle = \sigma_{2P} \langle I^2 \rangle = \sigma_{2P} g_2 I_0^2 \quad (1.33)$$

Where $g_2 = \frac{1}{f_l \tau_p}$ for a pulse with a square temporal shape and $g_2 = \frac{0.664}{f_l \tau_p}$ for a Gaussian temporal shape. If the 3-dimensional distribution of beam parameters are known, then the 3-dimensional

profile of two-photon excited fluorescence can be generated by replacing I_0 with $I_0(x, y, z)$. Then the point-spread function of a two-photon point scanning microscope can be computed. The normalized 3-dimensional point-spread function $IPSF(x, y)$ for two-photon excitation can be represented by the square of the Gaussian beam intensity.

$$IPSF_{2P} = \frac{1}{w^4(z)} exp\left(-4\frac{x^2+y^2}{w^2(z)}\right) \quad (1.34)$$

Because $2PEF$ scales as the square of the beam intensity, for a guassian beam, the 2PEF excitation will have a lateral width that is smaller by a factor of $\sqrt{2}$ compared to the width of the beam. The beam width near the focus can be computed using the ABCD matrix approach. The beam parameters at the lens pupil and the focal plane are related by the ABCD matrix $M = \begin{bmatrix} 0 & f \\ -1/f & 1 \end{bmatrix}$. . In addition, when the beam waist of the incoming beam and the lens pupil are on the same plane, and the depth of focus of the incoming beam is much greater than the focal length, the beam focus is formed at the focal plane of the lens with an approximate width of $\frac{\lambda_0}{\pi NA}$ (assuming that the incoming beam diameter is equal to the diameter of the lens aperture). For example, for numerical aperture $NA = 0.6$, the beam radius at the focus $w_{0f} \approx 420\ nm$. The corresponding radius of the 2PEF excitation is approximately $420/\sqrt{2} = 297\ nm$. Hence, even though longer excitation wavelengths are used for two-photon microscopy, subcellular resolution is still easily accessible. Equations for calculating the 2PEF point-spread function for high numerical aperture and overfilled objective lenses has been described elsewhere [27].

Finally, the measured signal can be formed into a 3-dimensional image. The mathematical description of image formation is given by [10]:

$$S_{image}(x', y', z') = \phi_c \sigma_{2P} \iiint c(x - x', y - y', z - z') I^2(x, y, z) dx dy dz \qquad (1.35)$$

where x', y' and z' form the scan vector.

1.6.6 Hardware

The optical detectors used 2PLSM are typically photo-multiplier tubes (PMTs). Given the ability to modulate the gain over a large range, PMTs provide high dynamic range. Despite the large amplification, the output current from a PMT is in the nA-μA range and is converted to a voltage signal using a transimpedance amplifier (TIA) before being recorded. In order to achieve good optical signal-to-noise ratio (SNR), it is important to match bandwidth of the detection electronics to the scan-speed. For a pixel-scan-rate of f_p, the detection bandwidth Δf_d is usually set to $2 * f_p$. Setting the Δf_d too low results in blurred images since the pixel-dwell time will exceed the signal integration time. On the other hand, setting Δf_d too high results in lower SNR.

1.6.7 Laser Systems

Most 2PLSMs are operated with Ti:Sapphire laser systems. These lasers are able to generate ~2 Watts of average power along with femtosecond pulses operating at approximately 80 MHz repetition rate. The ability to tune the wavelength of these lasers allows many different fluorophores to be excited using the same light source.

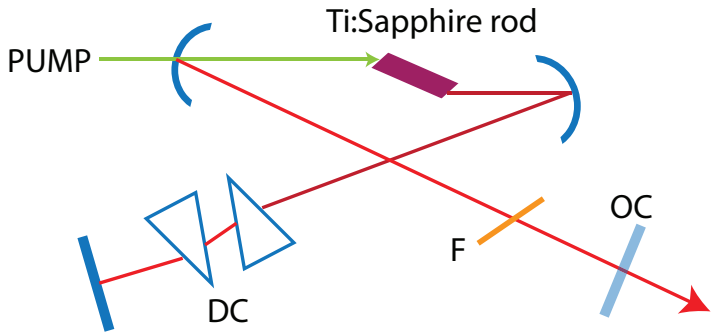

Figure 11: Ti:Sapphire Laser System

DC: Dispersion compensation prisms, F: Filter OC: Output-coupler

Figure 11 shows a schematic of a Ti:Sapphire laser. A Ti:Sapphire rod forms the laser gain medium and is pumped with continuous wave green (532 nm) light. Overlap between the green pump beam and the cavity mode is over a large length of the rod is facilitated by injecting the pump beam collinearly with the cavity mode. As shown in figure 12(a), the system operates as a 4-level system, with the 2→1 transition resulting in laser emission [6]. The wide spectral bandwidth of this transition yields a laser that is tunable in the 700 nm -1050 nm range. The tuning is facilitated using an intracavity prism system or a Bragg filter. A prism pair is used to perform intracavity dispersion compensation. In commercial systems, the pulse width optimization across wavelengths is computerized [6, 28].

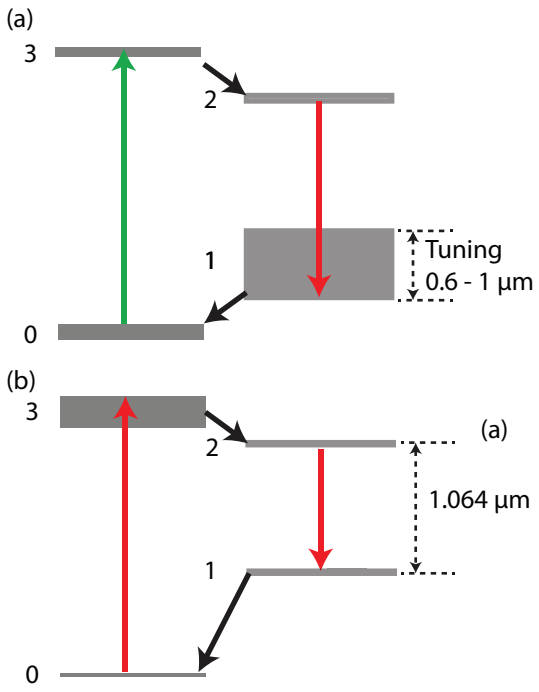

Figure 12: Simplified energy level diagrams for (a) Ti:Sapphire and (b) ND^{3+}:YVO_4

In the laser used for 2PLSM, ultrashort pulses are created through active mode-locking with an acousto-optic modulator (AOM). The AOM modulates the cavity loss at the repetition rate defined by the length of the cavity [28]. Timing between the AOM and the laser repetition rate is synchronized by driving the AOM through a feedback signal from the laser itself. The laser outputs ~ 2 Watts at the peak wavelength.

The pump beam for the Ti:Sapphire laser originates from a $ND3^{+}$:YVO_4 laser. A simplified energy diagram for this system is shown in figure 12(b). This system also operates as a 4-level system. The 2→1 transition yields 1.064 μm which is frequency-doubled to 532 nm using second harmonic generation using a LBO crystal. The output from the pump laser is ~ 13 Watts. The pump laser is also optically pumped using laser diodes [28].

Chapter 2: Wavefront Correction

2.1 Introduction

A common place to start when designing an optical system is to use the thin lens equation, or equivalently, paraxial ray transfer matrices. Such an approach can be useful in generating a model that describes the basic performance of a system. Real optical elements do not, in general, obey the thin lens equation and can deviate sharply from that approximation.

Because of this, optical systems are frequently designed with more advanced design models that take into account realistic behavior. In the ray picture, these departures from the ideal yield ray aberrations, where the rays deviate from their ideal location. Similarly, refractive elements can also be seen to modulate the phase of an incoming light-wave. In the wave picture, deviation from ideal behavior can be described in terms of phase-errors, referred to as wavefront aberrations. As will be shown later, describing an optical system in terms of its phase-errors offers a convenient way of correcting many of these errors with a single corrective element and forms the basis of wavefront correction.

Wavefront aberrations introduced by commonly used optics have been studied in great detail and it is now possible to design or optical systems that minimize errors. However, even a well-designed optical system is prone to aberrations due to non-ideal alignment. Hence, optical systems can be

expected to deviate from design behavior during actual use. This is not the only cause of aberrations. In this work, the samples being imaged are thick and inhomogeneous. For example, for mouse brain imaging, the excitation beam typically travels through an approximately 160 μm 'cranial window' followed by up to 500 μm of brain tissue. Even if the imaging system itself is well corrected for aberrations, sample induced aberrations will degrade the image quality. It is not always easy or possible to design an optical system with enough degrees of freedom to easily account for these types of aberrations.

The goal of this work is to characterize the types of aberrations encountered in mouse brain imaging with a two-photon microscope and to create a microscope that is capable self-correcting for system and sample induced aberrations. The concept of adaptively correcting for aberrations originated from astronomy where astronomers use wavefront correction to correct for aberrations originating from the atmosphere. While similar in concept to astronomical systems, applying wavefront correction to microscopy offers some unique challenges as well as opportunities. Wavefront correction in microscopy, while a recent field, is an active one. Later sections will describe some of the work done by other researchers as well.

2.2 Wavefronts and Energy Transport

In many cases considered in this work, the spatial part of an optical field can be expressed as a scalar wave of the following form [6, 29].

$$E(x,y,z) = A(x,y,z)exp[-ik\phi(x,y,z)] \quad (2.1)$$

In this definition, ϕ has units of length and the relation $\phi(x,y,z) = constant$ defines the wavefront of the above wave [6]. The rest of this section is concerned with how changes in the

wavefront ϕ effects two-photon microscopy. Figure 13 shows the wavefronts associated with a plane wave and a paraxial spherical wave traveling along the z-axis. The local direction of wave-propagation is parallel to the gradient of the wavefront. Wavefronts are linked to how energy is transported in an optical wave. In the limit of $\lambda \to 0$, ϕ becomes equivalent to the eikonal in ray-optics [6] discussed in Chapter 1. For an isotropic medium, the rays travel along wavefront normals.

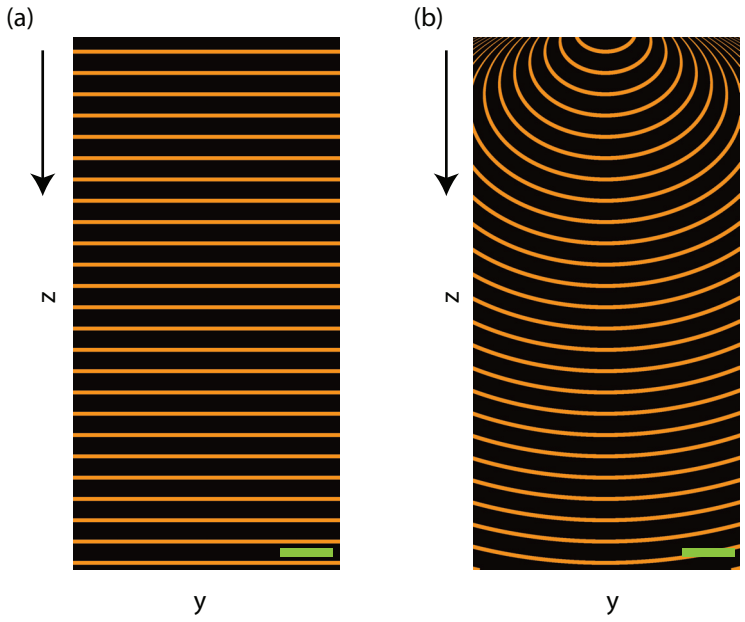

Figure 13: Wavefronts.

Wavefronts for (a) a plane wave and (b) a paraxial spherical wave propagating in vacuum along the z-axis at $\lambda = 800$ nm. Scalebar=2 μm.

For example, in figure 13(a), the rays associated with the plane wave will be a parallel ray bundle indicating a collimated beam while they rays associated with figure 13(b) will be a diverging set of rays. In fluorescence microscopy, the quantity of interest is the optical intensity I. It will become apparent later that the wavefront of an optical wave can have an impact on both the magnitude and the spatial distribution of I.

2.2.1 Reference wavefront and wavefront error

As mentioned above, any deviation of the wavefront from the expected perfect case is known as a wavefront error. In order to proceed, it is necessary to identify what a perfect wavefront would be for situations encountered in microscopy.

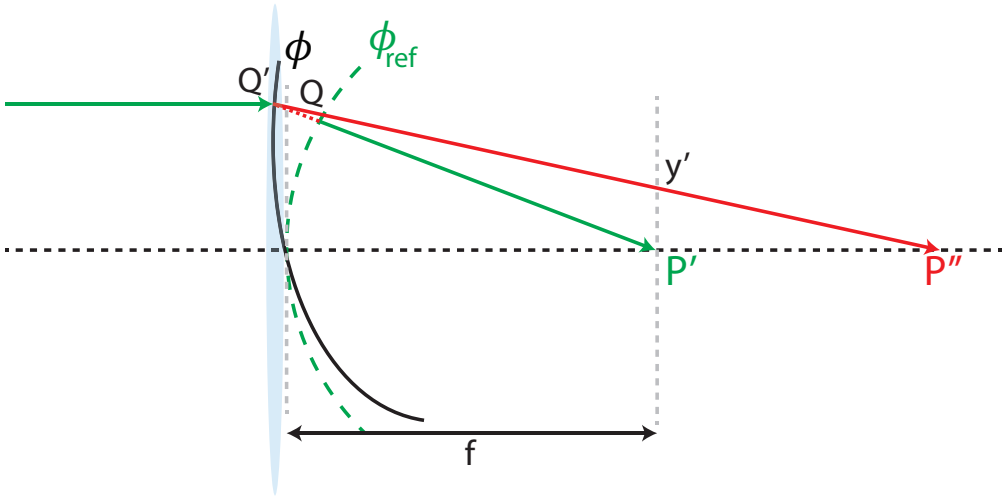

Figure 14: Aberration theory.

An ideal ray shown in green is refracted by a lens and is imaged on to point P' in the focal plane. The wavefront ϕ_{ref} associated with the ideal focusing system is a circle centered on the point P'. For a system that is aberrated, the wavefront ϕ deviates from the ideal as shown in the solid black curve. The ray asociated with the aberrated wavefront focuses to a point P''. At the focal plane, the aberrated ray is seen to deviate a distance of y' from the ideal focus.

Figure 14 shows the typical setup involving a lens that is forming a focus at its focal plane. In the ideal case, the wavefront just to the right of the lens would be 'perfect' and is denoted in green as $\phi_{ref}(x, y)$. The rays associated with this ideal wavefront will focus at the point P' while the rays associated with another (aberrated) wavefront ϕ will focus at a point P'' axially displaced from the focal point. At the focal plane, the aberrated ray has deviated a distance y' from the focus. This deviation is known as the ray aberration of the system. The departure from the ideal behavior can also be characterized in terms of a wave aberration. Although this is less intuitive, this work will characterize aberrations in terms of the wave aberrations as such an approach leads to an intuitive

description of wavefront correction. The aberration ϕ_{abr} is then seen as a deviation from the ideal and is characterized by the additional optical path length QQ' rays will travel between the ideal wavefront ϕ_{ref} and ϕ [30]. It is useful to know the functional form of ϕ_{ref}. This can be achieved in several ways. One approach is to place a virtual point-source emitting a paraxial spherical wave at the focus and compute the wavefront of the emitted wave at the lens plane. Then ϕ_{ref} is given by the following.

$$\phi_{ref}(x,y) = \frac{x^2+y^2}{2f} \qquad (2.2)$$

Note that the above can also be obtained by considering the transmission function of a thin lens under the paraxial approximation. This work utilizes a Gaussian beam from a laser to excite fluorescence. The wavefront of a Gaussian beam after the lens is also given by the above equation when $\left(\frac{z_0}{f}\right)^2 \ll 1$, which is usually true for microscopy. Here z_0 is the confocal parameter of the beam and f is the focal lens of the objective. The reference wavefront ϕ_{ref} is then then a circle with the center located at the focal point. As a result, the reference wavefront is typically referred to as the Gaussian reference sphere. The term 'Gaussian' used in this context has no relation to Gaussian beams but relates to the image point predicted by ray optics.

The challenge of performing wavefront correction is in correctly determining the wavefront ϕ at some plane in the imaging system. While one option would be to use wave models to compute the wavefront, In the limit of $\lambda \to 0$, ϕ becomes equivalent to the eikonal in ray-optics [6]. Provided this assumption is valid, it is possible to use ray propagation to compute the ϕ. Later sections will provide some computations made under this assumption.

2.2.2 Generalized pupil model, sample induced error and wavefront correction

Figure 14 depicts the situation where the incoming beam is aberrated. However, the aberrations in many cases originate from the sample, which is placed after the lens. It is then useful to have a model that describes all aberrations of the system. This is achieved using the generalized pupil model [8]. In this model, all aberrations from the system are lumped together as a single aberration described at some plane in the system (usually the entrance or exit pupil). Under this model, wavefront ϕ would now describe the wavefront associated with propagating the beam through both the system and the sample.

Then the field at the pupil is a product of several factors as shown below. $\mathbb{P}(x, y)$, known as the pupil function is a term containing the physical aperture of the lens as well as the input-beam amplitude and phase distribution (this will be Gaussian in most cases). ϕ_{abr} describes the wavefront aberration of *all* elements in the beam path and ϕ_{mod} is an additional wavefront modulation term associated with a wavefront correction element.

$$\mathbb{P}(x, y) = P(x, y)exp(-ik\phi_{abr})exp(-ik\phi_{mod}) \quad (2.3)$$

Here $P(x, y)$ is the input field multiplied by a function describing the physical dimensions of the aperture. For an input beam of uniform intensity and with a flat wavefront, $P(x, y)$ is a circle function. The behavior of the system can then be modeled using a diffraction model. This can be easily achieved with the Fourier transform based models presented in Chapter 1. Figure 15 shows a pictorial description of the model and its meaning. As shown in figure 15(a), in an ideal system, there is no wavefront error and no wavefront correction so $\phi_{abr} = 0 = \phi_{mod}$. In a practical system, there is wavefront aberration ϕ_{abr} but no wavefront correction element so $\phi_{mod} = 0$. In a corrected system, there is a wavefront aberration ϕ_{abr} and ϕ_{mod} is used to cancel out the aberration. Thus wavefront correction is achieved by pre-modulating the excitation light. If

ϕ_{abr} is known, the correction can be chosen as $k * \phi_{mod} = 2\pi - k * \phi_{abr}$ where ϕ is given in units of length.

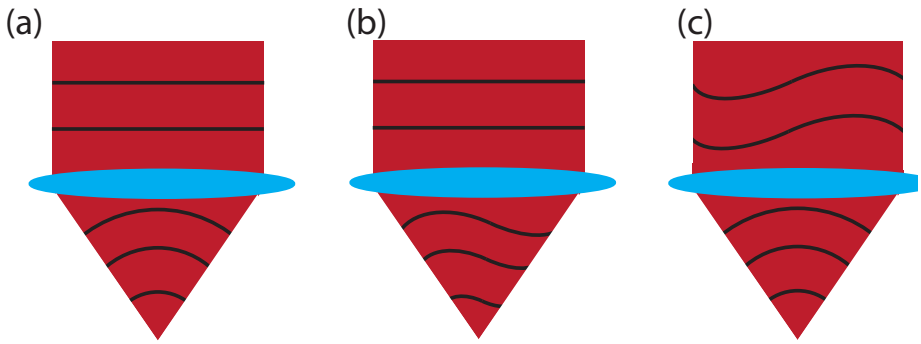

Figure 15: Principle of wavefront correction and the generalized pupil model.

(a) In an ideal system, there are no aberrations (b) In a realistic system, wavefront aberrations are present and degrade the focus quality, (c) In a corrected system, the input wavefront is pre-modulated to minimize wavefront error.

The above approach of computing wavefront error using ray propagation is valid provided the refractive index and the field does not change within a length scale of a wavelength [29]. In the case of scattering, the above assumptions are not true and a different model in the form below is needed [31].

$$E_m^{out} = \sum_n T_{mn} E_n^{in} \qquad (2.4)$$

The above equation represents a transmission matrix based model. T_{mn} is the transmission matrix of the system and its elements are complex in general to account for absorption as well as phase variations. The electric field at some location on the focal plane E_m^{out} can be represented as a superposition of the input field values at all points in the input plane E_n^{in} modulated by the sample dependent transmission matrix elements T_{mn}. Similar to aberration correction, the goal here is to find the phase values of E_{in} that optimize the field at the focus E_i^{out}. While the underlying

mechanisms are different, scattering correction can also be achieved by modulating the input wavefront.

2.2.3 Excitation vs. detection arm aberrations

A general microscope has two pathways: the excitation (or illumination) path and the detection path. In 2PLSM, the detection arm is not set up as an imaging system. That is, the sample is not imaged on the detector. Rather, the detection arm is set up to capture as much light as possible to relay it onto the detector. Therefore, there is not much benefit in performing wavefront correction on the detection arm itself. This work will focus entirely on correcting the excitation arm of the microscope. Other researchers have followed a similar path [32-35].

2.3 Aberrations and their Effects in 2PLSM

2.3.1 Rotationally symmetric aberrations

For a rotationally symmetric system, the wavefront aberration will depend on r^2, y'^2 and $ry'\cos(\theta)$. Here r and θ are the polar coordinates at the pupil and y' is the image height. The form of the aberration function in this case can be determined under the assumption that aberrations are small. Then taking a power series expansion in the above four variables and keeping the lowest non-zero order yields and aberration function of the form below [29, 30].

$$\phi_{abr} = A_s\rho^4 + A_c(y')\rho^3\cos(\theta) + A_a(y')\rho^2\cos^2(\theta) + A_d(y')\rho^2 + A_t(y')\rho\cos(\theta) \quad (2.5)$$

$0 \leq \rho \leq 1$ is the normalized pupil coordinate and θ is the azimuthal angle. The subscripts s,c,a,d and t represent spherical aberration, coma, astigmatism, field curvature and distortion respectively and are known as the fundamental aberrations. Note that all these aberrations, with the exception of spherical aberration, vary with the coordinate y, which is the distance from the origin in the image plane.

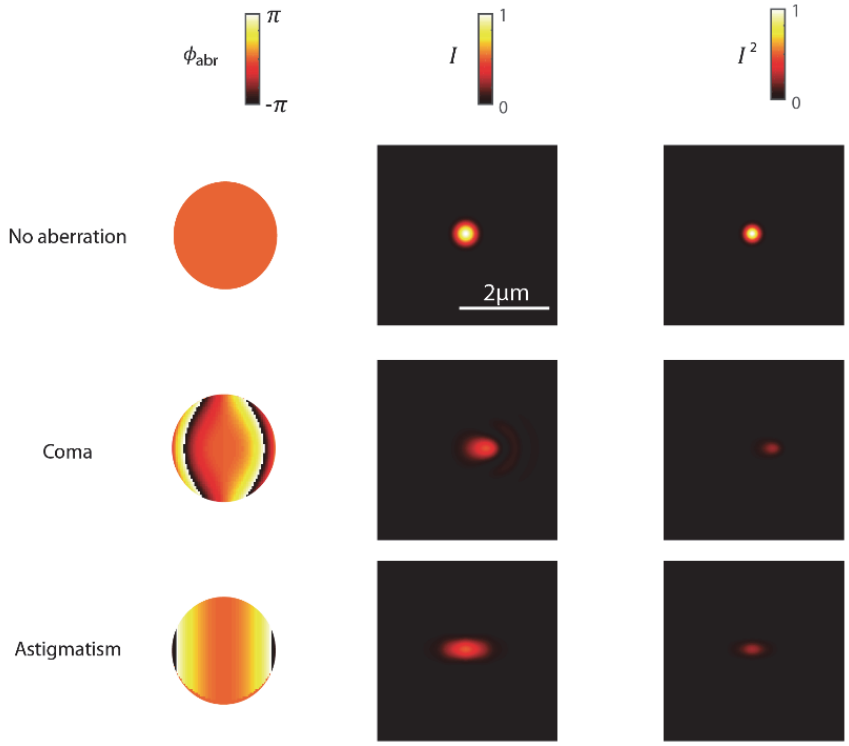

Figure 16: Numerical Simulation of the effect of several primary aberrations.

The figure shows several wavefronts (left column) and their effect on the intensity point-spread-function for single photon (middle column) and two-photon (right column) excitation. In all cases, the 2PEF point-spread-function is more spatially localized compared to single photon excitation. Aberrations lower the intensity and increase the spatial extent of the excitation. Numerically computed using Fresnel diffraction for $\lambda = 800$ nm and NA=0.6 for illumination with a Gaussian beam whose $1/e^2$ width is matched to the pupil size of the objective.

Figure 16 shows two numerically simulated examples of a tightly focused system (numerical aperture = 0.6) with primary aberrations. In all cases, the illumination beam was a Gaussian beam. Fresnel diffraction along with equation 2.3 with ϕ_{abr} chosen to be the functions shown in the left column was used to generate the intensity at the focal plane as shown in the center column. The third column shows I^2, which is proportional to the two-photon excitation point-spread function. It can be seen that in all cases, aberrations reduce the peak intensity and increase the spatial extent of the intensity. While two photon excitation removes some of the extraneous wings caused by the aberrations, there is still a loss of signal and a deformation of the spatial intensity pattern. It can

then be expected that aberrations in 2PLSM will result in decreased fluorescence and reduced resolution.

2.3.2 Wavefront perturbations that are not aberrations

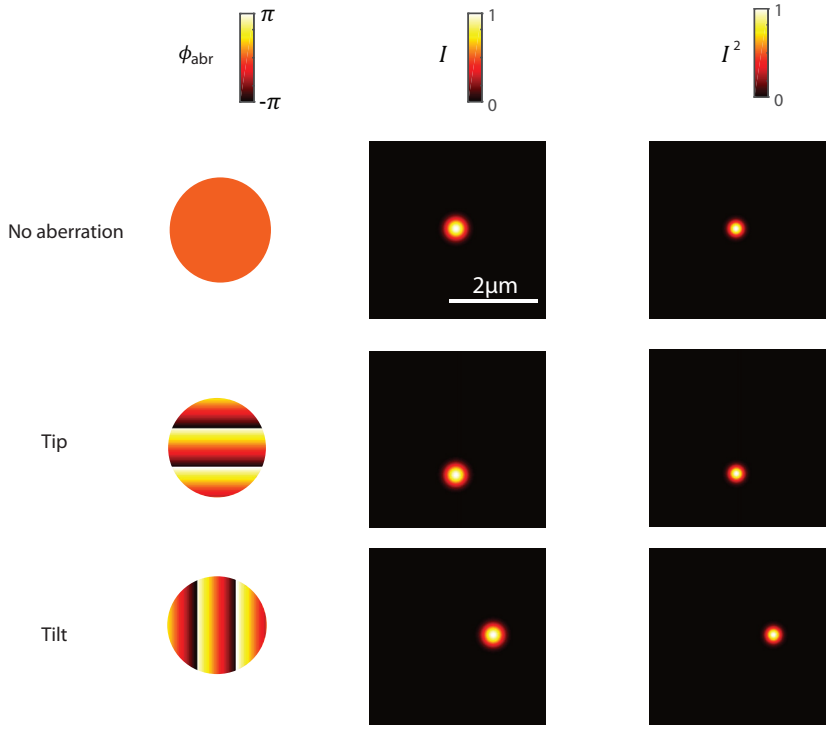

Figure 17: Numerical Simulation of effect of tip and tilt perturbations.

The intensity point-spread-function for single photon (middle column) and two-photon (right column) excitation in the presence of the wavefront perturbation shown in the left column. These perturbations yield pure beam translations and are not considered aberrations in the case of 2PLSM. Numerically computed using Fresnel diffraction for $\lambda = 800\ nm$ and NA=0.6 for illumination with a Gaussian beam whose $1/e^2$ width is matched to the pupil size of the objective.

It was shown above that wavefront aberrations are detrimental to two photon microscopy. However, it should be noted that not all wavefront perturbations are detrimental. Several wavefront perturbations of lower order than the ones presented above can be represented by a series as follows.

$$\phi_t = a_{tip}\,\rho cos\theta + a_{tilt}\rho\, sin(\theta) + a_d\rho^2 + p \quad (2.6)$$

Here the coefficients a_{tip} , a_{tilt} and a_d represent the wavefront perturbations associated with tip, tilt and defocus terms in the wavefront. The term p is a constant phase offset. The first three terms translate the focal spot in the x, y and z-planes respectively. Given that these are pure translation terms, these perturbations do not change the magnitude and the spatial distribution of light intensity and will not be considered aberrations in the case of 2PLSM. Figure 17 shows the effect of tip and tilt on the beam focus. It can be seen that the beam experiences a pure translation effect without change to the magnitude and spatial distribution of the intensity. While not shown, a similar effect can be shown for defocus, which will cause the beam to translate along the z-axis.

2.4 Determining the wavefront aberration

Performing wavefront correction requires the knowledge of the wavefront aberration ϕ_{abr}. Many methods of measuring or estimating ϕ_{abr} have been developed. The most common and direct way of obtaining ϕ_{abr} is through direct wavefront sensing.

For aberrations that can be considered small perturbations of the ideal wavefront, the most common method of determining ϕ_{abr} is through wavefront sensing. Figure 18 shows two different wavefront sensing schemes. In figure 18(a), a transillumination setup allows detecting the aberrated wavefront by placing a wavefront sensor on the transmission side of the system. This approach can be used for transmissive imaging systems. 2PLSM, on the other hand uses an epifluorescence detection scheme, where the fluorescence originating from deep within the sample is detected from the surface. Hence the method shown in figure 18(a) is not compatible with 2PLSM. A different approach that would accommodate wavefront sensing with 2PLSM is to excite a point source in the sample and detect the wavefront of the exiting light with a wavefront sensor [35, 36].

2.4.1 *Wavefront sensing*

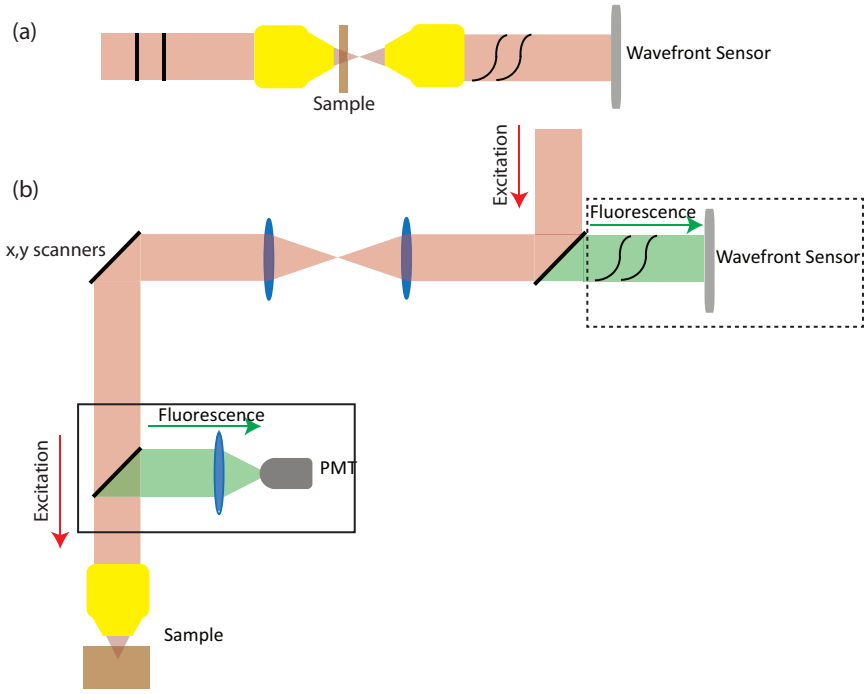

Figure 18: Wavefront-sensing setup.

(a) For a transillumination geometry. The wavefront aberration can be measured directly with a wavefront sensor placed in the detection beam path. (b) For an epifluorescence geometry. Fluorescence coming from a point-like source needs to be utilized for wavefront detection. The microscope requires modification so that fluorescent light is de-scanned by the scanning mirrors before being sent to a wavefront sensor. The solid box represents the typical detection arm of the microscope and the dotted square represents the additional detection arm needed to perform wavefront sensing.

One possible beam path for such a setup is shown in figure 18(b). While this approach has been demonstrated, there are two limitations of this approach. The first is that the detection arm of the microscope has to be significantly changed to incorporate a wavefront sensor. As can be seen by the solid box in figure 18(b), the detection arm of a 2PLSM is simple. In order to perform wavefront sensing, the fluorescent light has to be de-scanned by the scanning mirrors and a wavefront sensor has to be incorporated into the beam path.

Secondly, the fluorescent light is usually in the visible wavelength range and suffers from a lot more scattering than the near infrared excitation light. Hence, wavefront sensing for 2PLSM of

scattering samples requires fluorophores which emit in the red or the near infrared part of the spectrum [37].

2.4.2 Wavefront-sensorless methods

Another approach to determining ϕ_{abr} involves completely eliminating the modification to the detection arm and instead utilizing properties of the microscope images to determine the aberration. Given that these methods do not require implementation of a wavefront sensor, they offer a wavefront correction ability that can be easily implemented. Given there is no direct wavefront measurement, wavefront sensorless methods utilize a feedback signal from the microscope to determine the wavefront. Depending on the general approach, these methods can be seen as two different approaches. In 'local' schemes, the aberration is determined in a small part of the pupil at a time. In 'modal' schemes, the wavefront is represented by a series of functions. The differences are diagrammatically presented in figure 19.

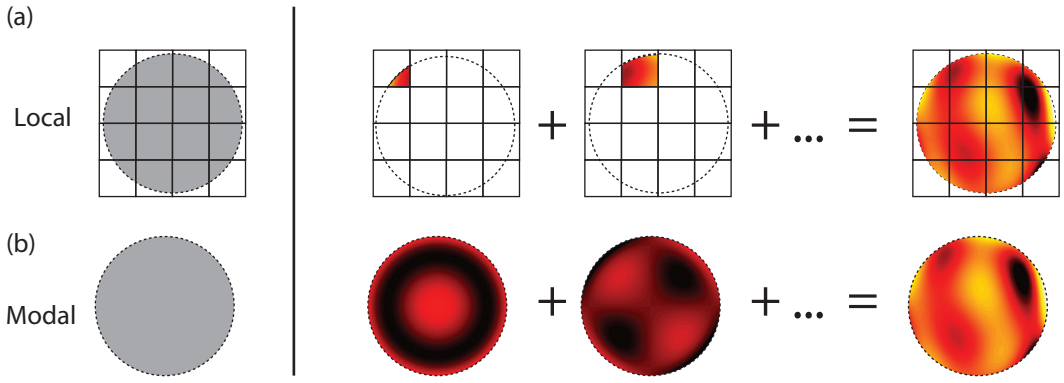

Figure 19: Local and modal wavefront construction.

(a) Local methods. The wavefront is estimated locally. Each step of the algorithm estimates the wavefront in each 'zone', usually on a square grid. (b) Modal methods. The wavefront is estimated globally and expressed as a sum of a set of functions. Each step of the algorithm determines the coefficient associated with each function.

As shown in figure 19(a), the local determination methods assume that the wavefront can be represented locally in the form below.

$$\phi_{mod}(x,y) \approx c_1 + c_2 x + c_3 y + higher\ order\ terms \quad (2.7)$$

The above approach has a simple physical explanation in terms of ray optics. A wavefront aberration at the exit pupil results in rays deviating from the ideal path. Correcting the wavefront then involves changing the ray angles at the pupil to have them point back to the ideal focus. The relative phase differences encountered by each ray has to be then compensated for a phase offset. The c_1 term represents the phase offset and $c_2 x + c_2 y$ term acts effectively as a prism and changes the ray angles. It has been shown that the relative image displacement when imaging with each sub-region of the pupil can be used to determine the offset terms [38]. This method, along with several of its variants [32, 34] have been used extensively in two-photon microscopy of the mouse brain. The disadvantage of using this method is that optimization method takes about two minutes to finish as enough measurements have to be performed to determine the wavefront at each pupil.

In the limit where the subregion size is made very small, such that each subregion is only one pixel, the local method involves determining the phase offset term c_1 for each pixel. While this would be a time consuming method, multiplexing the measurements by driving each pixel at some temporal frequency allows the determination of the phase through fourier analysis of the measured signal. This approach has yielded wavefront corrections that also compensate for scattering effects [33], with the downside being that the corrections are only valid over a very small region of space. Because of this, correcting a single plane, or a whole volume would take a large amount of time.

On the other hand, the modal approach used in figure 19(b) uses an entirely different approach. Optimization is performed by expanding the aberration in a series of the form below [39, 40].

$$\phi_{mod} = \sum_{i=1}^{N} c_i f_i(x,y) \quad (2.8)$$

Image properties are then used to determine the coefficients c_i associated with each basis functions f_i. The final correction is then a superposition of the basis set. Methods of this nature have been previously demonstrated in ex-vivo biological samples but have not been adapted for in-vivo brain imaging [40, 41].

2.4.3 Liquid Crystal Modulators

The phase modulation element used in this work is a liquid crystal spatial light modulator (LCLSM). The main motivation for using a liquid crystal phase modulator is because such devices offer many pixels (~10^6) at low cost and hence allows many degrees of freedom for controlling the excitation beam. The most commonly used wavefront correction elements for wavefront correction systems that only need a few degrees of freedom are deformable mirrors. While liquid crystal devices provide many degrees of freedom, there are some nuances to their use. This section will establish the fundamentals of wave propagation in liquid crystal as well as the practical aspects of using one in a wavefront correction system.

2.4.3.1 *Wave propagation in uniaxial crystals*

While most of the work presented in this dissertation assume that the optical wave propagates in an isotropic medium, this assumption is not true inside the liquid crystal medium. For a general anisotropic medium, the commonly used dielectric constant ϵ is replaced by a dielectric tensor $\tilde{\epsilon}$. For a uniaxial crystal, solving for normal modes yields two distinct solutions, and the system can be described by two distinct refractive indices n_e and n_o where the 'o' and the 'e' represent the ordinary and extraordinary modes respectively [6]. Figure 20 shows the operation and orientation of a typical liquid crystal modulator pixel.

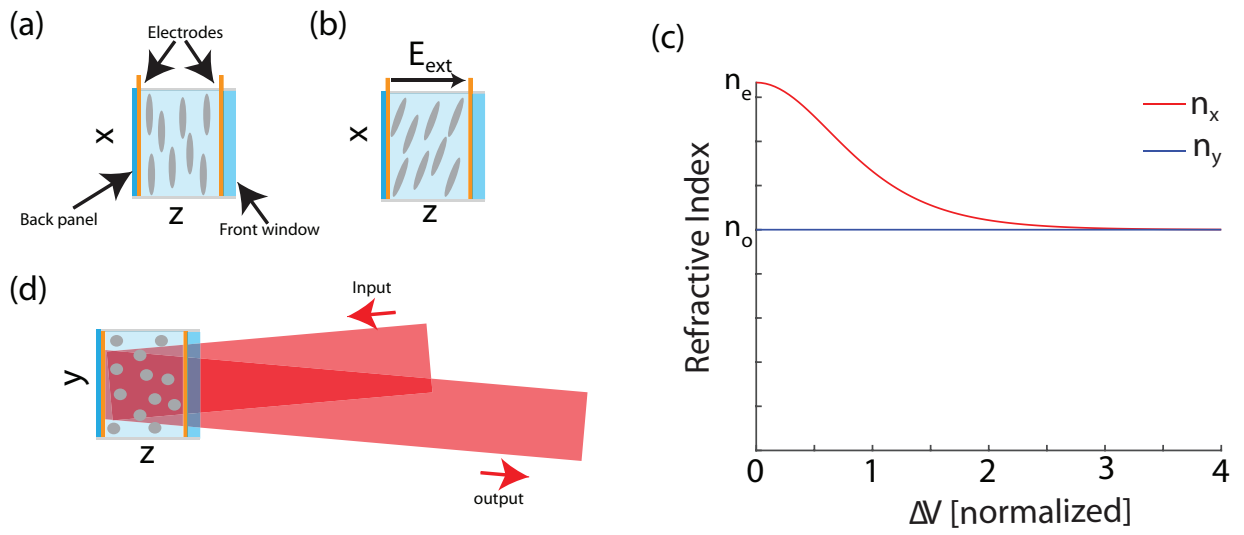

Figure 20: Liquid crystal phase modulators.

(a) Setup of a single pixel showing the orientation of the molecules. The molecules are sandwiched between two plates, with the front plate being transmissive and the back plate being reflective. (b) Operation: When in operation, an electric field is applied in the direction shown, causing the molecules and their optic axis to tilt. (c) The refractive index experienced by the ordinary mode n_x and the extraordinary mode n_y as a function of applied electrode voltage. (d) Optical setup of for a single pixel. The beam is reflected off the back plane at a small angle and the beam traverses the crystal twice.

The ordinary mode experiences a refractive index n_o, as it traverses through the crystal. On the other hand, the refractive index experienced by the extraordinary mode depends on the angle between the crystal's optic axis and the wavevector of the mode. If the crystal's optic axis is pointing in the z' direction (note that this is distinct from the z-axis of the optical system), and the wavevector is $\boldsymbol{k}$, a wave that has polarization normal to the kz' plane will be an ordinary mode [6]. A wave that has polarization along the kz' plane will be the extraordinary mode. In figure 20, the ordinary mode has polarization along the y direction while the extraordinary mode has polarization along the x direction.

With no external electric field applied, the molecules point in the x direction and the extraordinary mode experiences a refractive index n_e. When an external electric field is applied using the electrodes, the molecules, along with their optic axis, tilt due to electrostatic forces. Then the

refractive index experienced by the extraordinary mode can be tuned between n_0 and n_e by the external field.

With a device that allows control of the external field applied to each cell, the phase modulation induced at each pixel can be controlled. The external voltage is applied as an AC signal instead of a static field in order to avoid permanent damage to the device [8]. Because of this, the phase induced by the device oscillates at the driving frequency. This oscillation is usually small and is of little consequence. However, it is a good idea to consider how the oscillation frequency might interact with the operating frequencies of the microscope when designing systems that utilize these modulators.

In most devices, more than a wavelength of phase modulation is achieved by having a reflective back plate and having the beam pass through the crystal twice as shown in figure 20(d). The modulator used for this work is a parallel aligned nematic liquid crystal modulator with 1920x1080 individual pixels. The pixels are addressed similarly to an LCD screen through a digital (DVI or HDMI) video signal from a computer. The device supports a maximum phase resolution of 8 bits which allows 256 individual addressing levels. Because the fill-factor of the device is less than 100%, the device exhibits diffraction losses of about 40%.

2.4.3.2 *Calibration and characterization of liquid crystal modulator*

As shown in figure 20(c), the refractive index, and hence the phase retardation of the modulator is nonlinear in the applied electrode voltage. Accurate representation of pre-computed wavefronts then requires the calibration of the device. Figure 21(a) shows an interferometric setup that was used to characterize the device response. In this setup, a large diameter beam from the laser is split into two beams using a mask (the aperture sizes are large enough to avoid diffraction effects). The resulting two beams are incident on two spatially separated regions of the LCSLM. The reflected

beams are incident on a lens. The lens focuses both beams onto a single location at the focal plane and this plane is imaged onto a camera. While the setup shown in the figure shows the camera directly at the focal plane, a second magnification setup is usually used to magnify the focal region of the lens onto the camera.

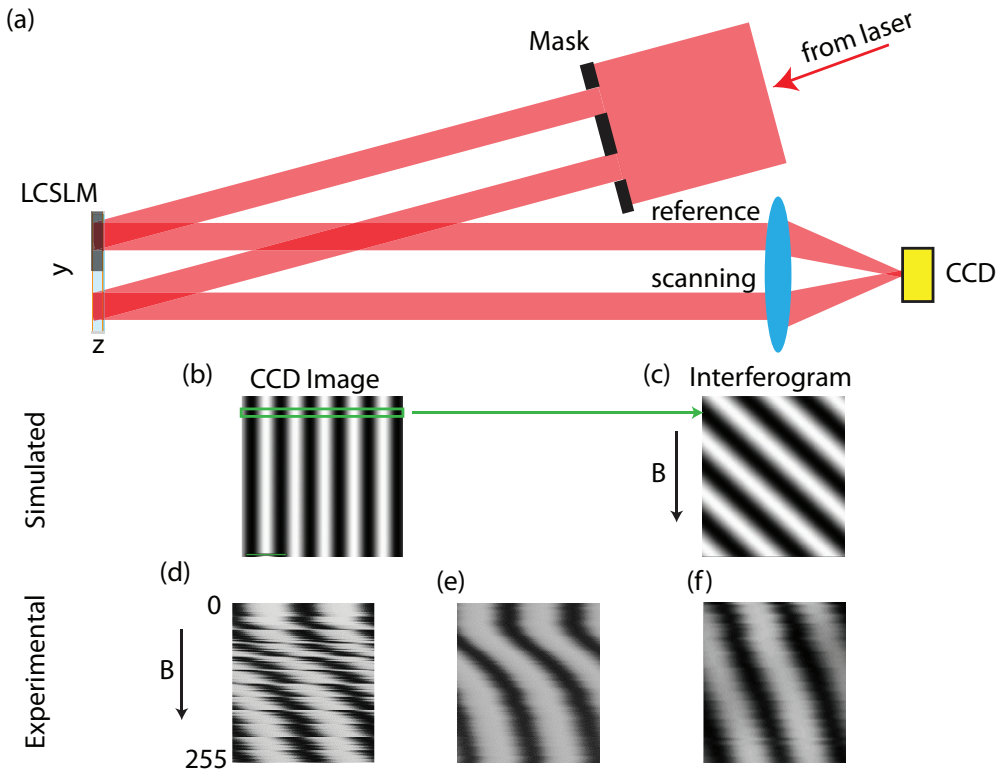

Figure 21: Interferometric characterization of a phase-only LCSLM

. (a) Two beams are made to interfere with using a lens and the resulting interference pattern is imaged. One beam is delayed with respect to the other using the LCSLM. (b) Simulated interference pattern expected near the focus. (c) Simulated interferogram for an LCSLM with a linear response. (d) Experimental interferogram from a defective LCSLM showing a discontinuous phase response. (e) Experimental interferogram from an LCSLM before linearization. (c) The nominally linear phase response from the same LCSLM after linearization achieved by changing the minimum and maximum electrode potentials as well as utilizing a look-up-table.)

Both beams are polarized so that they operate as extraordinary waves inside the LCSLM. However, during the characterization measurement, only one-half of the LCSLM is addressed so that the 'reference beam' experiences a constant phase delay while the 'scanning beam' experiences a controllable phase delay. At the focus of the lens, the field is given by a superposition of the two beams which are delayed with respect to each other. Because the beams are incident on the detector

at an angle to each other, this yields a spatially varying interference pattern. The interference pattern can be computed as follows. While the beamlets pick-up a quadratic wavefront at the lens plane, the radius-of-curvature of the wavefront will be very small near the focus and the beam. In addition, if the beam diameter is much smaller than the lens aperture, the focal extent of the beams will be large. In this case, they can be treated as plane waves near the focus and the interference pattern recorded on the camera be given by $I(x,y) \propto |\exp[-i(\boldsymbol{k_1} \cdot \boldsymbol{r})] + \exp[-i(\boldsymbol{k_2} \cdot \boldsymbol{r} + \Phi_{mod})]\,|^2$ where $|\quad|^2$ implies the complex conjugate product and Φ_{mod} is the phase delay (in units of radians) introduced to the scanning beam by the LCSLM and $\boldsymbol{k_1}$ and $\boldsymbol{k_2}$ are the wavevectors of the two beams near the focus. The interference pattern takes the form below.

$$I \propto 1 + \cos[2ksin(\alpha)y + \Phi_{mod}] \quad (2.9)$$

Here, α is the angle between each beam and the z-axis. The simulated interference pattern is shown in figure 21(b). As equation 2.9 implies, delaying the scanning beam by a wave shifts the interference fringes by a full period. For analysis, one line of the interference fringe is plotted against the addressed bit-value of the modulator as shown in figure 21(c). An interferogram of this nature can be used to determine the linearity as well as the maximum phase response. Figure 21(d) shows the interferogram associated with a defective LCSLM with a discontinuous response. Figure 21(e) shows a similar image for an uncalibrated LCSLM with a continuous phase response. Figure 21(f) shows the same device after calibration. The first step in calibrating a device is to first obtain the response shown in figure 21(e). The information can then be used to adjust the minimum and maximum potential difference to apply to the device to obtain an approximately linear region with a single wave of phase retardation. A second measurement is then performed and the information is used to generate look-up-table that delivers a linear response.

2.4.4 Wavefront modulation experimental setup design

This section details the process of introducing a wavefront correction arm to a standard 2PLSM. As mentioned previously, wavefront correction is achieved by establishing the wavefront error function ϕ_{abr} at some plane in the microscope and then adding a modulation term ϕ_{mod} that compensates for the wavefront error. This is usually done by introducing the wavefront modulation term into the entrance pupil of the objective.

There are several constraints to be met when designing the optical setup for wavefront modulation. Given that the objectives used for 2PLSM are infinity corrected, one requirement is that the beam entering the objective is collimated. This was introduced as the *collimation condition* in Chapter 1. A second constraint is that the phase modulator, typically being a reflective device, cannot be placed exactly at the objective back aperture. The strategy is then to place the modulator at another location and image it onto the back aperture of the objective. In addition, the x and y scanning mirrors are also imaged on the back aperture and in effect, the system acts as if the scanning mirrors and the modulator were all placed directly at the back aperture of the objective. This condition will be referred to as the *imaging condition*. The third constraint is the *beam size constraint*. In order limit the energy density at the modulator, and in order to sample the excitation beam well with the modulator pixels, the beam has to be expanded on the modulator itself. Also, the beam diameter at the back aperture of the objective determines the effective excitation numerical aperture and achieving high-resolution imaging requires a high fill-factor of the objective back aperture. This would mean that the beam diameter at the modulator and the back aperture of the objective have to be carefully planned. Figure 22 shows the beam path which was designed to meet all of the above constraints.

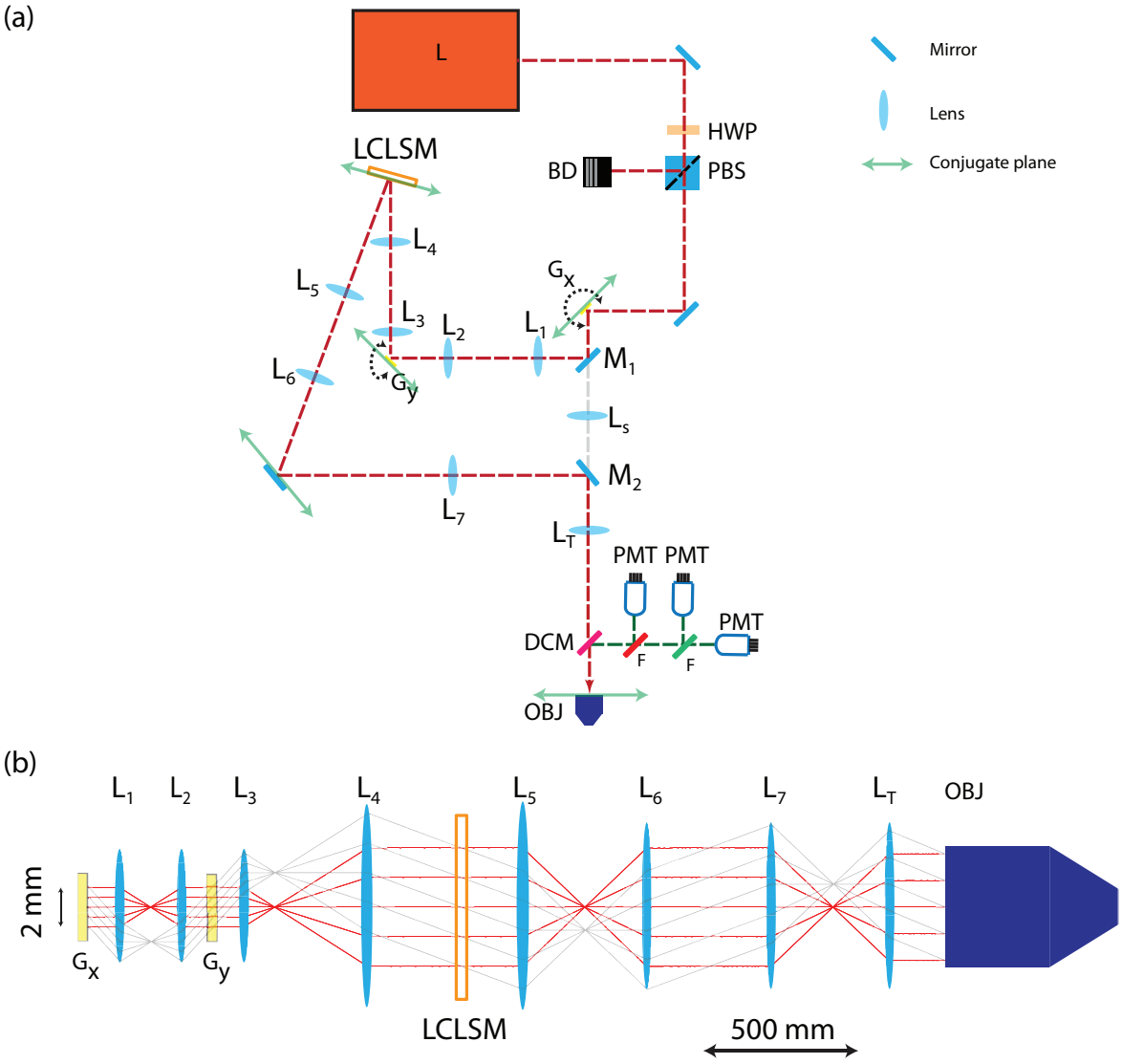

Figure 22: Beam path and ray trace for 2PLSM wavefront correction.

The beam path from the laser (L) up to mirror M1 is the original microscope setup. The half-wave plate (HWP) the polarizing beam splitter (PBS) and the beam dump (BD) forms an attenuator. Removing mirrors M1 and M2 returns the microscope to its original beam path that does not perform wavefront modulation. Adding mirrors M1 and M2 adds wavefront modulation to the excitation beam. The lens pairs (L1,L2), (L3,L4), (L5,L6) and (L7,LT) each form a telescope. The detection arm was not changed. (b) Ray diagram showing how the system meets all of the constraints. The collimation condition is met because each lens pair forms a telescope, and the beam at the objective is collimated. The imaging condition is made possible by imaging the x-scanning mirror onto the y-scanning mirror, which is imaged on to the LCLSM, which is imaged onto the back aperture of the objective. The focal lengths of the lenses were chosen to meet the beam size constraint. The incoming beam is magnified to slightly underfill the LCLSM and is demagnified again to just fill the back aperture of the objective. Note that for (b), the scaling between the two dimensions is not equal in the figure.

An existing 2PLSM was modified to add wavefront modulation capabilities in such a way that the constraints discussed above are satisfied. For the additional beam path elements as shown in figure 22(a), each lens pair forms a telescope. This ensures that a collimated beam going in comes out as a collimated beam. As shown by the green arrows, each telescope images one optic onto the other. For example, the x-scanning mirror is imaged on the y-scanning mirror. The focal lengths of the lenses were chosen to magnify or demagnify the beam size as needed. The pairs (L1,L2) (L5,L6) deliver a magnification of 1. The pair (L3,L4) deliver a magnification of 3, while the pair (L7,LT) deliver a magnification of 0.9. This ensures that a 2 mm beam at the scanner is expanded to be 6 mm at the LCSLM, and demagnified again at the objective back aperture to a diameter of 5.4 mm. The LCSLM is a phase only modulator (Pluto, Holoeye Photonics).

Figure 22(b) also demonstrates how the 'imaging condition' is met. The ray diagram, which was generated using ABCD matrix propagation, shows that beam position and angle at each plane in the imaging system. The red trace in Figure 22(b) shows the beam when it is parallel to the optical axis and the gray ray trace shows the beam when it is tilted at an angle. At the scanning mirrors, the LCSLM and the objective back aperture, the beam can be seen to change direction without any translation indicating that all of these image planes are conjugate to each other. If the LCSLM were placed on a non-conjugate image plane to the scanning mirrors, the beam would translate on the LCSLM and the phase factor introduced by the LCLSM would change as a function of the scan angle. The ray diagram only shows scanning in one dimension but the imaging condition remains true for scanning in both x and y because the x and y scanning mirrors are placed on independent conjugate planes.

In this setup, the LCSLM is slightly underfilled. This removes diffraction effects from the edge of the liquid crystal region and also increases the throughput of the system. The beam slightly overfills the objective (Olympus LUMPlan FLN 60x, NA = 1.0, water immersion) which ensure high effective excitation numerical aperture. The lenses used were achromatic doublets with design wavelengths of 706.5 nm, 855 nm and 1015 nm. Note that real lenses deviate significantly from the thin lens ray diagram shown in figure 22(b). The thin lens model was used as a starting point and the actual experimental setup took into account the thickness of the lenses. The LCSLM itself generates multiple diffraction orders related to its fill-factor being less than 100%. These higher order diffraction orders do not propagate through to the objective.

Excitation light was provided by a mode-locked Ti:Sapphire laser (Mai Tai HP DeepSee, Spectra Physics). The pulse repetition rate was ~80 MHz with a pulse width of ~100 fs. Emitted fluorescence signal is detected using three PMTs (R3896, Hamamatsu) separated by dichroic filters to detect three spectral bands (<505 nm, 505-560 nm and 560-690 nm). The signal from each PMT was converted to a voltage and filtered using a transimpedance amplifier (SR570, Stanford Research), and digitized via an analog to digital converter (PCI 6133, National Instruments).

Finally, the addition of additional components to the system can increase can increase the pulse-width at the sample through dispersion effects. After the final beam path was setup, the onboard dispersion compensator of the laser was adjusted to minimize the pulse-width at the sample at selected wavelengths in the tuning range of the laser.

2.5 Development of a new optimization scheme for in-vivo brain imaging

While several 2PLSM wavefront optimization schemes based on a wavefront-sensorless approach have been methods demonstrated so far, they have suffered from limitations such as requiring serial image acquisition [38], requiring the introduction of fluorescent beads to measure image displacement [32], long optimization times [32, 34] or have generated corrections that are valid over only a small volume [33]. This goal of this work is to achieve a wavefront optimization scheme that is fast and simple enough to be used for routine mouse brain imaging.

2.5.1 Numerical Simulations of Aberrations: Arguments for Modal Optimization

It is useful to analyze the optical setup commonly used for two-photon imaging of the mouse brain to understand common sources of aberrations. This section aims to approximate the wavefront aberration that is likely to be encountered during mouse brain imaging. In the limit of geometric optics, the wavefront difference of a ray bundle propagating from point a point P_1 to another point P_2 can be calculated as $\phi(P_2) = \phi(P_1) + OPL$. The OPL function denotes the optical path length and can be computed using the following relation [29].

$$OPL = \int_{P_1}^{P_2} n\, dr \quad (2.10)$$

The integration is performed along the ray trajectory from P_1 to P_2 and takes into account the local refractive index. For a homogenous medium, the trajectory can be shown to be a straight line. Since the aberration is a deviation from the ideal wavefront, the aberration is computed as the difference of the optical path length of the actual ray compared to an ideal reference ray. Equivalently, the aberration is the deviation of the wavefront from the reference sphere. The wave aberration ϕ_{abr} in units of length is given by $\phi_{abr} = OPD$, where OPD is the optical path length

difference with respect to the unaberrated ray. The wave aberration in units of radians can be computed using the following relation.

$$\Phi_{abr} = \frac{2\pi}{\lambda} OPD \quad (2.11)$$

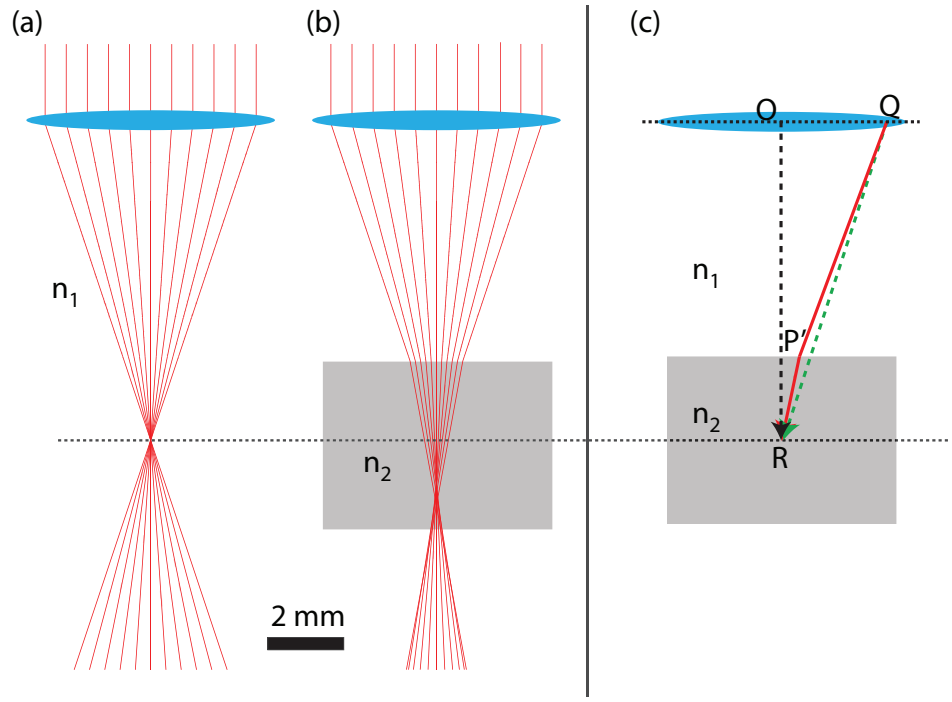

Figure 23: Ray and wave aberration modeling.

(a) A diffraction limited ray bundle focuses to a single point after a thin lens (b) Adding refractive index mismatch to the sample causes the rays to focus at various depths. The ray deviation at the focal plane is the ray aberration. (c) Wave aberration computation for the same system. The aberrated wavefront is given by the optical path length of the ray QP′R computed at all points on the lens plane. The reference wavefront is described by the ray QR in the absence of the refractive index mismatch.

Figure 23 shows an example of an aberrated ray bundle. Figure 23(a) shows a high numerical aperture beam focused by a f=9 mm thin lens in a medium of refractive index n_1. The ray diagram shows the rays focusing to a single point at the focal plane, indicating no aberrations. Figure 23(b) shows the same beam, with the sample being modified so that the beam is focused inside a region of the sample with refractive index n_2, with $n_2 > n_1$. In this case, the ray deviates from the focal point laterally at the focal plane, which is indicative of aberrations. In addition, the rays close to

the optical axis and the rays further away from the optical axis focus to different axial locations. This type of aberration is very common and can be found in systems where a diverging or converging beam traverses a flat refractive index boundary. While figure 23(b) shows the ray aberrations, the quantity that is needed for wavefront correction is the wave aberration.

The wave aberration can be computed by the OPD function described above. This process is described in figure 23(c). For an aberration free system, the optical path length of ray OR must match the optical path length of ray QR. For a paraxial system, the lens imparts a quadratic wavefront that causes the system to meet this condition. When introducing the interface with refractive index n_2, the optical path length from the focal point to the point Q is now given by ray $QP'R$. The wavefront can then be generated by computing the OPL for the ray $QP'R$ at all points on the pupil.

While the mouse brain itself is expected to be non-homogenous, a basic aberration model can be constructed under some assumptions. The optical setup for in-vivo brain imaging can be seen in figure 24(a). Access to the brain is achieved by removing the skull and implanting a window. The window has dual purposes – it provides optical access to the brain and also provides motion stability since unrestrained brain tissue can move around due to the heartbeat. The windows itself is made with a thin microscope coverglass. Right underneath the window is artificial cerebrospinal fluid, an aqueous medium. Water is placed between the window and the water-immersion imaging objective.

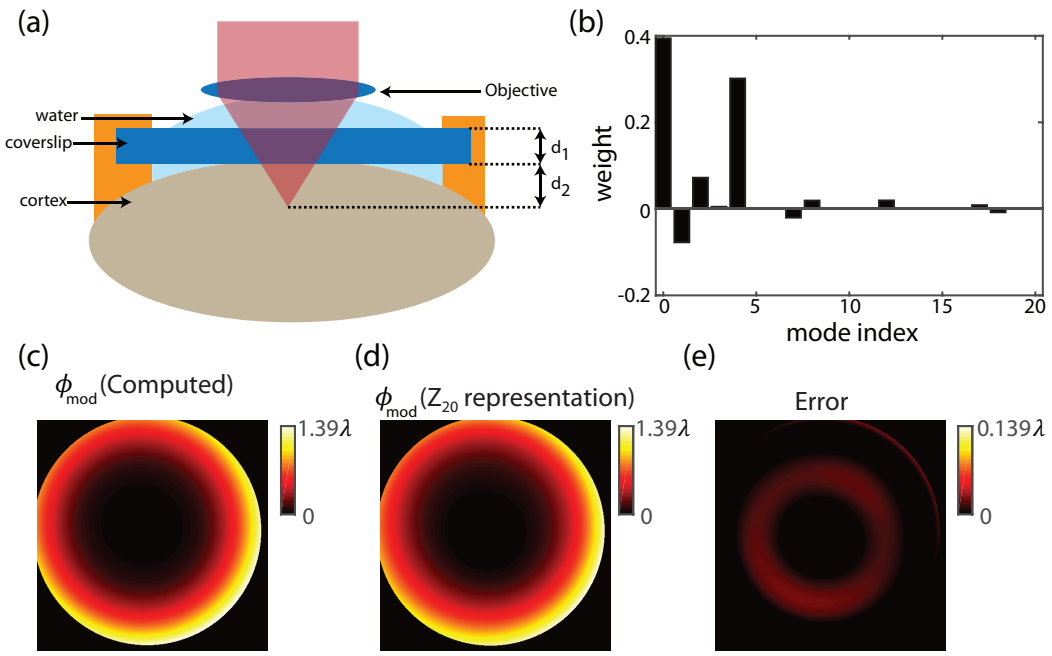

Figure 24: Numerical simulations of cranial window aberrations.

(a) The setup. A thin lens focuses a beam through a coverslip into the cortex. For the simulation $d_1 = 160\ \mu m$ and $d_2 = 150\ \mu m$ and focal length f=9 mm. The beam experiences a refractive index boundary as travels from the water into the coverslip and the coverslip into the brain. $n_w = 1.33, n_1 = 1.5, n_2 = 1.37$. The coverslip was tilted by 2° in each dimension. The distance from the lens place to the focus is 9 mm, and the numerical aperture of the source is ~ 0.9. (c) Computed aberration referenced to the reference sphere. (d) The computed aberration expressed as superposition of the first 20 Zernike modes. (e) The error between the original function and the Zernike representation.

The excitation beam must traverse the window before it can reach the brain. As evidenced by the equation 2.11, the magnitude of aberrations is related to the optical path length difference. Since the refractive index of glass is approximately 1.5 and the background refractive index of water is 1.33 and the average refractive index of the brain is 1.37 [42], the glass window itself can introduce significant aberrations. Given that the glass window is approximately 160 μm thick, it can be expected that the window induced aberrations will be the dominant effect when imaging at shallow depths.

In order to study the types of aberrations induced by the window, a numerical simulation was performed using commercial software (Zemax). The optical system was setup as shown in figure 24(a). The aberration associated with imaging a depth of 150 μm brain through a glass window of

160 μm thickness and tilted 2 degrees in each dimension was computed. The wavefront aberration computed in reference to the reference sphere was conjugated to obtain the related correction function ϕ_{mod} and is shown in figure 24(c).

While it is possible to perform blind optimization, it would greatly simplify the optimization process if the aberration could be represented in a small number of basis function so that a modal optimization scheme could be utilized. Since the Zernike basis is often used to represent aberrations [29], and since this basis has been used in modal optimization schemes before [40, 43], it is of interest to investigate the utility of this basis for in-vivo mouse brain imaging. The definition of Zernike functions is provided in section 2.7.

The aberration function was expanded as a superposition of Zernike function so that $\phi_{abr} = \sum_{k=1}^{N} c_k Z_k(x, y)$, and Z_k represents the k[th] Zernike function. The analytical form of Zernike functions make up a complete orthogonal basis. The coefficients k_i were estimated by numerically computing the inner product $k_i = \langle \phi_{abr}, Z_i \rangle$, assuming that the discrete Zernike functions are also orthogonal. Note that the completeness and orthogonality of discrete Zernike functions is an actively researched topic and is beyond the scope of this work [44]. For the representation, the first 20 Zernike coefficients were computed. The wavefronts and the discrete Zernike functions were defined on a 512x512 grid. As seen in figure 24(c), the original function has a maximum wavefront error of approximately 1.4λ and and the wavefront estimation error as shown in Figure 24(e), has error terms that are ten times smaller. In order to quantify the error between the original function and the Zernike representation, the RMS wavefront error was computed using the equation below.

$$\phi_{rms} = \sqrt{\langle \phi^2 \rangle - \langle \phi \rangle^2} \quad (2.12)$$

Here, ⟨ ⟩ implies a spatial average computed over the whole pupil. The RMS wavefront error of the original wavefront aberration ϕ_{abr} is 0.35λ. After correcting with the Zernike approximated correction function, the residual RMS wavefront error is 0.02λ. Thus, it is evident that the aberration arising from the window and index mismatch aberrations in the brain can be readily expressed and corrected using the first 20 Zernike modes.

In terms of the Zernike components, modes 0,1,2 and 4 in figure 24(b) are low order perturbations that do not degrade two-photon excitation and can be ignored. The aberration is then comprised of several components that include astigmatism, coma and spherical aberration. Spherical aberration (mode 12) alone can be corrected using either an objective with a correction collar or an adjustable membrane [45] and is likely to yield significant improvements in beam focusing. A more accurate correction can be performed by correcting other Zernike modes using a spatial light modulator or a deformable mirror device. The next sections will focus entirely on using a modal approach to perform wavefront optimization. figure 25 shows a visual depiction of the first 20 Zernike functions excluding mode 0, which is a constant offset term.

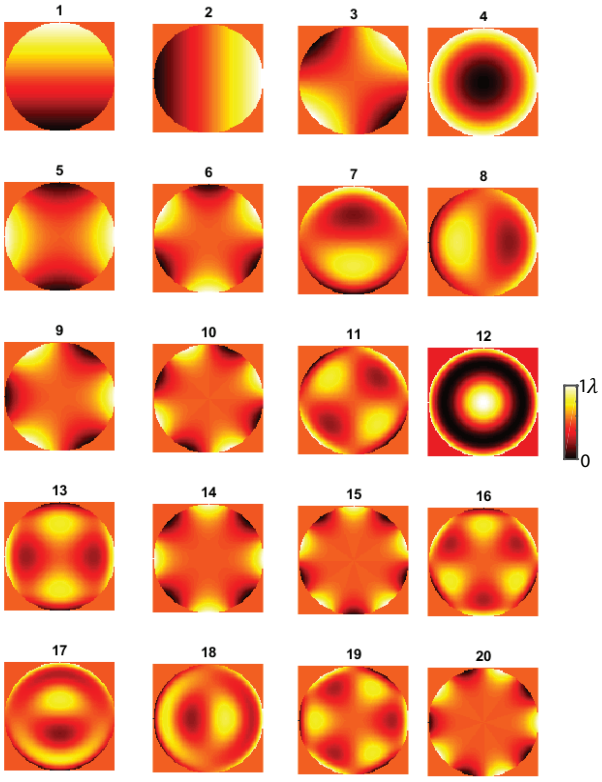

Figure 25: The first 20 Zernike modes (excluding mode 0).

The normalization constant has been ignored in the visual depiction and all function were encoded so that the peak-valley range was 1 wave. Mode 0 (not shown) is a constant offset term.

2.5.2 Demonstration of Two-Photon Excited Fluorescence as a beam quality metric

In order to algorithmically determine the modulation function that compensates for wavefront aberrations, a feedback signal is required. In previous work done on 2-photon wavefront optimization, Ji et al. [32, 38] used a local estimation scheme where they used the images of distinct objects to determine local tip and tilt or used temporal lock-in measurements to determine local wavefront gradient using an interferometric signal [34]. Tang et al. [33] used temporal lock-in measurements of an interferometric signal to determine the phase value at each pixel of the phase

modulator. Debarre et al. developed a method that uses the average two-photon image intensity to determine the wavefront correction in a modal scheme [40].

This section aims to demonstrate how the 2PEF signal can be directly utilized as a feedback signal. For the rest of this section, it will be assumed that the power-loss from the beam due to two-photon absorption is negligible. Assuming the beam is propagating in a medium of constant fluorophore concentration, the fluorescence generated at some given instant in time is given by the following [10, 46]:

$$S_{2P}(x,y,z,t) = \sigma_{2P} c_0 \iiint \; I^2(x,y,z,t)dxdydz \qquad (2.13)$$

where σ_{2P} is the two-photon action cross-section in units of m^4/W, c_0 is the fluorephore concentration and I(x,y,z) is the optical intensity. The measured fluorescence is a spatial integral since the point-detector used in 2PLSM does not offer spatial resolution. Assuming the intensity near the focus is described by a perfect Gaussian beam, the 3-dimensional intensity can be expressed as follows.

$$I(x,y,z,t) = \frac{P(t)}{\pi w^2} \exp\left[-2\left(\frac{x^2+y^2}{w^2}\right)\right] \quad (2.14)$$

Here the instantaneous power $P(t)$ is a function of time since the excitation beam is pulsed. Assuming a square wave pulse, the peak power P_{peak} and the average power P_0 are related by $P_{peak} = \frac{P_0}{f_l \tau_p}$, where f_l is the laser repetition rate and τ_p is the pulse width. The measured signal, even for a single voxel in the image, is averaged over many pulses. Then the measured quantity is the time-averaged fluorescence. Performing a time average of the above equation yields the following.

$$\langle S_{2P} \rangle \propto K_1 \iiint \frac{1}{w^4(z)} \exp\left[-4 * \left(\frac{x^2+y^2}{w^2(z)}\right)\right] dxdydz \quad (2.15)$$

All multiplicative constants have been absorbed into the constant K_1 since for this computation, we are interested in variation of fluorescence and not absolute values. It is assumed that the collection efficiency is does not vary with spatial location near the focal point. The Gaussian beam radius $w(z)$ is a function of the wavelength λ, the beam waist w_0 and the refractive index n. The above relation ignores photobleaching and assumes the excitation intensity is well below saturation. Then the magnitude of the total 2PEF signal for a uniformly labeled sample, as a function of the beam waist w_0 can be computed by numerically integrating the above equation. Similarly, the time averaged single photon excited fluorescence (1PEF) can be computed as,

$$\langle S_{1P} \rangle \propto K_2 \iiint \frac{1}{w^2(z)} \exp\left[-2 \left(\frac{x^2+y^2}{w^2(z)}\right)\right] dxdydz \quad (2.16)$$

The above equations were used to determine how the total fluorescence varies as a function of the beam waist radius w_0 for samples of three different sizes and the results are shown in Figure 26. As shown in Figure 26(d), for a sample that is smaller than the beam waist, both the single photon fluorescence (1PEF) and the two-photon fluorescence decrease with increasing beam-width, with the 2PEF decaying faster with beam width. This shows that in the presence of a point-like sample, both 1PEF and 2PEF magnitude can be used to determine the beam quality, with the fluorescence increasing with tighter focusing. For an object that is approximately the size of a cell, 1PEF is seen to not vary with the beam size. This is because, when the sample is larger than the beam, each plane of the beam generated equal fluorescence, irrespective of beam size. Hence for a cell-like object, 1PEF cannot be used as a feedback signal. On the other-hand, 2PEF originating from a cell-like object is seen to change as a function of beam radius, with tightly focused beams yielding more fluorescence. Hence, 2PEF from a cell can potentially be used as feedback source for beam

optimization. Finally, when the sample is large and uniformly labeled, even 2PEF is seen to not provide a sensitive feedback signal. This shows the limiting case where 2PEF signal no longer forms a useful feedback signal.

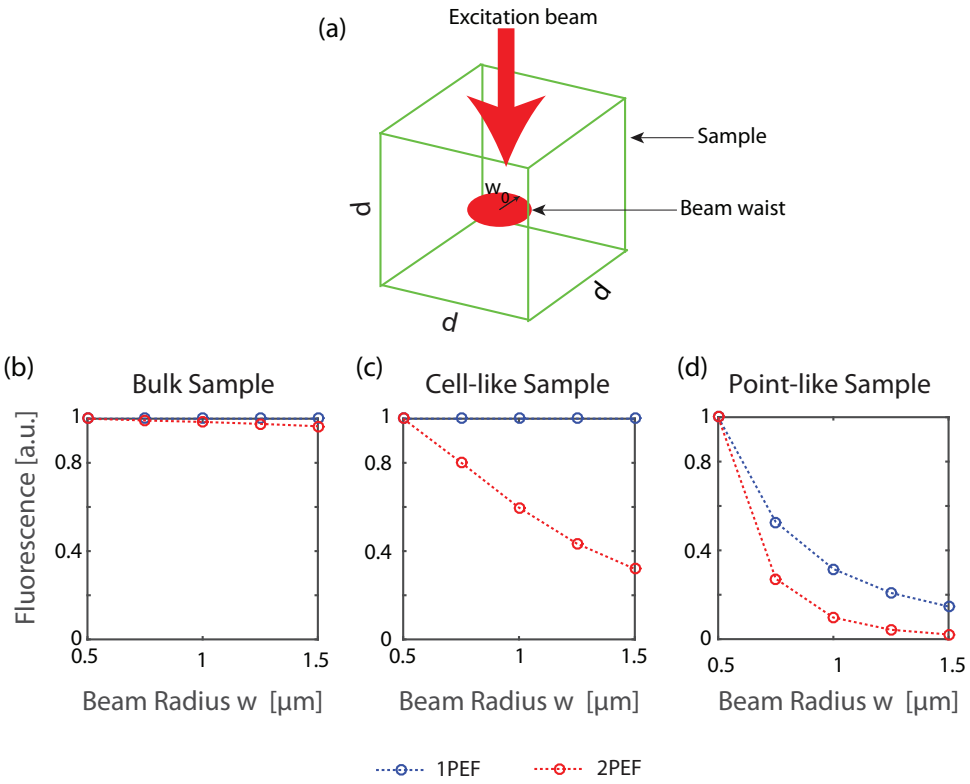

Figure 26: Numerical Simulation: Variation of time and space integrated fluorescence signal with beam size for point excitation with a Gaussian beam.

The fluorescence signal equations were integrated over a cube centered at the beam focus as shown in (a). The length of a cube side d was set to values of 200 μm, 5 μm and 0.25 μm to mimic a bulk sample, a cell-like sample and a point-like sample. The total fluorescence was plotted against beam waist radius in each case and is shown in (b),(c) and (d). Each curve was independently normalized to its maximum value. (b) For a bulk, uniformly labeled sample, 1-photon fluorescence does not vary significantly with beam waist radius while 2-photon fluorescence varies slightly with beam waist radius. (c) 1-photon fluorescence does not vary with beam waist radius for a cell-like object while 2-photon fluorescence varies significantly. (d) For a point-like object, both 1-photon and 2-photon fluorescence varies significantly with beam waist radius. $\lambda = 850$ nm, n=1.33

These results also highlight the inherent advantage of 2PEF over 1PEF for wavefront optimization, since in many cases, the two-photon signal can be used as a metric for determining the tightness

of the beam focus. While not obvious from the above simulations, the time-averaged 2PEF signal is also a function of the pulse-width of the excitation beam at the focus and scales at $1/\tau_p$. Because of this, 2PEF can be used to optimize both the spatial as well as the temporal focusing [47]. The most relevant aspect of this results is that the beam quality can be assessed based entirely on the magnitude of fluorescence and in the absence of explicit spatial information.

Figure 27 shows experimental confirmation of the results obtained above. A high numerical aperture beam ($NA \approx 1$) was focused on a 4 μm diameter fluorescence bead. The fluorescence in generated through 2-photon excitation. The wavefront was modulated by addressing specific Zernike functions (corresponding to mode indices 5,6 and 12) and the change in fluorescence was observed. Addressing was performed by taking each Zernike function (normalization constant was ignored) and encoding it so that the peak-valley phase difference was equal to one wavelength at the LCSLM calibration wavelength of 850 nm. Then addessed the functions were scaled by a weighting constant in the range of -1 to 1. The bead was embedded in epoxy as shown in figure 27(a). Figure 27(b),(c) and (d) show the variation of 2-photon excited fluorescence with weight value described above. It is seen that the fluorescence changes based on the wavefront, indicative of numerical results generated earlier, showing that for a cell-sized object, the 2PEF changes as function wavefront aberrations. Note that the fluorescence variation is not due to power modulation. The LCSLM setup to operate in phase only mode. The inadvertent power modulation was experimentally determined in a separate measument (not shown) to be in the range $\pm 2.3\%$, which translates to a 2PEF signal change of $\pm 5\%$. The changes observed in this experiments and all following experiments far exceed this value, indicating changes due to wavefront modulation.

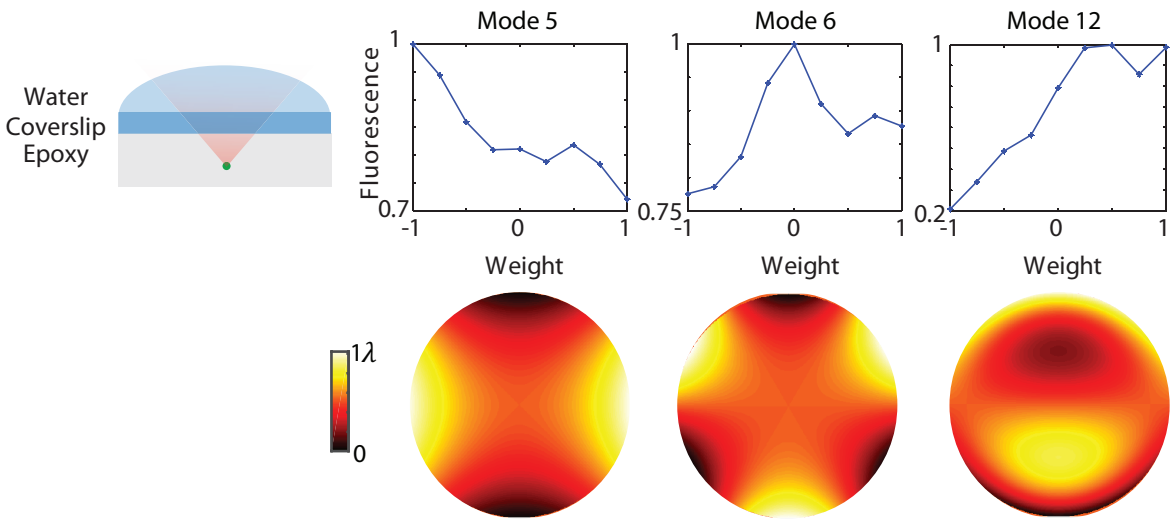

Figure 27: Experiment: 2PEF signal variation with wavefront modulation

.(a) Setup: A 4 μm diameter bead was embedded in epoxy and imaged through a coverslip. Three different Zernike functions shown in (b), (c) and (d) were encoded into wavefronts and were multiplied by a range of weight values before being addressed to the LCSLM. The fluorescence change with weight was measured in each case and shows significant changes. Weight value of zero represents a flat wavefront modulation function. $\lambda_{ex} = 755\ nm$.

2.5.3 Constructing a 2PEF signal based optimization algorithm

2.5.3.1 *A solution to the beam constraining problem*

The previous sections demonstrated that the first 20 Zernike functions can be used to represent window and some brain aberrations. Previous work in 2PLSM modal optimization have relied on image acquisition and have utilized the mean image intensity over a single 2-D plane as an optimization feedback signal. This approach presents some challenges. First of all, in a scattering medium such as mouse brain, at constant excitation power, the 2PEF signal decreases as a function of depth. In densely labeled samples, this approach could simply translate the beam towards the surface, even if the first few Zernike modes which represent lateral and axial translations are excluded from the optimization process. This is because, in general, a wavefront modulation function can translate the beam along any of the 3 axes.

Previous work has focused on preventing beam translation by constraining the addressed wavefront in two different ways. In one approach, the effect of Zernike modes on image formation process was theoretically calculated to remove the cross-talk between modes and to generate a new set of modes [40]. Another approach has been to use standard Zernike functions, but experimentally determine the displacement induced by each function and balance the displacement by adding using the tip, tilt and defocus Zernike modes [43] (corresponding to k=2,3,4) in definitions used in this work.

This work considered another approach to constraining the beam by making use of the numerical and experimental results obtained in the previous section. This approach is based on two signal generation arguments. The first one is that optimization can be performed without image acquisition. The second one is that, near a discrete physical object, the maximum 2PEF is obtained when there is maximal overlap between the beam focus and the object. Hence a discrete object will provide a physical constraint. With this approach, the wavefront optimization system is not designed with a specific set of basis functions in mind, and these can be varied as will be shown later. In addition, in this approach, the optimization process only excites a small reference region of the sample which need not be an experiment critical cell. It will demonsrated later that the discrete object for optimization can be achieved using a the soma of a cell, without requiring the introduction of exogenous signal sources.

2.5.3.2 *Algorithm*

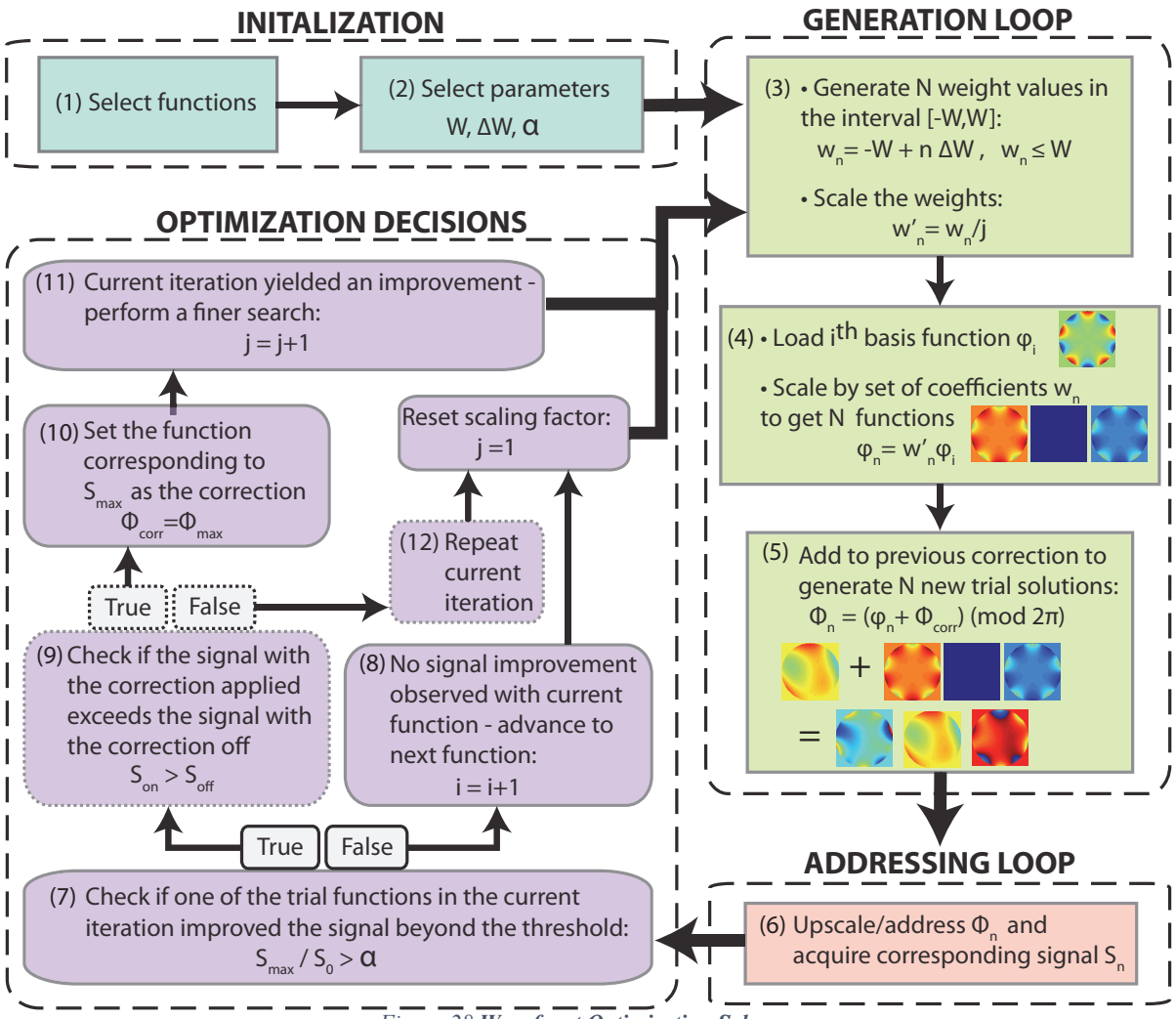

Figure 28 ***Wavefront Optimization Scheme.***

At the beginning, the basis index i and the scale factor j are set to 1. ***Steps 1,2:*** *A set of correction functions and parameters W (maximum weight), ΔW (step size), and α (acceptance threshold are chosen).* ***Step 3:*** *N weight values w_n (which includes 0) are generated based on the parameters set in step 2. These weight values are scaled by an integer j based on the results of the previous iteration.* ***Step 4:*** *The i^{th} basis function is loaded and scaled by the weight values generated above to generate N functions.* ***Step 5:*** *The N functions generated in the previous step are summed with the correction of the previous iteration and phase wrapped to generate N trial solutions Φ_n.* ***Step 6:*** *The functions are up-scaled and addressed one by one and the corresponding 2PEF signal S_i is recorded.* ***Step 7:*** *The ratio between the maximum signal S_{max} to the signal S_0 corresponding to a weight of 0 is compared to α.* ***Step 9:*** *(optional) attempts to detect incorrect decisions caused by signal fluctuations.* ***Step 10-11:*** *If step 7 yielded a positive result, the function corresponding to the maximum signal is set as the current correction and the scaling factor j is incremented by 1. This causes the scheme to perform another optimization cycle using the same basis function but with the weight values scaled by j.* ***Step 8:*** *If step 7 did not yield a positive result, the variable i is incremented and the scale-factor j is reset so that the scheme moves on to the next basis function.*

In our optimization scheme, the system starts off with a flat wavefront as the first estimate for the correction. Each new iteration of the algorithm perturbs the previous correction to generate several new trial wavefronts. The scheme decides whether to accept one of these trial wavefronts as the new correction by comparing the 2PEF signal associated with the new wavefronts with that of the previous correction. In all cases, the 2PEF signal originates from a discrete object inside the sample.

The *acceptance threshold* (α) is an important feature of the scheme presented here. The 2PEF signal, while being a suitable feedback signal, does suffer from signal fluctuations. These are more pronounced during in-vivo experiments due to breathing and heartbeat. One strategy to deal with fluctuations involves increasing integration time to average them out. However, large integration times slow down the optimization process. The inclusion of an *acceptance threshold* allows the wavefront correction system to discard steps that do not measurably improve the solution, and thus ignore signal fluctuations. Only signal changes greater than α are considered valid. For best corrections, α is set to the percentage of fluctuation expected on the measured signal. Inclusion of this allows the scheme to achieve corrections in-vivo based on the signal alone without long signal integration times. To experimentally determine α, a number of 2PEF signal measurements are performed without changing the wavefront addressed to the LCSLM, and the maximum fluctuation compared to the mean is set equal to α .

2.5.3.3 *Standing beam and sweeping beam noise analysis*

This approach provides the versatility of being able to perform optimization in either a *dwelling beam* or a *sweeping beam* configuration, where the beam either dwells at a single point or is swept across a small (~10 μm x 10 μm) region during optimization. Figure 29 shows a comparison of the frequency spectrum of the measured fluorescence signal under the two methods. Compared to

the dwelling beam approach, the scanning beam approach introduces signal fluctuations at high frequencies. The dwelling beam approach delivers superior SNR, while the sweeping beam approach is useful for avoiding photobleaching and photodamaging a single point. We note that it is important for the sweeping beam to scan only a small area encompassing a single cell to avoid unpredictable beam translation effects and that the laser power used here is much less than that used in wavefront correction schemes that require sequential acquisition of images.

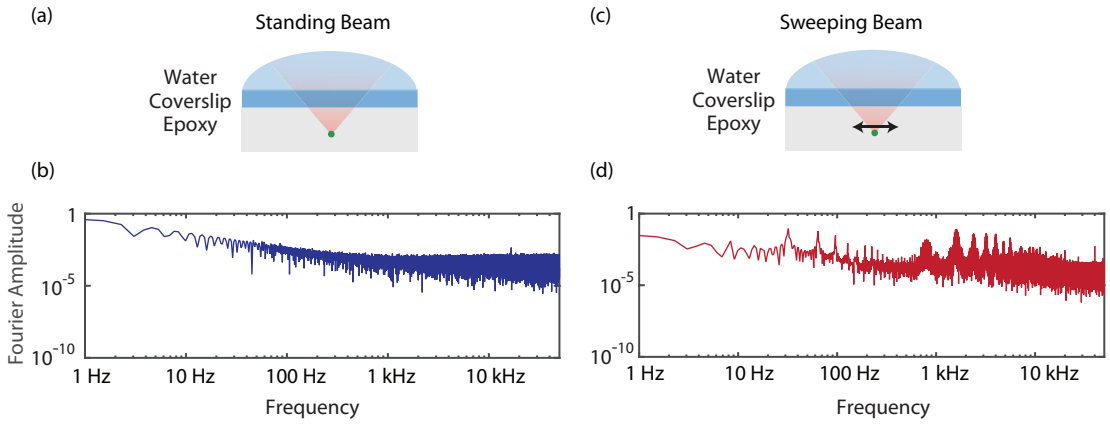

Figure 29: Noise analysis: standing beam vs. sweeping beam optimizations.

The fluorescence signal originating from a 4 μm fluorescent bead under two-photon excitation was measured at high sampling rate with the beam stationery on the bead as shown (a) or the beam performing a 2-dimensional scan across the bead as shown in (c). The Fourier amplitude spectrum corresponding to (a) and (c) are shown in (b) and (d) (note the log scale in both axes). For the dwelling beam approach, the noise components are mostly in the lower frequency (1-100 Hz range). For the scanning beam approach, noise is present even at higher frequencies. The additional fluctuation terms are related to the scanning at line-rate of 1.6 kHz and a full sweep rate of 32 Hz.

In subsequent experiments, the detection bandwidth was set to ~ 30 Hz, which significantly improves the signal-to-noise ratio (SNR) of the signal compared to the bandwidth used for image acquisition (1 MHz). The dwelling beam approach was used to samples that were not likely to sustain photobleaching or photodamage.

On a practical note, since repeated image acquisition and analysis is not required, the microscope software itself does not need to be modified and the wavefront correction system interacts with the microscope only through the signal from one of the photomultiplier tube detectors (PMTs).

2.5.3.4 *Implementing custom code to perform wavefront modulation*

The wavefront optimization system runs on custom code implemented in MATLAB. The LCSLM is addressed as an external display connected to the optimization computer. Reliable display and timing were achieved using the Psychophysics Toolbox extensions [48-50] for MATLAB which provides a MATLAB interface for OpenGL (open graphics library). The basis functions used for optimization were pre-computed using custom code and are loaded when the optimization code is running. During the optimization process, the scaled functions for a single optimization cycle are loaded into memory. For 100x100 grid, each function utilizes 100 kB of memory. The pre-loaded wavefronts can be rapidly transferred to the graphics display buffer to achieve fast update speeds.

2.5.3.5 *Speeding up optimization*

As shown in figure 28, the presented algorithm operates by adding more terms to the previous cycle's correction and hence requires the summing and scaling of trial wavefronts. The maximum sampling resolution permitted by the LCLSM is equal to the number of pixels along its shorter dimension and is 1080. Performing computation on a 1080x1080 grid is computationally expensive. For example, performing a 100 scaling and phase-wrapping operations at the full LCSLM pixel-resolution with 16-bit integer precision takes 1.58 seconds while the same computation can be performed in 0.011 seconds at 100x100 sampling (Computed on an Intel Core 2 Duo E4600 processor on MATLAB). At 100x100 sampling, the computation times become insignificant. Numerical simulations were performed to determine the effects of sampling on the representation error as shown in figure 30.

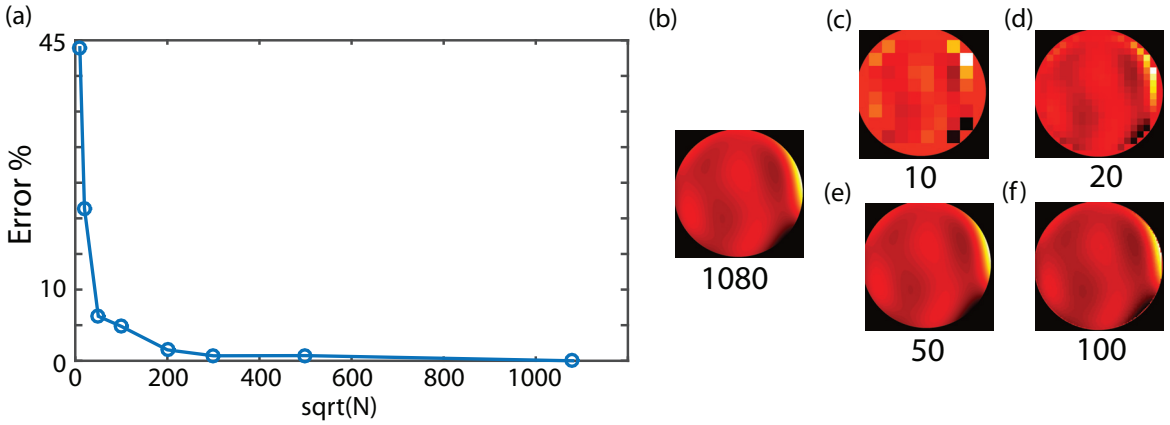

Figure 30: Sampling and wavefront estimation error (Numerical Simulation).

The effect of sampling the wavefront with various numbers of pixels in the range 10^2-1080^2 was studied through numerical simulations. The maximum achievable sampling is a square grid of 1080x1080 pixels as shown in (b). The same wavefront was generated with lower sampling, with some of them being shown in (c)-(f). The root-mean-square error associated with sampling was computed as a function of the number of pixels and is shown in (a). Sampling with 100x100 pixels yields an RMS error ~5% compared to the maximum sampling of 1080x1080.

A reference wavefront was generated by summing the first 20 Zernike function (ignoring the normalization constant) on a $\sqrt{N} \times \sqrt{N}$) square grid with $\sqrt{N} = 1080$. Test wavefronts were also generated using the same Zernike coefficients with $\sqrt{N}$ ranging from 10 to 1080. Error between the reference wavefront and the test wavefront was computed by up-sampling the test wavefront to a grid of 1080x1080 and computing the difference. Figure 30(b) shows the reference wavefront and (c)-(f) show a few of the test wavefronts. The error was computed as the RMS wavefront value of the difference as a percentage of the RMS wavefront value of the reference wavefront so that the error was zero for $\sqrt{N} = 1080$. As shown in figure 30(a), the error is seen to decrease non-linearly with the number of samples N. $\sqrt{N} = 100$ was chosen as the standard value for further optimization, noting that doing so only yields an error ~5% compared to the $\sqrt{N} = 1080$ sampling. If higer sampling is desired in the future, this could be achieved using a newer processor and a hardware control system that provides better real-time performance such as LabView (National Instruments).

The data acquisition is performed asynchronously in order to speed up the optimization process. The data acquisition function runs in the background in a continuous fashion at approximately $30\,ms$ intervals. After a wavefront is addressed, the system is programmed to pause for a time period greater than $30\,ms$ before recording the data point so that the recorded data point corresponds to the last addressed wavefront.

2.5.3.6 *Lowering intensity at LCSLM through hardware up-sampling*

While performing computations at this low sampling resolves timing challenges, this introduces another challenge. A 100 pixel region on the LCSLM represents a length of approximately 0.8 mm. During microscope operation, it can be expected that an average power in excess of 250 mW will be incident on the modulator. The average intensity on the modulator will then be in the order of kW/cm^2, far exceeding the recommended average intensity limit of $2W/cm^2$. In addition, laterally and axially aligning a small beam can be challenging. This can be resolved if the computations could still be performed on a 100x100 grid, but all the 1080 pixels were utilized to represent them. Assuming the LCSLM is lightly underfilled by the excitation beam, in this case the average energy fluence will be smaller than the device damage threshold.

One challenge here is that up-sampling a wavefront from a 100x100 grid to a 1080x1080 grid still requires computational resources and defeats the purpose of performing computations on a low-resolution grid. This issue was resolved by utilizing the interpolation capabilities of the graphics hardware on the optimization computer to up-sample the functions. Figure 31(a) shows a wavefront that has been computed on a 100x100 grid with 255 distinct levels and the same function that has been read from the front buffer of the graphical system which has been up sampled through interpolation to a 1080x1080 grid. Figure 31(b) shows the timing information for 100 wavefronts that have been computed at 100x100 resolution but are upsampled to 1080x1080 as they are being

displayed. The average time between frames is approximately 18 ms, corresponding to a update rate of 56 Hz. The maximum refresh rate of the LCSLM is 60 Hz. Hence the up-sampling step does not pose a challenge in terms of timing. In realistic scenarios, the device updated at approximately 10 Hz. In this case the, average time between frames was $10ms$, corresponding to a 10Hz refresh rate. The timing jitter that is present in figure 31(b) is not present in figure 31(c), indicating that the the measurements and wavefront updates can be reliably synchronized.

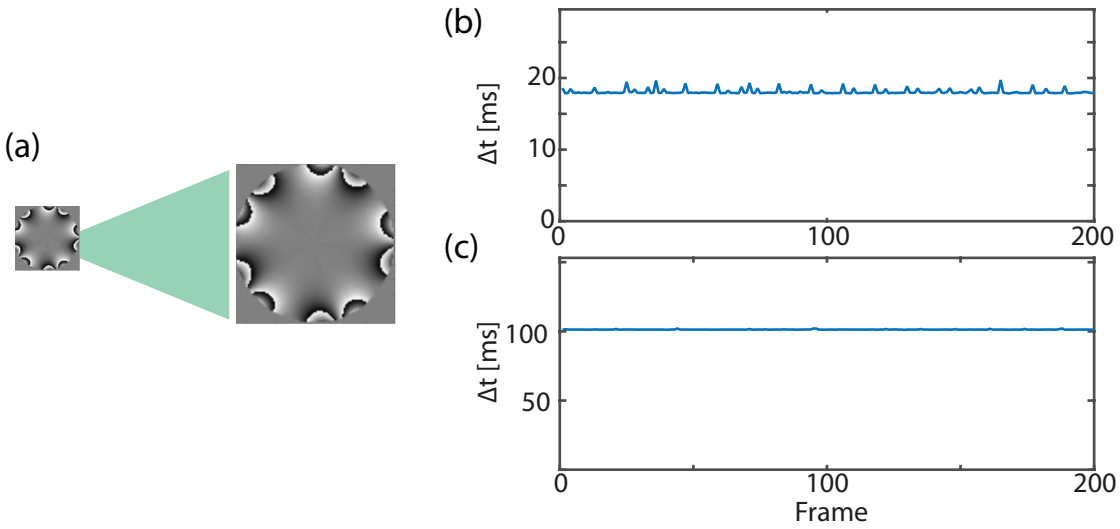

Figure 31: Hardware up-sampling and timing jitter measurements.

(a) Computations are performed on a 100x100 grid and up-sampled using graphics hardware. The left image shows the original wavefront and the right image shows data retrieved from the graphics buffer showing the wavefront after being up-sampled through interpolation. (b) Shows the timing in the 'addressing' loop of the wavefront correction system including the time taken to perform up-sampling and record the fluorescence signal, when the system is operated at a target sample-rate of 60 Hz. (c) Shows the same data when the system is operated at a target sample-rate of 10 Hz. When operating at 10 Hz, the system shows no significant timing jitter.

2.5.4 Demonstration of wavefront optimization

The previous section established the reasoning behind the design of the wavefront correction algorithm and presented technical details of its operation. This section provides experimental demonstrations of its use in various samples.

2.5.4.1 *Demonstrating wavefront correction by direct imaging of the beam*

It was argued earlier that, using a point source, it would be possible to optimize beam focusing using the magnitude of the feedback signal. Figure 32 shows an experiment that makes use of the same concept. Instead of relying on fluorescence, the experiment directly images the beam focus onto a camera. The peak signal on the camera provides a feedback signal provided the pixel size is appreciably smaller than the beam size, which is true for highly aberrated beams.

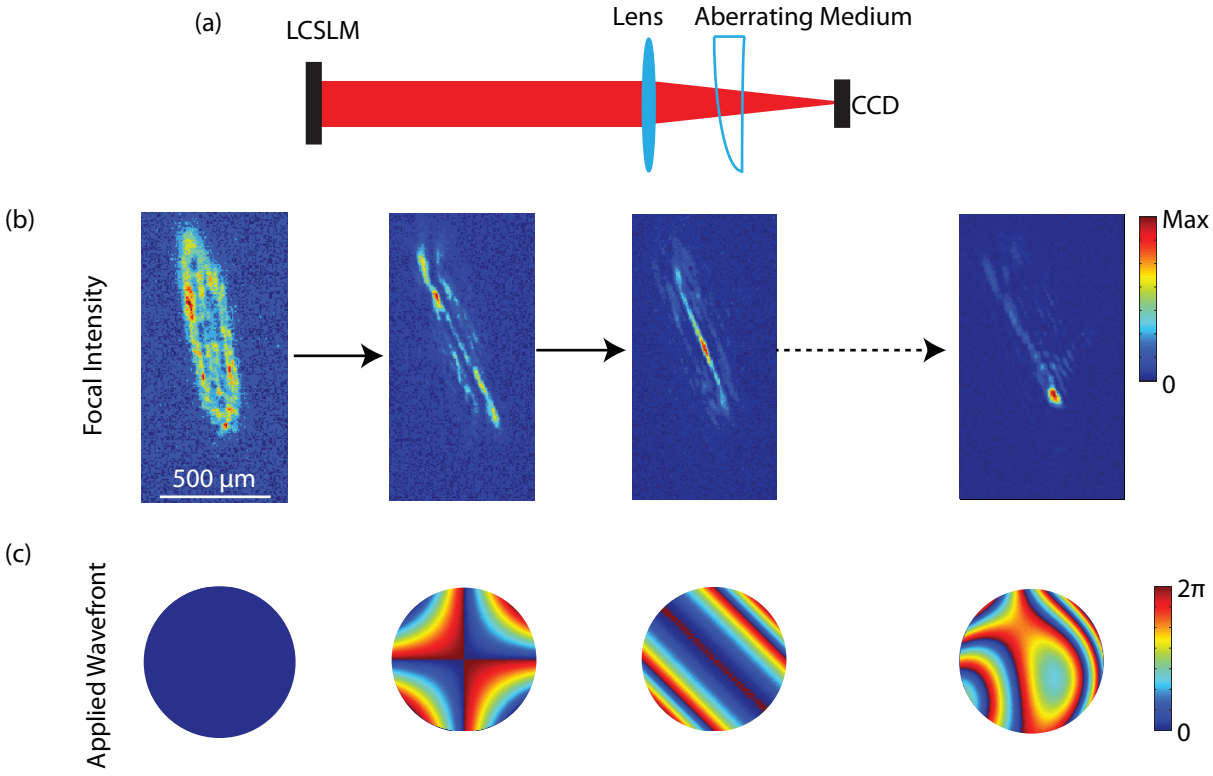

Figure 32: Wavefront correction based on direct beam imaging.

(a) Setup: A beam is reflected off the LCSLM and passes through a lens (f=300 mm). A CCD is placed at the focus. An aberrating medium is introduced to after the lens (for this case, the medium was a cylindrical lens). The wavefront correction system uses the peak signal from the CCD as feedback. (a) Focal intensity evolution as the corrections are performed. Each iteration of the algorithm makes the focus tighter (not all steps are shown). The rightmost image is the focal intensity after correction with Zernike modes 3 through 10. The corresponding applied wavefronts are shown in (c). λ =750 nm.

Performing optimization on an aberrated beam shows that each step of the algorithm yields a tighter beam focus. After correcting with Zernike modes 3-10, the beam is significantly narrower at the focus and the peak intensity of the beam increased by a factor of 6.4. The next section will demonstrate wavefront correction using two-photon excitation when it is not possible to directly sample the beam either with a camera or by imaging a point-like source.

2.5.4.2 *Data collection and analysis methods*

For 2PEF experiments, all data were collected and analyzed using the following methods. The experimental setup was as described in figure 22. During the optimization process, the detection bandwidth was set to ~30 Hz, and the wavefront correction system sampled the signal at approximately 10 Hz. The excitation light source was Ti:Sapphire laser with a pulse repetition rate of 80 MHz and a pulse-width ~100fs (Mai Tai HP DeepSee, Spectra Physics). After the wavefront correction was recovered, the detection bandwidth was set to 1 MHz, and an image stack was acquired of the sample with a flat wavefront (a grid of all zeros) applied to the LCSLM, so that the planes above and below the optimization plane are captured. This is the reference image stack. Then a second image stack was acquired with the correction wavefront applied to the LCSLM. This is the optimized image stack. The two image stacks were compared by either comparing the plane of maximum signal or taking the maximum intensity projection to the xy, xz or yz planes. The signal enhancement was computed using the relation $SE = 100 \times (S_{on} - S_{off}) / S_{off}$, where S_{on} and S_{off} refer to the 2PEF intensity measured with and without the correction applied respectively.

2.5.4.3 *Demonstration of beam constraint*

One of the characteristics expected in the method developed here is that wavefront correction would utilize a discrete object to constrain beam translation during the optimization process. Experimental confirmation of this is shown in figure 33. Figure 33 shows optimization performed for both an in-focus and an out-of-focus object

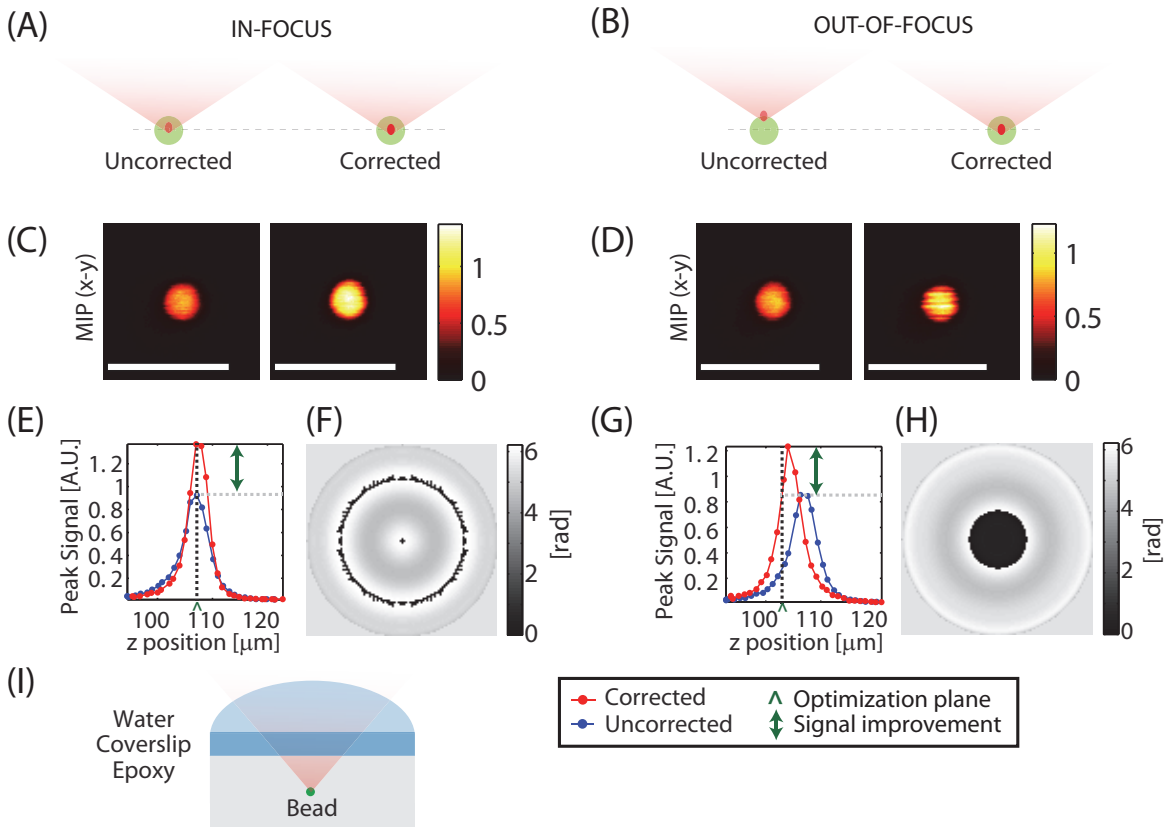

Figure 33:Experimental verification of beam constraint.

Aberration correction performed on a 4 micron diameter bead embedded in a scattering epoxy phantom at a depth of ~100 µm with the bead initially in-focus (left panel) and out-of-focus (right panel). Axial stacks were acquired with and without the correction applied. Optimization was achieved for both the in-focus and out-of-focus bead. In both cases, the optimized focus was formed near the center of the bead. (A,B) Schematics showing the optimization process. (C,D) Max intensity projections of the axial stack to the x-y plane (MIP-xy). (E,G) Peak signal measured at each plane with and without the correction applied as a function of depth. '^' marks the approximate location of the focus prior to optimization. (F,H) Final correction applied to the LCSLM. (I) Schematic of the sample. Scale bars=10 µm. λ= 755 nm. Configuration: Sweeping Beam.

. The sample was a scattering epoxy resin phantom with embedded 4 µm fluorescent beads, imaged through a glass coverslip as shown in (I). Aberrations are thus expected due to scattering

and refractive index differences between water used for immersion, glass and the epoxy material (refractive index ≈ 1.55) [51-53]. Zernike functions were chosen for optimization.

Optimizations were performed for the same bead, but starting from either a point at the approximate center of the bead (A) or slightly above the bead (B). In both cases, axial image stacks were acquired to monitor for axial shifts as well as signal improvement. Maximum intensity projections to the x-y plane (MIP-xy) with and without the correction applied are shown in (C) and (D) for the in-focus and out-of-focus case respectively. As shown in the axial peak-signal plots (E,G), when optimization was started on an object that was not on the same axial plane as the focus, wavefront optimization both adjusted the depth of the focal point to coincide with the center of the bead, and optimized and improved peak signal similarly to the case where optimization was started at the correct axial position. The differences seen in the final corrections (F) and (H) can be accounted for by the fact that in the out-of-focus case, the wavefront adds an axial translation in addition to performing correction. This result shows that optimization can be achieved without beam-constraints so long as a discrete object is present. In all subsequent experiments, the reference object used for optimization was brought into focus before starting the optimization process.

2.5.4.4 *Experimental comparison of Zernike and Hadamard representations*

A second advantage of the method developed here is in its ability to vary basis functions as the system merely optimizes the fluorescence signal, and does not rely on any assumptions about the basis. To test whether our signal-based scheme can be utilized to correct for the effects of heavy scattering, the coverslip in the above experiment was replaced with a piece of scattering tape as shown Figure 34(J). As can be seen in (A), in this case, the heavy scattering makes the bead

difficult to resolve. In this case, instead of using the Zernike basis described earlier, Hadamard functions were used, because the wavefront correction associated with scattering is expected to be discontinuous. Figure 34 thus compares corrections obtained with Zernike and Hadamard functions. In both cases, both a fast optimization (16 functions) and a slower optimization (60 functions) were performed for comparison.

For the fast correction, Zernike function optimization took ~24 seconds, but shows no significant improvement in the image (B). However, Hadamard function optimization, which took 22 seconds, yielded a SE≈230% (C). For a slower correction, optimizing with 60 Zernike functions yielded noticeable enhancement (SE≈50%) as seen in (D), which took 73 seconds while a 70 second Hadamard function optimization yielded a superior enhancement (SE≈357%) as shown in (E). When comparing the corrections (F-I), it can be seen that Hadamard functions are able to capture the randomness of the wavefront better than the Zernike functions. The Hadamard optimization was performed using low order functions represented by only 256 distinct segments on the LCSLM. This is consistent with other studies which show that measurable enhancement can be achieved even when using a small number of segments [31, 54]. While using higher order Hadamard functions is likely to yield better results, optimizing over a larger number of functions will increase computation time.

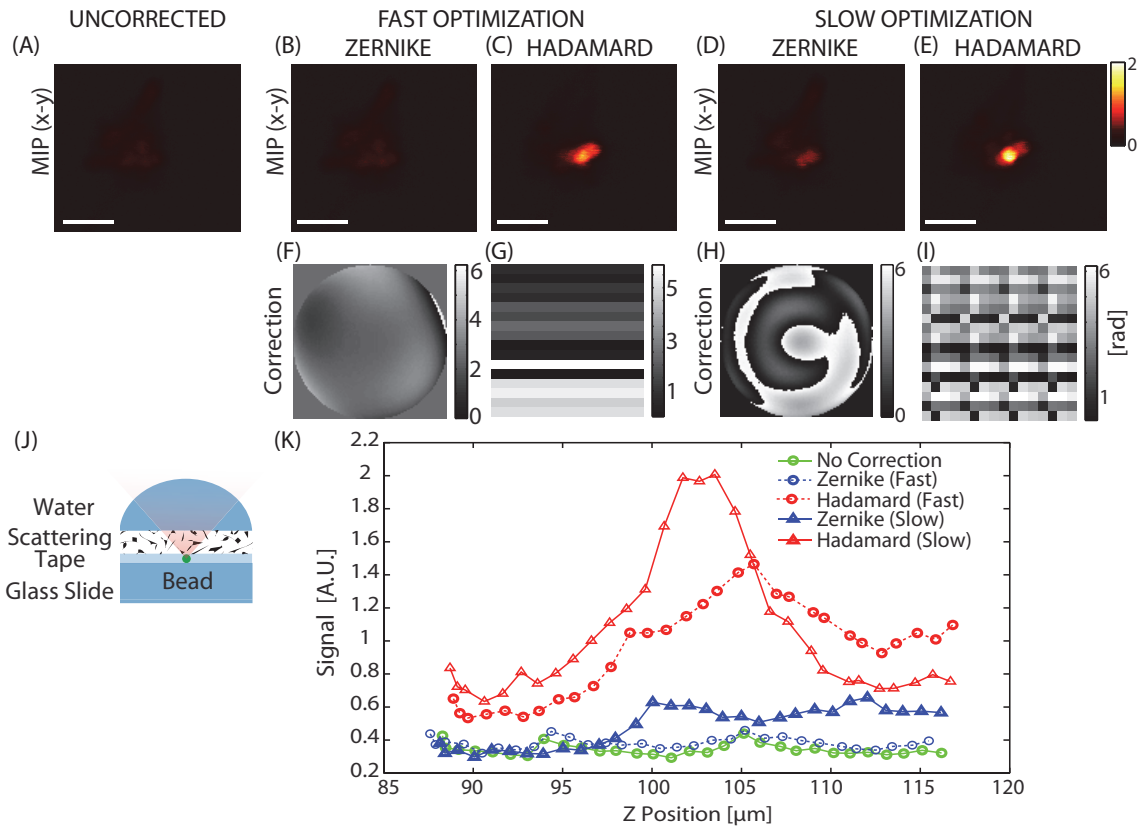

Figure 34: Comparing bases for scattering corrections.

Comparing optimization performed with Zernike vs. Hadamard functions on a scattered excitation beam. Short optimization: Correcting function set Z16 (Zernike) and H256-16 (Hadamard). Long Optimization: Correcting function set Z60 (Zernike) and H256-60 (Hadamard). (A-E) are maximum intensity projections to the x-y plane (MIP-xy). (A) Uncorrected. (B) After fast optimization using Zernike and (C) Hadamard functions. (D) After slow optimization with Zernike and (E) Hadamard functions. (F-I) are the corrections corresponding to (B-E) respectively. (J) shows the sample setup and (K) shows the axial peak signal variation with depth before and after correction. λ=850 nm. Configuration: Standing Beam. Scale bars=10 µm.

2.5.4.5 *Demonstration of sample specific optimizations*

One advantage of using a modal approach is that specific types of wavefront error can be targeted by choosing specific optimization functions. Figure 35 shows three cases where optimization functions have been chosen based on the sample. (A) shows an agar and glass composite sample that mimics a typical window used for in-vivo brain imaging experiments. (B) shows a case where high refractive index mismatch is present while (C) shows corrections achieved when imaging through scattering chicken tissue. Sets of Zernike functions were used for the first two samples, while Hadamard functions were used for the final sample (function sets Z16, ZR and H64

respectively, as defined in section 2.7). Both the optimization time and the final enhancement vary by sample.

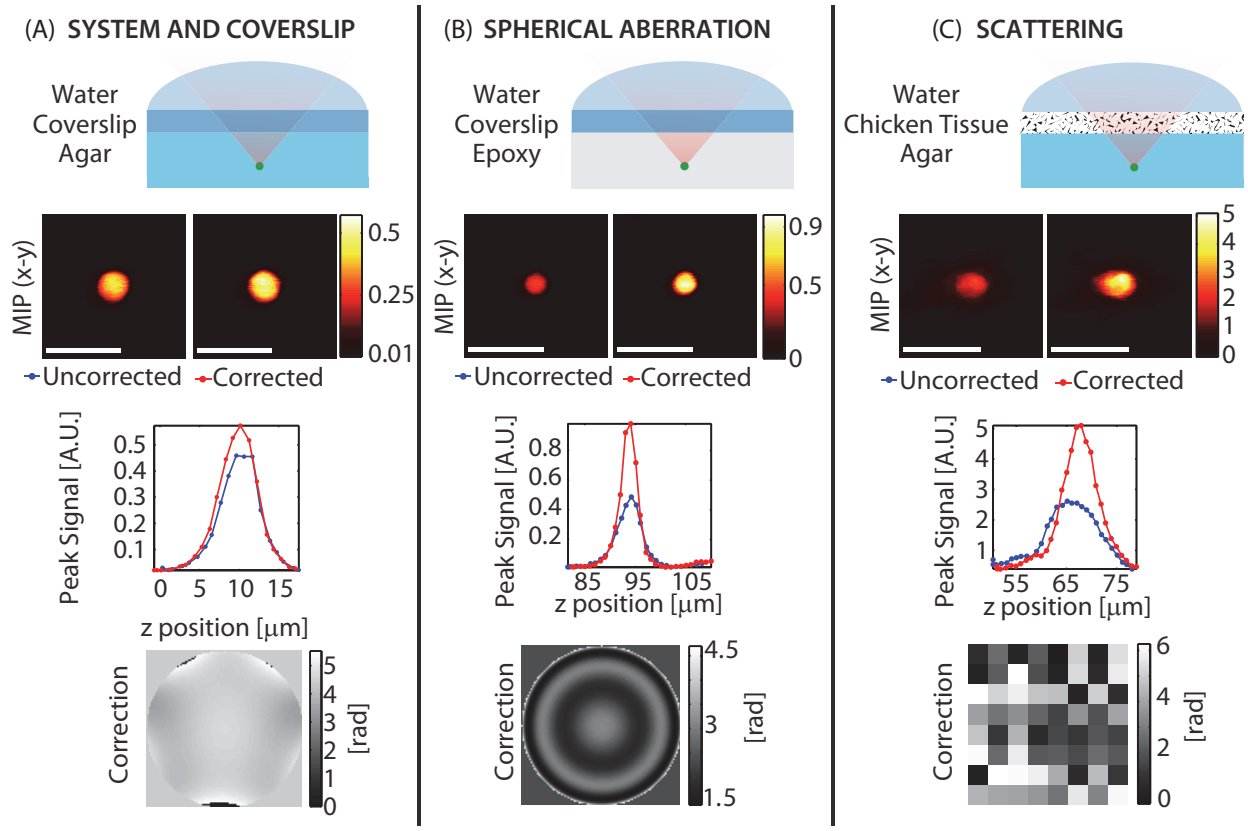

Figure 35: Comparison of optimizations performed on 4 micron diameter beads embedded in various samples:

The functions were picked to match the expected wavefront error. (A) System and coverslip correction. (B) Spherical aberration correction. (C) Scattering induced by chicken tissue. Axial stacks were acquired with and without the correction applied. Each column shows the sample schematic (row 1), maximum intensity projection to the x-y plane (MIP-xy) (row 2), peak signal variation with depth (row 3) and the correction applied to the LCSLM (row 4). λ=755 nm (A, B) and λ=850 nm (C). Configuration: Sweeping Beam (A,B) and Standing Beam (C). Scale bars=10 µm.

The system and coverslip correction yielded an enhancement of SE≈25%. The spherical aberration correction yielded an enhancement of SE≈100%, and the chicken tissue scattering correction yielded an enhancement of SE≈95% as measured using a 4 micron diameter bead. The optimization time in each case was 16.1 seconds, 4.5 seconds and 96 seconds respectively. One important result here is that for samples where spherical aberration is present, significant improvements can be achieved in a short (~5 second) correction using the function set ZR. This is

in agreement with Booth et al**.** [52]**,** who have shown computationally that the wavefront error introduced by refractive index mismatch can be well approximated by several orders of Zernike spherical aberration functions.

2.5.4.6 *Demonstration of In-vivo corrections*

Our correction method does require the presence of some fluorescent contrast that is physically constrained. Ideally, these sources of signal should be well distributed in all areas that are being imaged. In addition, they should provide a stable 2PEF signal. While fluorescent beads can be used for this purpose, introducing beads requires injection, which can disturb the brain, or in-utero surgery [32].

Rather than introduce external sources, we focused on utilizing structures already present in the brain as signal sources. We identified both astrocytes and blood vessels as possible candidates. We first attempted to use blood vessels carrying dextran-conjugated FITC (Fluorescein isothiocyanate), however the movement of red blood cells resulted in high levels of signal fluctuations. Instead, we chose to use astrocytes, which are distributed widely in the cortex and can be easily loaded with a cell-specific red fluorophore (Sulforhodamine, SR101) via simple topical, or even intraperitoneal labeling [2, 55, 56]. Since SR101 is distributed via astrocytic gap junctions, it can spread to astrocytes > 500 microns deep into the brain within 30-60 minutes of application. The excitation and emission spectrum of SR101 are complementary to GFP, GCaMP or Oregon Green labeling of neurons [57].

2.5.4.7 *Window-only corrections*

As previously shown in Figure 35(A), performing a correction using a bead imaged through a coverslip yielded ~25% improvement in signal, corresponding to correction of system and coverslip aberrations. Since the windows used for in-vivo imaging were made using a single

coverslip, as shown in Figure 36(A), it was expected that performing such a correction would also yield improved signal in-vivo. To test this correction, we introduced 4 µm diameter beads onto the surface of the dura, under the cranial window during its construction. When comparing the axial image stacks with and without correction, the window correction itself shows improved 2PEF signal as seen in (B) and (C).

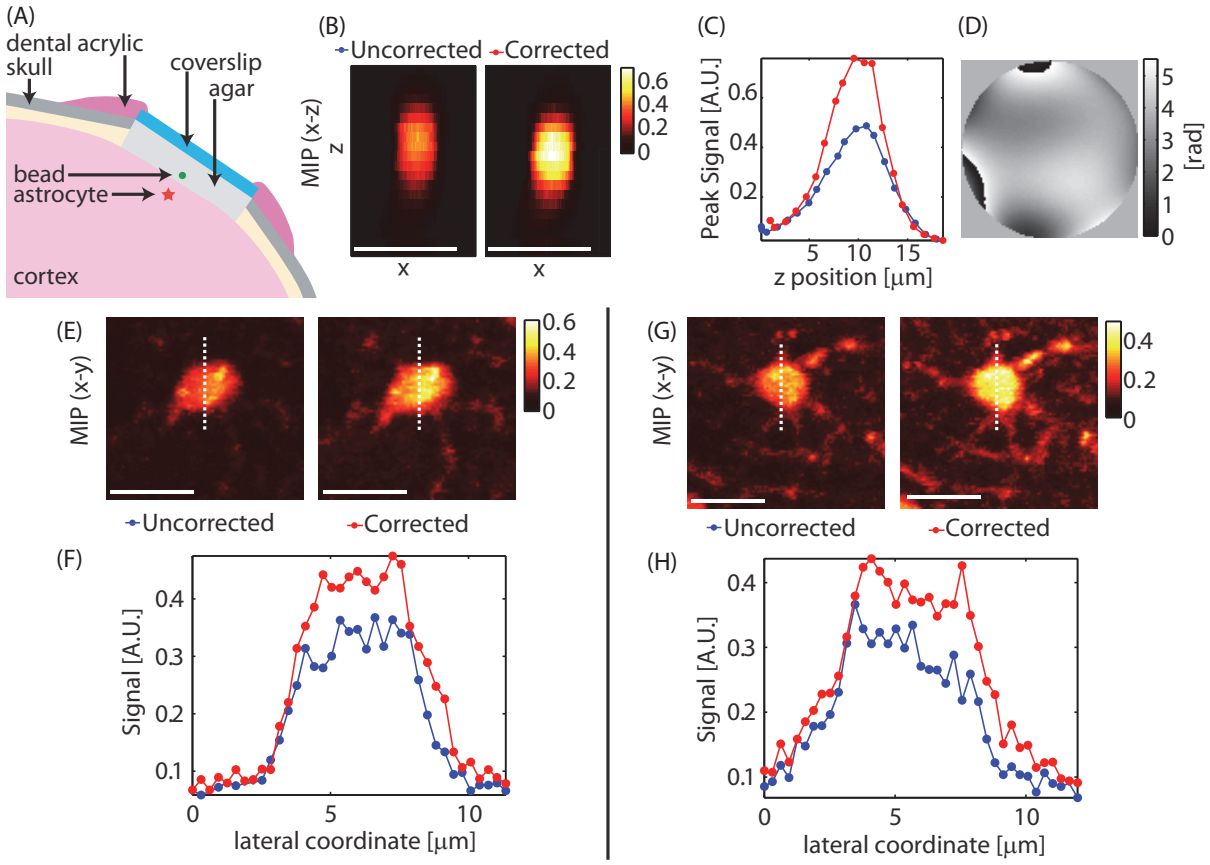

Figure 36: ***Cranial window corrections.***

A correction was performed using a 4 µm diameter bead placed underneath the window on the surface of the dura. The correction obtained using the bead was applied to image astrocytes near the surface of the brain. Axial stacks were acquired with and without the correction applied. (A) Schematic showing the sample setup. (B) Maximum intensity projections to the x-z plane of the bead used for optimization. (C) Peak signal variation with depth for the bead. (D) The final correction applied to the LCSLM. (E,G) Max intensity projections to the x-y plane of astrocytes at a z≈65 µm with and without correction. (F,H) Signal variation along the dashed lines in (E) and (G). Optimization time was 18 seconds. λ=850 nm. Configuration: Sweeping Beam. Scale bars=10 µm.

The correction shown in (D), was achieved in ~18 seconds and yielded enhancement of SE≈56% as measured on the bead (F). When the same correction was applied to two astrocytes at a depth

of z=65 μm in the brain, enhancement values of SE≈22% and SE≈15% were obtained compared to an uncorrected excitation beam as shown in (E-H).

2.5.4.8 *Brain and window corrections using intrinsic guide-stars*

While just correcting for aberrations related to the cranial window is seen to be beneficial, next we set out to perform wavefront corrections to account for both window and brain induced aberrations. Figure 37 shows corrections achieved using astrocytes at various depths *as the reference object*. In each case, an astrocyte was chosen as an intrinsic guide-star and optimization was run to maximize the two-photon signal. In all cases, the optimized focus of the beam remained on the chosen astrocyte despite labeling of local somata and processes. Figures 37(A1-3) demonstrate that a single correction can improve imaging of astrocytes throughout the imaged volume. Figures 37(B-D) show corrections optimized on single astrocytes. The correction shown in (C) on an astrocyte at a depth of z =250 μm was achieved using the function set ZR, which targets spherical aberration and is seen to improve both signal as well as the visibility of processes. (D) shows a worst case scenario. Even though the astrocyte is weakly labeled and is barely discernible over the background, the optimization process still provided some improvement in both signal and image quality.

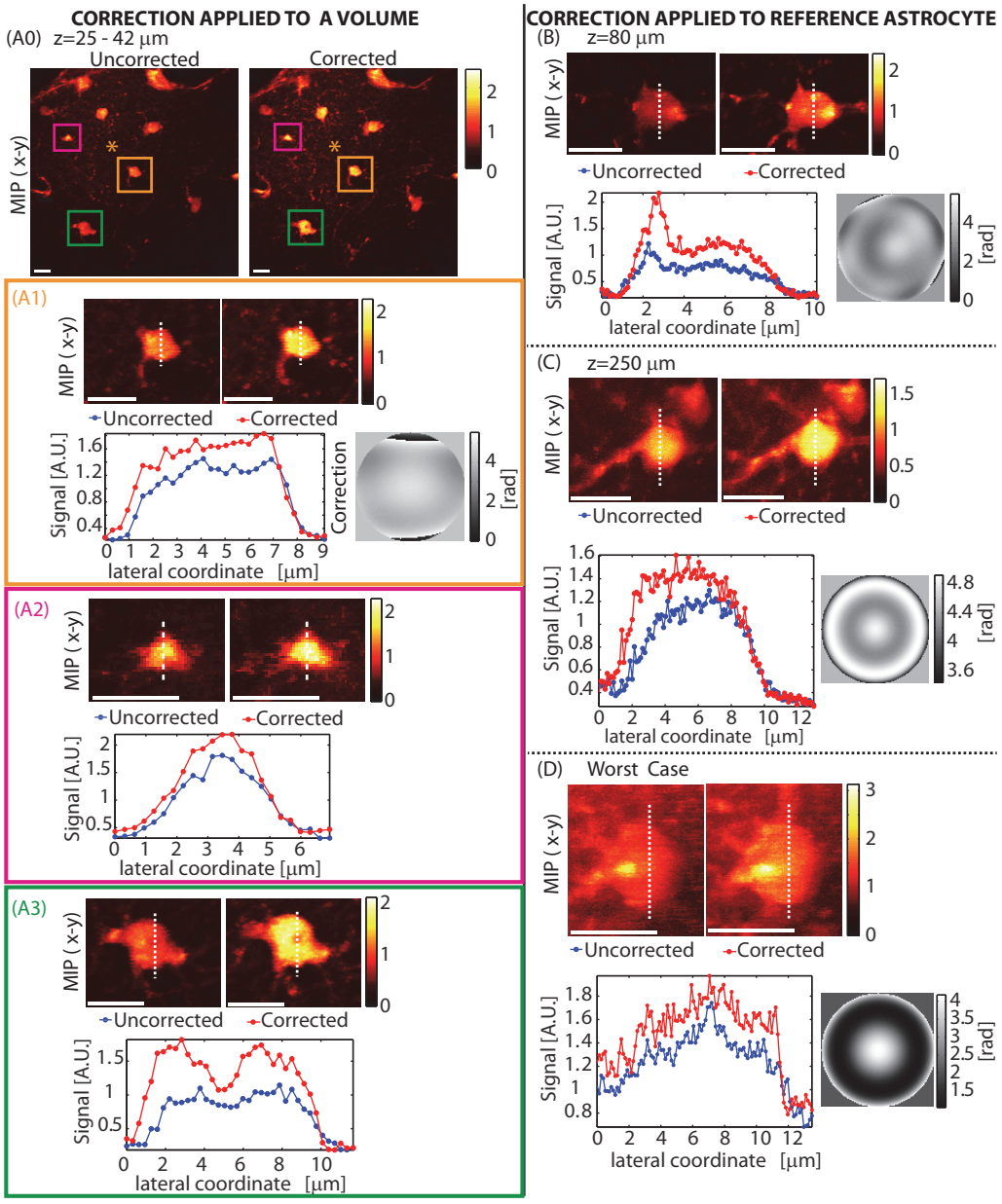

Figure 37: In-vivo corrections using astrocytes at various depths

.(A) A correction was performed using the astrocyte at the center of the field of view (indicated by a '' in A0). An axial stack of this field of view (approximately 120x120x19 µm) was then acquired with and without this correction. (A0) shows the max-intensity projection to the x-y plane (MIP-xy). (A1-A3) shows the MIP–xy and signal cross sections of three astrocytes in the volume located at z≈35 µm, z≈40 µm and z≈25 µm respectively, showing that the correction remains valid across the volume. In (B,C,D), a correction was performed on the same astrocyte as imaged, for a range of astrocytes at different depths. The final LCSLM correction pattern is shown next to the signal variation plot. Function sets used for optimization were: (A) Z16, (B) Z16 followed by ZR, (C) ZR and (D) ZR. Optimization time was (A) 19 seconds, (B) 37 seconds, (C) 6 seconds and (D) 6 seconds. λ=850 nm. Configuration: Sweeping Beam. Scale bars=10 µm.*

2.5.4.9 *Physical extent of in-vivo correction applicability*

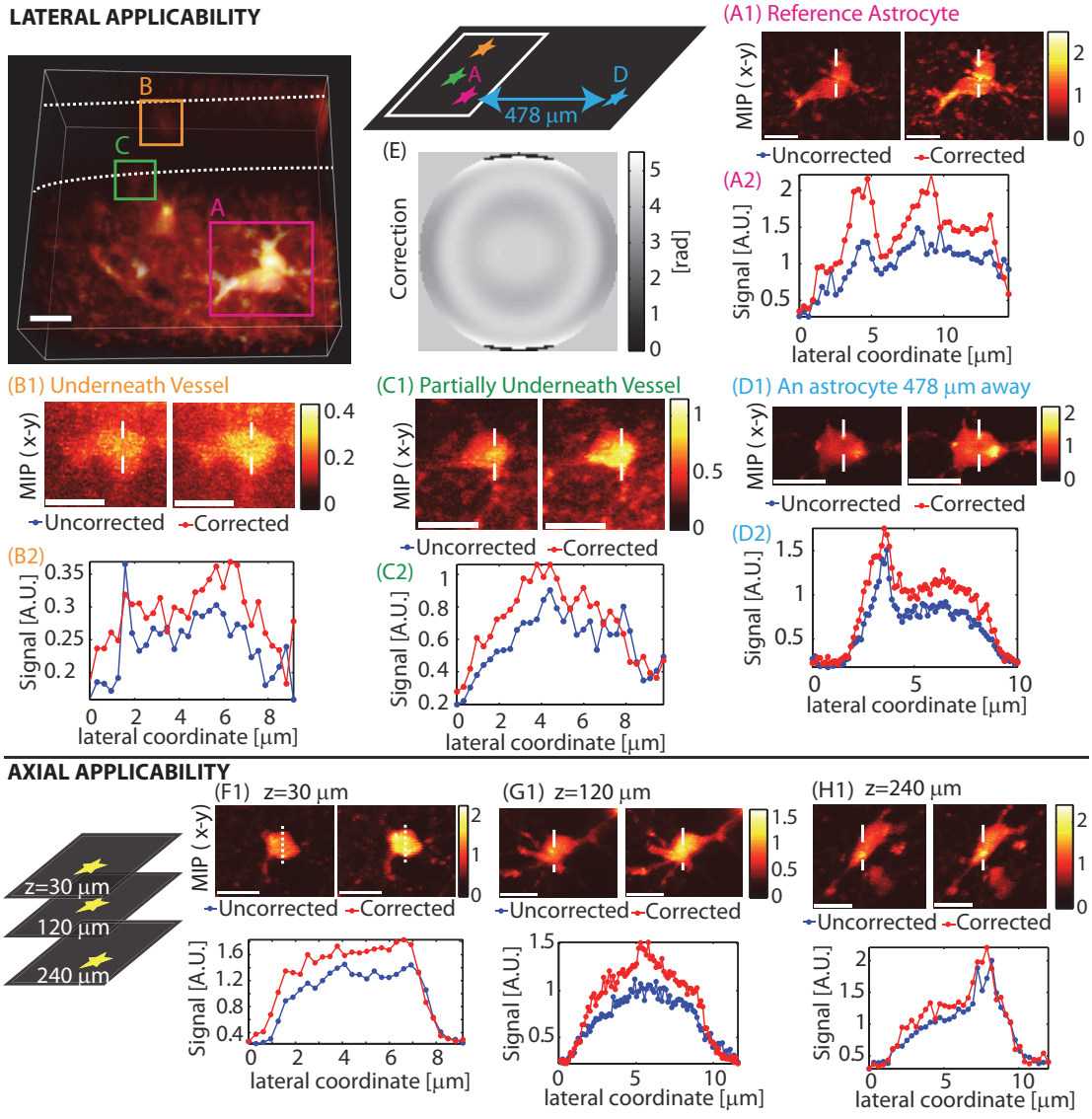

Figure 38: Spatial applicability of a single correction.

Lateral: The image on the top left is a 3-D rendering showing the imaged volume indicating three astrocytes and a blood vessel (outlined in dashed white lines). A correction generated using an astrocyte (A) was applied to the same astrocyte (A), two nearby astrocytes (hidden by a vessel) (B,C), and another astrocyte ~478 µm away laterally (D). The corresponding correction is (E). Optimization time was 22 seconds. Axial: A correction generated at z=30 µm was applied at two other depths (G,H). The corresponding correction is shown in Figure 7(A). λ=850 nm. Configuration: Sweeping Beam. Scale bars=10 µm.

Figure 37(A) demonstrated our ability to improve signal and image quality for objects within the same field of view as the astrocyte used for optimization. However, broader applicability of a

correction optimized at one location over the surrounding volume will reduce the number of repeated corrections that need to be calculated during in-vivo imaging.

The extent of validity of a correction can depend on sample properties as well as the type of correction performed. Figure 37(A) showed how a correction performed on an astrocyte at the center of the field of view remains valid over the whole field of volume. Figure 38(A,B,C) shows a similar situation where a correction made using one astrocyte provides some improvement when applied to two nearby astrocytes hidden by a vessel. When the same correction was applied to another astrocyte 478 μm away as shown in (D), image quality improved and yields SE≈40%. Re-optimizing at the same location yielded a higher enhancement of SE≈60% as previously shown in Figure 37(B). These results show that while local structure can have an effect on corrections, they can remain useful laterally for hundreds of microns.

Figure 38 also shows the axial validity of a correction generated at z≈30 μm. The correction is still found to be useful at z≈120 μm and z≈240 μm, but is seen to become less effective with increasing depth. These in-vivo corrections were achieved in a relatively short amount of time of 5-37 seconds.

2.5.5 Demonstration of Wavefront encoding

So far, the focus has been on correcting aberrations through wavefront modulation. In this case , inadvertent wavefront deviation causes the intensity distribution of the beam at the focus to deviate from diffraction-limited values. It is also possible to intentionally change the intensity distribution of the focal intensity by performing wavefront encoding [58-60]. The most popular application for such systems is in the field of optogenetics. While various forms of microscopy have been used to observe biological phenomena, recent advances in biology have led to the development of light-

sensitive technologies. These technologies now allow experimenters to either activate [61] or inhibit [62] action potential in the living brain using targeted light.

Wavefront encoding then allows for experiments where cells can be activated or inhibited using external light delivery. While these experiments are often conducted using single-photon excitation, there is also interest in using two-photon excitation to perform optogenetic stimulation [63]. The interest in two-photon excitation is that it is a highly localized process that can allow targeting of single cells. Given the interest in performing these experiments, it is useful if the wavefront correction system developed could also perform wavefront encoding, improving the versatility of the system.

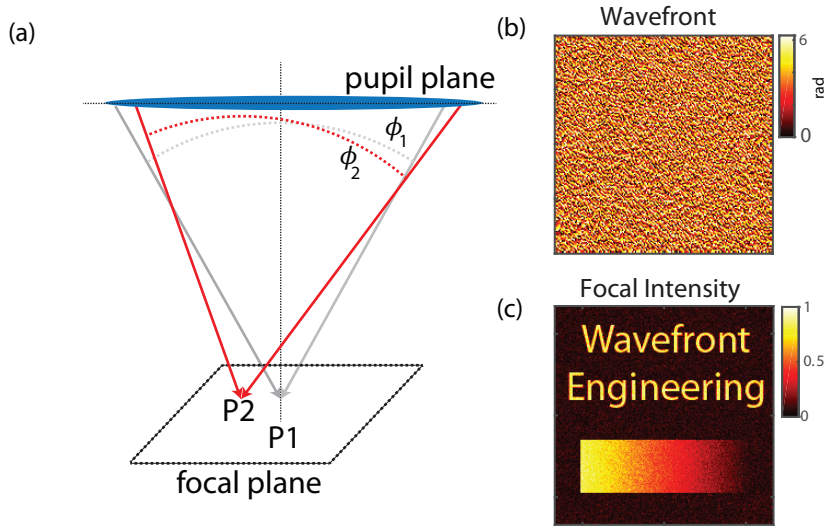

Figure 39: Wavefront Encoding (Numerical Simulation).

(a) Concept of wavefront encoding. A system has a quadratic wavefront ϕ_1 that focuses rays to the focal point P1. Changing the wavefront from ϕ_1 to ϕ_2 causes rays to deviate towards another point P2 (the shown case is for the case where ϕ_2 is obtained by tilting ϕ_1. Hence wavefront modulation can be used to control the focal light intensity. For reliable results interference must be taken into account when performing wavefront encoding. (b) Shows a wavefront computed using the Gerchberg-Saxton algorithm and the resulting focal intensity obtained using Fresnel diffraction. $\lambda = 800\ nm, n = 1.00,$ numerical aperture $NA = 0.6$.

Figure 39 shows the concept of wavefront encoding along with some numerical simulations. An ideal wavefront after a focusing element, which is quadratic, will cause the light to focus at the

focal point. As discussed earlier, this can be understood in-terms of the relation between wavefronts and ray propagation, with the rays propagating orthogonal to the wavefront in an isotropic medium.

A deviation of the wavefront from the ideal case will then cause the rays to point in other directions, which was the cause of unintentional aberrations earlier. However, carefully modulating the wavefront allows fine control of ray directions, and allows focusing of rays towards arbitrary points in space. The ray description however, is not adequate to perform wavefront encoding since near the focus of the rays, diffraction effects will become important. Hence, wavefront encoding is usually performed using a wave model. One such method exploits the Fourier-transform property of thin lenses discussed in Chapter 1 in order to perform phase encoding in what is known as the Gerchberg-Saxton algorithm [64-67]. Figure 39 also shows a wavefront generated using the algorithm and the resulting intensity pattern.

Figure 40 shows experimental validation that the wavefront encoding can be performed on the designed system. The experiment makes use of the same beam path before. A camera and an objective was used to directly image the focal intensity near the focal plane of the microscope objective. A spot pattern was generated on the computer and the Gerchberg-Saxton algorithm was used to generate the corresponding wavefront. The wavefront was then addressed to the LCSLM and the focal intensity was directly measured on the camera. The focal intensity closely matches the requested spot pattern with high contrast, confirming that the wavefront correction system can also double as a wavefront encoding system. In actual experiments, each of the spots will be directed onto an individual cell to either activate or inhibit activity using two-photon excitation.

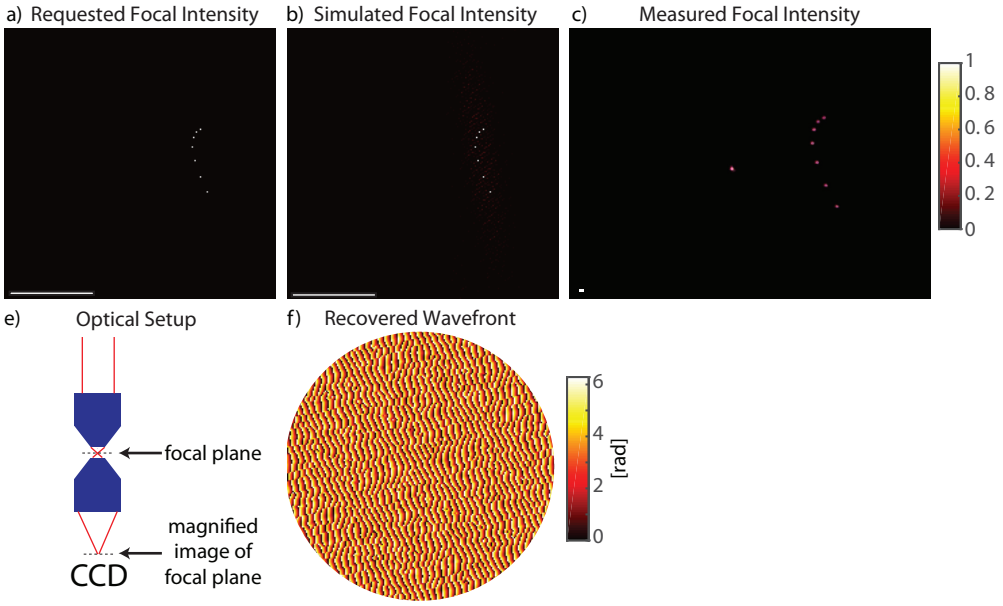

Figure 40: Wavefront encoding (Experiment).

A wavefront (f) that encodes multiple spots in the focal plane was recovered using the Gerchberg-Saxton algorithm. The wavefront was applied to the excitation beam and the focal intensity was measured using the setup shown in (e). The measured focal intensity (c) agrees well with the requested focal intensity (a).

2.6 Discussion

We have demonstrated a simple in-vivo two-photon wavefront correction scheme which generates corrections quickly, without image acquisition or beam constraint. The function type used for correction can be freely varied to match the sample, so the scheme can correct both aberrations as well as scattering. Low order corrections performed in in-vivo mouse brain were found to be valid over hundreds of microns from the point of optimization.

Optimization in the mouse brain was performed based on a the 2PEF originating from a single astrocyte soma for each correction. This approach is likely to succeed with other fluorophores and other cell types provided the labeling density is low enough to allow for discrete, spatially

separated somata. If the labeling of the sample does not meet the above discreteness requirement, astrocytes can be labeled using Sulforhodamine 101 in order to provide a feedback signal for wavefront optimization. The fluorescent emission from Sulforhodamine 101, which is centered on the red region of the spectrum, can be spectrally isolated from the green emission from fluorophores that are commonly used in neurobiology experiments such as green fluorescent protein. Hence, the scheme can potentially be applied to structural and functional imaging of neurons in the mouse brain.

The benefits of our approach make it well suited for in-vivo brain imaging, where adaptive optics promises to improve penetration depth and resolution without requiring greatly increased laser power. In-vivo brain imaging studies focusing on functional recording of neuronal activity require multiple regions to be surveyed within a given experiment. Animals are either anesthetized or, increasingly, awake and head fixed, both of which impose constraints on the duration of imaging experiments. Both of these factors make it inconvenient to utilize wavefront correction schemes that take a long time to optimize.

Another concern when performing adaptive optimization is that the process requires additional sample exposure to the excitation light. In our approach, corrections can be generated at much lower excitation power levels than are typically used for imaging: in most cases the power was lowered during optimization so that the 2PEF signal was 2-10 times lower than for imaging. In addition, since corrections are valid over hundreds of microns, and because optimization is performed without image acquisition, additional light exposure can be localized to small regions, potentially outside of the required field of view. Thus, while our scheme does not provide orders of magnitude improvements in signal, its ability to be recalculated at different sites in less than 60 seconds, yielding up to 100% signal improvements makes it feasible for routine in-vivo use.

In exploring the types of aberrations affecting signal and the effects of each correction, we note that in many cases, just correcting for spherical aberration can produce marked improvements, and can be achieved in around 5 seconds using a simple object at the surface of the brain. Rather than utilize a single spherical aberration correction, we found it useful to correct up to five orders of spherical aberration with the function set ZR. This recognizes that the standard optical window configurations used in in-vivo brain microscopy cause marked aberrations that are well suited to Zernike function correction. For example, we have found that wavefront corrections performed on thicker windows made of two coverslips yielded >100% enhancement when correcting only for the coverslips. Hence spherical aberration should be the first aberration to be corrected for. In cases where an objective with a correction collar is used, adjusting the collar will reduce spherical aberration, before starting the optimization process. In addition to spherical aberration, we performed corrections using 16 low order Zernike functions. We found Hadamard functions to be useful when there were obvious signs of scattering as seen in figure 34(A), where the image of a single bead appears as many beads. In the case of Hadamard functions, we did not choose specific functions. In principal, it is also possible to combine multiple types of bases, such as Hadamard and Zernike to correct for both aberrations and scattering.

In our in-vivo results, we did not explicitly single out the wavefront error coming from the microscope and the window itself, however for the results shown in figures 37 and 38, Zernike functions were used, with minimal improvements being seen with Hadamard functions, suggesting that the dominating effects were aberrations. This is consistent with the fairly long range validity of our corrections within the brain, since the correction for aberrations within the microscope and the cranial window will be valid independent of the location within the sample. However, the smaller variations in the validity of corrections shown in figure 38 do highlight some sample-

location specificity in our corrections suggesting that brain induced wavefront error was also corrected. In terms of limitations, the corrections generated by our optimization scheme depend on its acceptance threshold, which in turn is based on signal fluctuations. Because setting a high acceptance threshold only picks out the corrections that contribute strongly to signal improvement, the optimization scheme might not achieve the best possible correction for a given location. On the positive side, only picking out the most dominant parts of the correction seems to yield corrections that are valid over a large volume.

In the scheme presented here, optimization times of 5-37 seconds are demonstrated to provide useful corrections over large field of view in in-vivo mouse brain. While a 2-photon signal-based optimization scheme that can achieve higher order corrections in around 5 seconds has been demonstrated previously in fixed mouse brain tissue [33], these corrections were valid for only small fields of view, increasing the number of times optimization needed to be performed to image a larger volume. Comparing to image and scanning-beamlet based segmented pupil approaches demonstrated previously for in-vivo mouse brain imaging [34], our faster modal approach achieves similar corrections while also requiring a less complex experimental setup.

In conclusion, we have demonstrated a simple signal-based wavefront correction scheme that uses the 2PEF signal as the feedback. The optimization scheme has modest hardware requirements and can be implemented on a single LCSLM in a configuration compatible with standard patterned photo-activation [58, 68].

2.7 Function Definitions

The correction functions used in our scheme were generated using the definitions presented below and in both cases the minimum and maximum value of each function was mapped to the lowest and the highest phase retardation value of the modulator.

Zernike functions Z_n^m as defined by Thibos et al. [69] were used. The definitions are reproduced below:

$$Z_n^m = \begin{cases} N_n^m R_n^{|m|}(\rho)\cos(m\theta); m \geq 0 \\ -N_n^m R_n^{|m|}(\rho)\sin(m\theta); m \geq 0 \end{cases} \tag{2.17}$$

$$R_n^{|m|}(\rho) = \sum_{s=0}^{(n-|m|)/2} \frac{(-1)^s (n-s)!}{s![0.5(n+|\mathrm{m}|-s]![0.5(\mathrm{n}-|\mathrm{m}|)-s]!} \rho^{n-2s} \tag{2.18}$$

$$k = \frac{n(n+2)+m}{2} \tag{2.19}$$

Here, ρ and θ are the radial and angular coordinates. Each Zernike function Z_n^m is described by an order n and an azimuthal frequency m. The order n takes integer values with 0 being the minimum. For a given order n, the only allowed values of m vary from –n to n in steps of 2. Since each function is described by two indices n and m, the index k used to describe the functions using a single index. We set the normalization constant N=1 for all functions in order to avoid phase-wrapping the initial set of functions used for optimization.

The n-th order Hadamard matrix is defined by the relation [70]:

$$H_n H_n^T = nI_n \tag{2.20}$$

where all the elements of H are either +1 or -1.

Relevant orders of Hadamard matrices can be generated using:

$$H_{2n} = \begin{bmatrix} H_n & H_n \\ H_n & -H_n \end{bmatrix} \tag{2.21}$$

To generate the Hadamard correction functions with n discrete elements, The n-th order Hadamard matrix was generated and each column was rearranged into a 2-dimensional matrix of dimensions $\sqrt{n}$ x $\sqrt{n}$ to represent wavefronts. Functions were indexed so that the k^{th} column of the Hadamard matrix formed the k^{th} correction wavefront.

Since various functions were used, they are identified in the table below. The number of segments used to compute the wavefronts is indicated in the 'Segments' column.

Table 1: ***Functions used for optimization***

Identifier	Basis	Segments	Functions
ZR	Zernike	10,000	k=(12,24,40,60,84)
Z16	Zernike	10,000	k=5 to 20
Z60	Zernike	10,000	k=1 to 60
H64	Hadamard (order=64)	64	k=1-60
H256-60	Hadamard (order=256)	256	k=1 to 60
H256-16	Hadamard (order=256)	256	k=5-20

In the case of Zernike functions, specific sets of functions were chosen based on the sample. For Hadamard functions, no special functions were selected.

Chapter 3: Optimizing laser pulse parameters for fast volumetric imaging

3.1 Introduction

While two-photon microscopy has allowed a great deal to be learnt about the biology of living organisms, it is still limited in some ways. The earlier chapter focused on optimizing the wavefront for two-photon microscopy in order to increase the fluorescence signal and to improve resolution. Another aspect of two-photon microscopy that could be improved is its imaging speed.

A typical point-scanning two-photon microscope achieves a frame rate of ~ 5 Hz, sampling a 500x 500 μm^2 region with approximately 500x500 $pixel^2$. Some speed improvement can be achieved by replacing the conventional galvanometer scanner with a resonant scanning mirror. Even then, the achievable framerate is in the order of 30 Hz. Given this, the volume acquisition rate on point scanning two-photon microscopes are too low to facilitate functional imaging in three dimensions. Several approaches have been developed to increase the volume acquisition rate of two-photon microscopy.

Some approaches have aimed at multiplexing the number of planes acquired through spectral encoding [71] or wavefront encoding of the excitation profile [60], or by generating extended depth of field excitation patterns [72, 73]. While these methods have been proven to be useful, they each work only under special conditions. Some other approaches have focused on improving the scan

speed through the use of non-mechanical scanners [74]. However, these methods have still not delivered fast volume-rates while imaging large volumes. One final approach has been to implement wide-field two-photon and temporal focusing two-photon microscopy, which has delivered 10 volumes per second imaging but at low resolution [75] .

This chapter presents a numerical and experimental study that aims to present a new solution to the problem of fast two-photon imaging. The solution is in the form of scanning light-sheet excitation combined with a detection approach that provides axial sectioning, formally known as Swept Confocally Aligned Planar Excitation Microscopy (SCAPE) [76]. More details on the SCAPE geometry and how it is well suited for fast volumetric imaging will be discussed in section 3.6. The challenge of implementing this approach with two-photon excitation is in managing the many constraints associated with imaging and photodamage. This chapter will conclude with a demonstration of fast volumetric imaging in a non-biological sample.

3.2 Limitation of the point-scanning approach

One question that is worth investigating is if point scanning 2PLSM can be improved upon to provide faster volume rates. While the most obvious approach to improving speed for point-scanning is to scan faster, it is useful to investigate what is ultimately possible by considering the limiting factors.

Figure 41 shows an analysis of the mechanical constraints associated with point-scanning vs. two different light sheet approaches. In order to achieve point-scanning at 20 volumes per second with 200x200x200 $pixel^3$ sampling, the required scan-rate is 160 MHz. Not only does this scan-rate exceed the typical repetition rate of a Ti:Sapphire laser, but the related pixel dwell time of 6.25 ns is comparable to the excited state lifetime of many fluorophores. Because of this, achieving such

fast volume-rates with point-scanning is not likely to succeed. Setting the scan-rate equal to the typical pulse repetition rate of 80 MHz, the maximum volume-rate achievable is 10 Hz. To date, the fastest point-scanning 2PLSM demonstrated has only resulted in ~ 10 Hz volume-rate over a 450 x250x130 μm^3 volume using an ultrasound lens to perform the axial scanning [74].

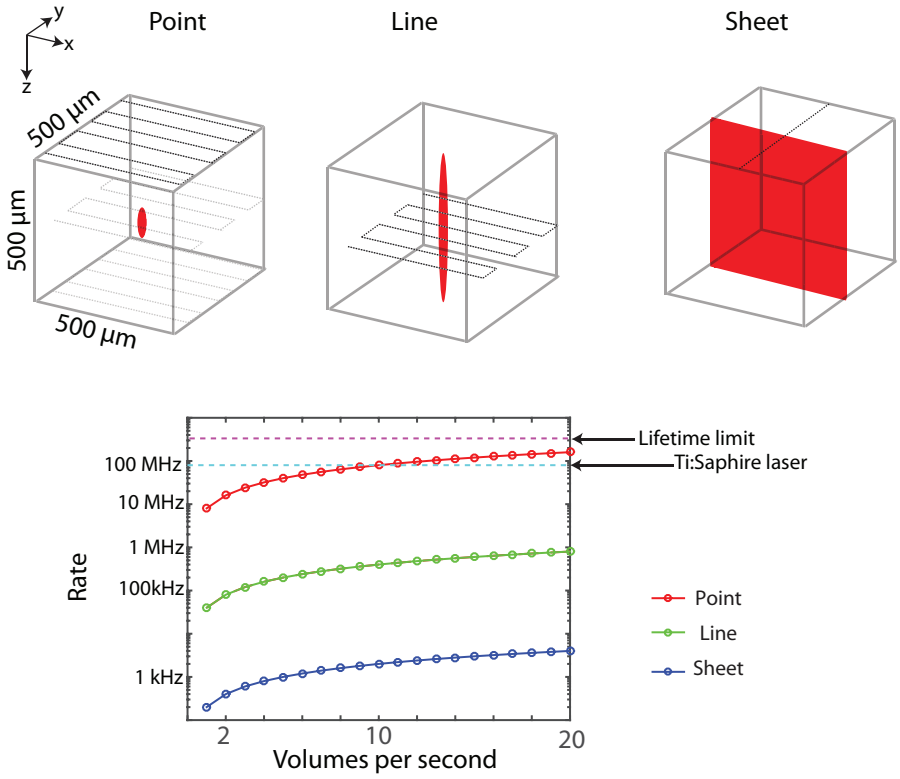

Figure 41: Scan-rates and limitations

Top row: Diagrams of point-scanning line-scanning and sheet scanning for volumetric two-photon imaging. With point-scanning, the maximum imaging speed is limited by the excited state lifetime and the laser repetition rate. With line and sheet scanning, the required scan speeds are much lower than the limits placed by fluorophore lifetime and technological limits.

However, instead of performing point-scanning, if the excitation profile is changed to be an axially extended line or a sheet as shown in figure 41, then the required scan-speeds are much lower than the limits set by the laser repetition rate or the fluorophore lifetime. While these non-standard excitation profiles will resolve the limits introduced by the scan-speed, they require a complete re-

optimization of the microscope design. The rest of this chapter is dedicated to computations and experiments that explore the feasibility of achieving fast volumetric two-photon imaging with axially extended line and sheet excitation.

3.3 Relationship between beam parameters and 2PEF signal

It was established in chapter 1 that the 2PEF signal per molecule is given by:

$$S_{molecule} = \sigma_{2p} I^2 \quad (3.1)$$

Here σ_{2p} is the two-photon action cross-section and I is the intensity. The fluorescence generated per pulse per molecule is then given by the following.

$$S_{molecule} = \int_{t=0}^{\tau_p} \sigma_{2p} I^2 dt \quad (3.2)$$

For simplicity, it is assumed that the temporal profile of the laser pulse is a square wave with repetition rate f_l and duration τ_p. Then the peak value of the intensity I is given by $I_{peak} = \frac{I_0}{f\tau}$, where I_0 is the time-averaged intensity. Then the 2PEF signal per molecule per pulse can be expressed in terms of measurable beam parameters as follows.

$$S_{molecule,pulse} = \frac{\sigma_{2p}}{f^2 \tau_p} I_0^2 \quad (3.3)$$

Fluorescence measurements that will be considered here will be averaged over many pulses. Then it is more useful to consider the signal averaged over some time T. Taking the time averaged value over a time T under the condition $T \gg 1/f_l$ yields.

$$S_T = \frac{\sigma_{2p}}{f \tau_p} I_0^2 T \quad (3.4)$$

Here T is the integration time associated with the detector. The 3-dimensional 2PEF excitation profile can be computed by introducing the intensity of the excitation beam (assuming there is no excitation beam depletion due to two-photon absorption). For the case where the excitation beam is a perfect Gaussian beam, the 3-dimensional intensity distribution can be written as follows.

$$I_{0,beam} = \frac{2P_0}{\pi w^2(z)} \exp[-2 * \frac{(x^2+y^2)}{w^2(z)}] \quad (3.5)$$

The above is the intensity of a Gaussian beam with $w(z)$ being the $1/e^2$ beam width at an axial displacement of z from the waist. In the case of sheet excitation, the more general form of an astigmatic Gaussian beam [77] can be used.

$$I_{0,sheet} = \frac{2P_0}{\pi w_x(z) w_y(z)} \exp\left(-\frac{2x^2}{w_x^2(z)}\right) \exp\left(-\frac{2y^2}{w_y^2(z)}\right) \quad (3.6)$$

The sheet is described by two values $w_x(z)$ and $w_y(z)$ which are the beam radii in the x and the y dimensions. For the case where $w_x = w_y$, the sheet excitation reduces to the commonly used form of a Gaussian beam. It is assumed here that for the sheet, the beam waist in both dimensions occur at the same z-plane after the objective. The 3-dimensional form of the above can be generated using ABCD matrices or Gaussian beam propagation equations, keeping track of each dimension separately. Then the 3-dimensional 2PEF distribution and signal strength can then be obtained by substituting equations 3.5 or 3.6 in 3.4. The 2PEF signal at the focus can be computed by setting $x = y = z = 0$.

$$S_{T,focus} = \frac{\sigma_{2p}}{f\tau A^2} P_0^2 T \quad (3.7)$$

Here A is the beam cross-sectional area defined by the following relation.

$$A = \pi w_{x0} w_{y0} \quad (3.8)$$

Here, w_{x0} and w_{y0} are beam waist radii in the x and y dimensions respectively. Equation 3.7 demonstrates the how the magnitude of the 2PEF signal scales with beam parameters. For example, it can be seen that the 2PEF signal drops off as the square of the cross-sectional area but increases linearly with integration time.

3.4 Constraints associated with two-photon excitation

This section aims to identify the various constraints associated with two-photon excitation.

3.4.1 Signal constraint

The first constraint that is relevant to microscopy is the signal constraint. In order to generate useful data, the fluorescence signal collected from each voxel must have noise levels below some threshold that depends on the application. For structural imaging of a system that is not dynamic, there are not many time constraints. In this case, it is possible to average over many acquisitions to increase the overall signal-to-noise ratio (SNR) even though each image itself might be noisy. In dynamic experiments where the experiment can be repeated, the condition is that the SNR of the averaged data should exceed the fluctuations that are being measured. Finally, the most challenging signals to measure are spontaneous signals that are not controlled by the experimenter, and hence no data averaging is possible. This type of experiment requires high SNR measurements as no averaging is possible. An optical measurement at the very least contains shot noise. But in reality, many other forms of noise associated with the detector and the detection electronics can be present. For this study, the signal levels associated with various excitation methods will be established experimentally.

3.4.2 Lifetime constraint

While energy absorption from the excitation beam is near-instantaneous, the relaxation process takes a finite amount of time. This can be seen by solving the rate equations presented in Chapter 1. For a molecule that is in the excited state at time $t = 0$, the probability of finding the molecule in the excited state at some $t > 0$ follows an exponential decay. For fluorophores that are of interest for microscopy, the characteristic decay time is in the order of 3 ns. Hence two-photon microscopes are designed so that the separation between pulses exceeds the excited state lifetime [78]. For example, the pulse repetition rate in a common Ti:Sapphire laser is 80 MHz, corresponding to a pulse separation of 12.5 ns.

3.4.3 Saturation and photodamage constraints

3.4.3.1 *Saturation*

While equation 3.7 predicts that the magnitude of the time-averaged 2PEF signal scales as the square of the average power P_0, this relationship assumes that the excitation is weak. For strong excitation intensities, the relationship between the 2PEF signal beam parameters deviate from the relationship given in equation 3.7 [19]. The conditions under which the deviation happens, referred to as saturation, can be estimated based on the following arguments. The number of photons absorbed per pulse per molecule at the beam focus was computed by Denk and Webb [17] as

$$n_a \propto \frac{\sigma_{2pa} P_0^2 (NA)^4}{\tau_p f_l^2 (2hc\lambda)^2} \quad (3.9)$$

Here σ_{2pa} is the two-photon absorption cross-section in units of GM and NA is the numerical aperture of the excitation beam. Since we will be modulating the beam cross-section A in later

sections, it is more useful express the above in terms of A. Substituting with the relationships $w_o = \frac{\lambda}{\pi NA}$ and $A = \pi w_0^2$ yields the following:

$$n_{abs,pulse} \propto \frac{(\frac{\sigma_{2pa}}{hc/\lambda})P_0^2}{4\pi^2\tau_p f_l^2 A^2(\frac{hc}{\lambda})} \quad (3.10)$$

where $\frac{hc}{\lambda}$ is the photon energy and A is the beam cross-sectional area. The two-photon absorption cross-section σ_{2pa} is usually given is units of GM and can be converted to standard units using the relation $1GM = 10^{-50} cm^4 s/photon$ [79]. Saturation effects will manifest when n_a becomes comparable to 1 [80]. Computing the energy fluence $\mathbb{F} = \frac{P_0}{f_l A}$ that yields $n \sim 0.1$ for a pulse width of 100 fs for $\sigma_{2pa} = 37\ GM$ (This is comparable to the cross section of both fluorescein [18] as well as GCaMP6f [81]) yields $\mathbb{F} \sim 2.5\ nJ/\mu m^2$. For an NA=1 beam with $f_l = 80\ MHz\ \tau_p = 100\ fs$, this condition is met when $P_0 \sim 40\ mW$. Figure 42 shows an experimental measurement of saturation behavior for point-scanning two-photon microscopy with a tightly focused beam. The relationship between power at the sample and fluorescence deviates from equation 3.7 when the average power at the sample exceeds 50 mW. When operating near saturation, the fluorescence generated will be lower than the value computed using commonly used equations. In addition, in the saturation regime, the excitation profile can deviate from what is expected. This will be discussed later in the context of axially extended line excitation.

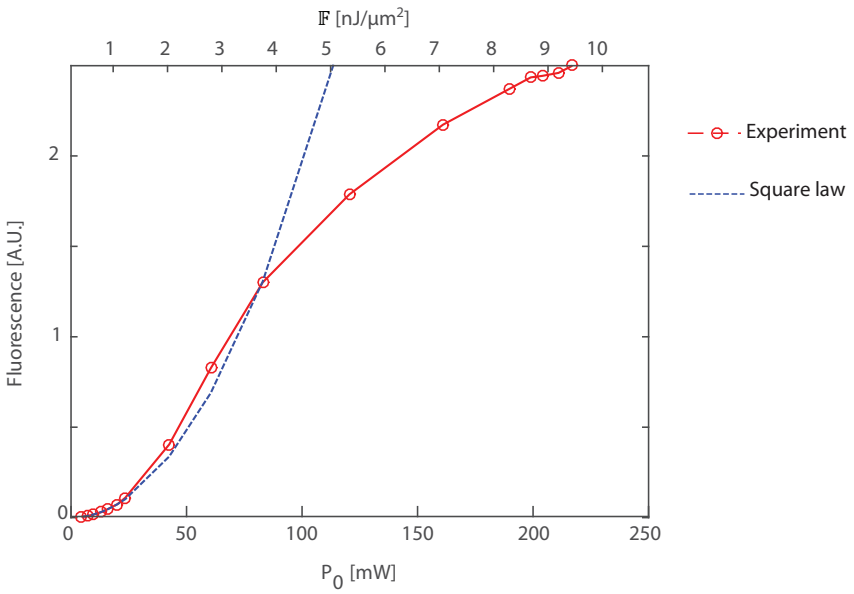

Figure 42: Saturation behavior for point scanning 2-photon microscopy (Experiment).

Fluorescence from fluorescein at a concentration of $1\mu M$ *was measured as a function of average power at sample* P_0*. At low power, the relationship obeys the square law but deviates from it at high power.* $NA \approx 1$, λ *=800 nm,* $f_l = 80\ MHz, \tau_p \sim 100\ fs$.

3.4.3.2 *Cell-damage*

Exposure to the excitation light source can be harmful to cells. Cell damage is usually not visible in microscope images and might have to be factored in the microscope design as well as experimental design. Experiments performed by other researchers suggest that the damage mechanisms at wavelengths used for two-photon microscopy are dominantly due to nonlinear processes. One study found that the photo-damage scales as $\iint I^{2.5}(x,y,z,t)dVdt$, and prescribes a threshold of 6 mW for $NA = 1.2, \lambda = 800\ nm, f_{laser} = 80\ MHz$ and a pixel dwell time of 80 μs [82]. This converts to a fluence limit of 0.5 $nJ/\mu m^2$ for the repetition rate and the dwell time mentioned above. A study done using wide-field two-photon excitation found that an intensity of 115 GW/cm^2 for 30 seconds with f_l~200 kHz and $\tau_p = 170\ fs$ causes photodamage [83]. This corresponds to a fluence limit of 0.2 $nJ/\mu m^2$ for 170 fs pulses.

3.4.3.3 *Ablation*

While the type of damage discussed above would not be obvious during imaging, another type of damage can occur that is obvious – ablation mediated by plasma. If the electric field of the laser pulse becomes comparable to the binding energy of the valence electrons, the laser pulse can trigger a process that generates plasma within the sample. The threshold value for this process is $\sim 10 \frac{nJ}{\mu m^2}$ [84].

3.4.4 Sample heating

Since only a small fraction of the excitation energy gets converted to fluorescence, the rest of the energy is dissipated in the sample itself. It has been observed that two-photon imaging of the mouse brain leads to an increase in brain temperature. Experiments performed at $f_l = 80\ MHz$ and $\tau_p = 120\ fs$ have found that the temperature rise is linear in average power P_0 and is independent of the numerical aperture of the beam, provided the scan area, step-size and the dwell times are the same. Then the steady state brain temperature is given by $1.8°C/100mW$ [85]. Experiments performed at $f_l = 4.1\ MHz$ and $\tau_p = 180\ fs$ using a temporal-focusing two-photon microscopy scheme also found a linear relationship between steady-state temperature and average power [75]. Based on the above, the safe limit for average power at the sample can be estimated to be $\sim 200\ mW$.

Table 2 summarizes all the constraints discussed in this section. Various two-photon excitation profiles can now be considered taking into consideration the restrictions placed by the conditions in Table 2.

Table 2: Constraints

Description		Conditions	Comments/References
Signal constraint	At least enough signal to exceed dark noise on detector		Varies based on fluorophore concentration, system transmission and detector.
Saturation	$\mathbb{F} < 2.5\, nJ/\mu m^2$	$\sigma_{2P} \approx 20\, GM.$ $\tau_p \approx 100\, fs$	Equation 3.10 Figure 43 (Experiment)
Cell death	$\mathbb{F} < 0.2\, nJ/\mu m^2$	$\tau_p \approx 170\, fs$ $T = 30\, seconds$ $f_l \approx 200\, kHz$	
Ablation	$\mathbb{F} \ll 10\, nJ/\mu m^2$		
Brain Heating	$P_0 < 200\, mW$	Independent of numerical aperture. Independent of pulse repetition rate for $f_l = 4\, MHz - 80\, MHz$	[85] [75]

3.5 2PEF Profiles

Various 2PEF profiles can be generated by manipulating the beam at the back-focal-plane of the excitation objective. Figure 43 shows the back focal plane configuration for creating point, axially extended line and axial sheet 2PEF excitation profiles.

The 2PEF profiles were generated using equations 3.4 and 3.6. Figure 43(a) shows the beam configuration at the back focal plane. For a point excitation, the beam is large at the back-focal plane so that the back-aperture of the objective is mostly filled. Column 1 shows the 3-dimensional distribution for an effective NA of 0.6 at $\lambda = 800\, nm$ in water. The lateral and axial FWHM in x,y and z was $0.35\, \mu m$, $0.35\, \mu m$ and $1.1\, \mu m$ respectively (the lateral profile was fitted to a Gaussian while the axial profiles were fitted to a Lorentzian function).

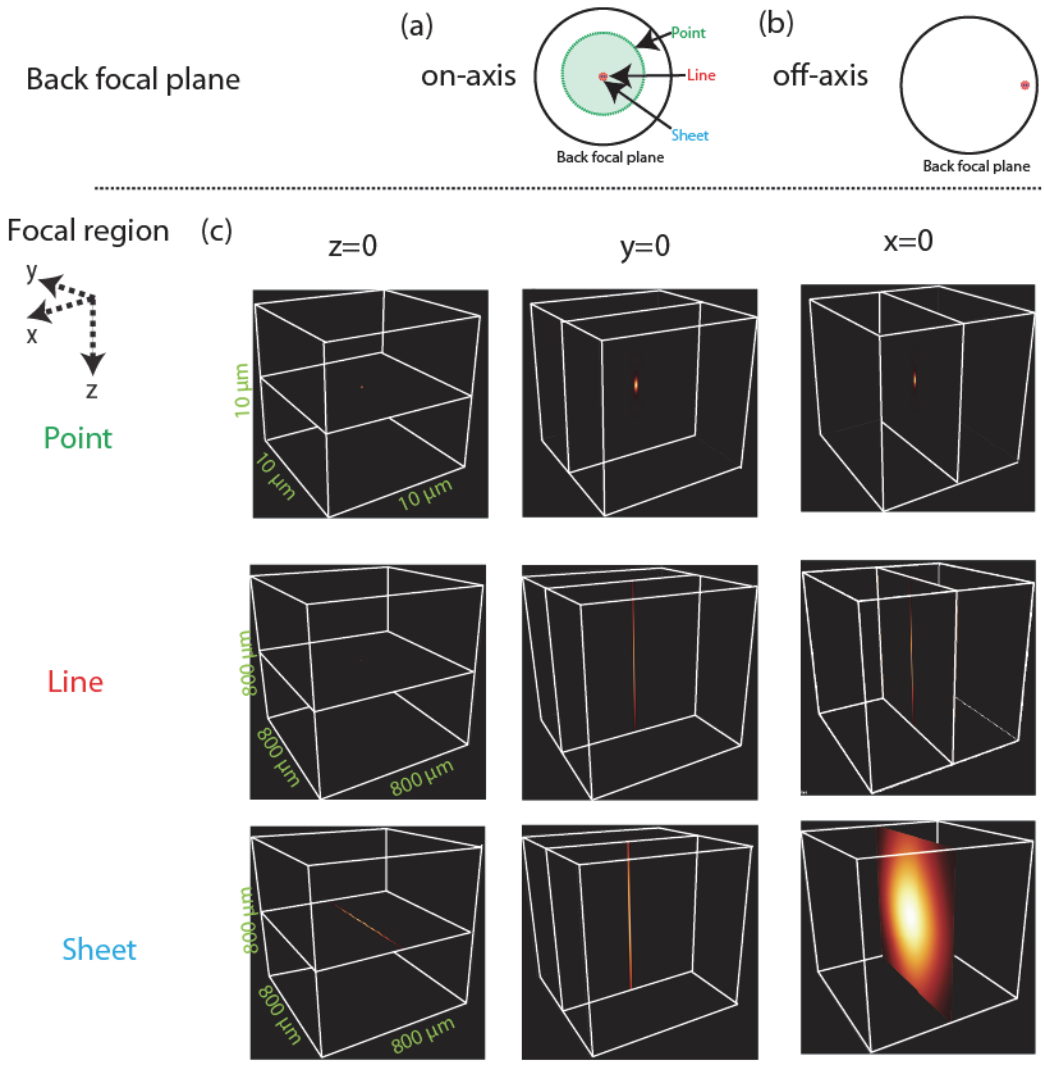

Figure 43: Generating various 2PEF excitation profiles (Numerical Simulation).

Various on-axis excitation profiles can be generated by changing excitation beam profile at the back aperture as shown in (a). A large excitation beam impinging on a high NA objective yields a point excitation pattern as shown in column (1). A small excitation beam at the back focal plane yields an axially extended excitation profile as shown in column (2). An asymmetric beam at the back focal plane yields a sheet profile as shown in column 3- in this case, the beam is focused in one dimension and collimated in the other. Off-axis profiles (not shown) can be generated by decentering the excitation beam at the back focal plane. Profiles generated from equations 3.4-3.6 for $\lambda = 800\ nm$, n=1.33 for an objective with NA=1.

Similarly, an axial line excitation can be generated by lowering the fill-factor of objective as shown in red in figure 43(a). This lowered fill factor increases both the lateral and the axial extent of the beam, with the axial extent expanding much more than the lateral. The resulting two-photon excitation profile for an effective NA of 0.032 is shown in figure 43 column 2. The FWHM in x,y and z were $6.62\ \mu m$, $6.62\ \mu m$ and $487\ \mu m$ respectively. Finally, a sheet excitation profile can be

generated by focusing one of the dimensions that was used to generate the line, as shown in blue in figure 43(a). In this case, the beam at the back focal plane is a line. The resulting excitation profile, when the beam from the line excitation case is focused down by a factor of 75 in one dimension, yields the excitation profile shown in figure 43(c). The FWHM in x,y and z was found to be $6.62\ \mu m$, $497\ \mu m$ and $662\ \mu m$ respectively. When going from a point→line→ sheet, the beam cross-section at the back-focal plane is decreased while the beam cross-section at the waist is increased. As will be disccused in the next section, simply generating on-axis excitation profiles as described in figure 44(a) will not yield optical sectioning and requires creating off-axis excitation profiles. Off-axis excitation profile can be generated by decentering the excitation on the back focal plane of the objective as shown in figure 44(b).

An alternate method to creating an axially extended line excitation is to create an annular ring amplitude pattern at the back focal plane, which results in a Bessel-like beam near the focus [86]. This type of beam provides an extended depth of focus with a small central lobe width but creates side-lobes due to the Bessel-like behavior. The effect of side-lobes is partially mitigated by the two-photon excitation. This approach has been successfully used to create a 2PEF line profile with an axial depth of focus (FWHM) of $100\ \mu m$ or less [72]. Creating a large depth of focus requires results in a higher percentage of energy being carried in the side-lobes which will results in lowering the effective resolution [72]. The rest of this chapter will only explore Gaussian excitation profiles as their properties are well known, and because they simplify both the experimental setup as well as numerical simulation. Bessel-like excitation profiles merit more attention in later numerical and experimental studies.

3.6 Imparting Sectioning

Generating an axially or laterally extended profile significantly increases the excitation volume. However, in this case, a point detector can no longer be used to provide resolution and a camera is needed.

One previous approach utilized a laterally extended excitation profile to increase the excitation region. In this wide-field temporal focusing approach [87], the excitation profile is expanded laterally to form a disc-like excitation region. Axial sectioning is achieved in this case using a temporal-focusing setup, where the pulse experiences dispersion everywhere except near the focus. Each camera image captures a lateral plane and a volume is acquired by scanning the disc along the z-axis. The limitation of this implementation is in how the two-photon signal scales with the area of excitation. For example, using high energy ($\sim 2\ \mu J$) pulses, it has only been possible to create a disc-like two-photon-excitation profile that is $\sim 60 \mu m$ wide [87]. As will be demonstrated in section 3.7.2, significant improvement in excitation efficiency can be achieved by extending the excitation profile axially to form a sheet.

In the case of an axial sheet excitation profile, depth sectioning can be achieved by the use of oblique illumination combined with oblique detection as shown in figure 44(b). Figure 44(c) shows a scanning microscope that provides depth sectioning through the scanning confocally aligned planar excitation (SCAPE) geometry [76], which provides both de-scanning and depth sectioning. This geometry has been utilized previously to achieve fast volumetric imaging and hence it was hypothesized that the same geometry could be utilized to achieve volumetric imaging with two-photon excitation.

The SCAPE imaging geometry forms the excitation beam into an oblique light sheet as shown schematically in figure 44(c). The light sheet is scanned laterally using a galvanometer scanning mirror which is imaged on to the back-focal-plane of the excitation objective using a telescope formed by lenses L4 and L5. Similar to a confocal microscope, the galvanometer mirror also performs de-scanning, and a de-scanned image plane is formed after the 2nd objective OBJ2. The image plane remains stationary even when the sheet is being scanned. The third objective OBJ3, is placed orthogonal to this stationary image of the sheet, and re-images the stationary image plane onto a camera. A volume is captured by performing a single sweep of the sheet while recording the data-stream on the camera. The individual frames can be used to reconstruct a volume image of the sample fluorescence. The SCAPE geometry then allows fast imaging by scanning the sheet using the galvanometer mirror. The same geometry can be utilized to image a volume with line excitation by using two scanning mirrors that scan and descan an axially-extended beam in x and y and creates a linear oblique image in the intermediate image plane. In this case, elements of a linear detector will image different depths in parallel such that a single x-y raster scan will image a volume.

Given that SCAPE microscopy uses the same objective for excitation as well as light collection, and uses a sheet scanning to excite a volume, it is compatible with mouse brain imaging with a water immersion objective. SCAPE microscopy of the mouse brain with single-photon excitation is limited by the depth penetration of the visible wavelength excitation light [88]. Achieving two photon excitation in this geometry could pave the way for fast volumetric imaging with increased depth penetration.

Because SCAPE's excitation profile is oblique, the imaged volume is at an angle to the optical axis and will be represented by the as x, y and z' axes. For line excitation, x and y are scanning

directions. For sheet excitation, the sheet is laterally extended along the y axis and scanned along the x axis.

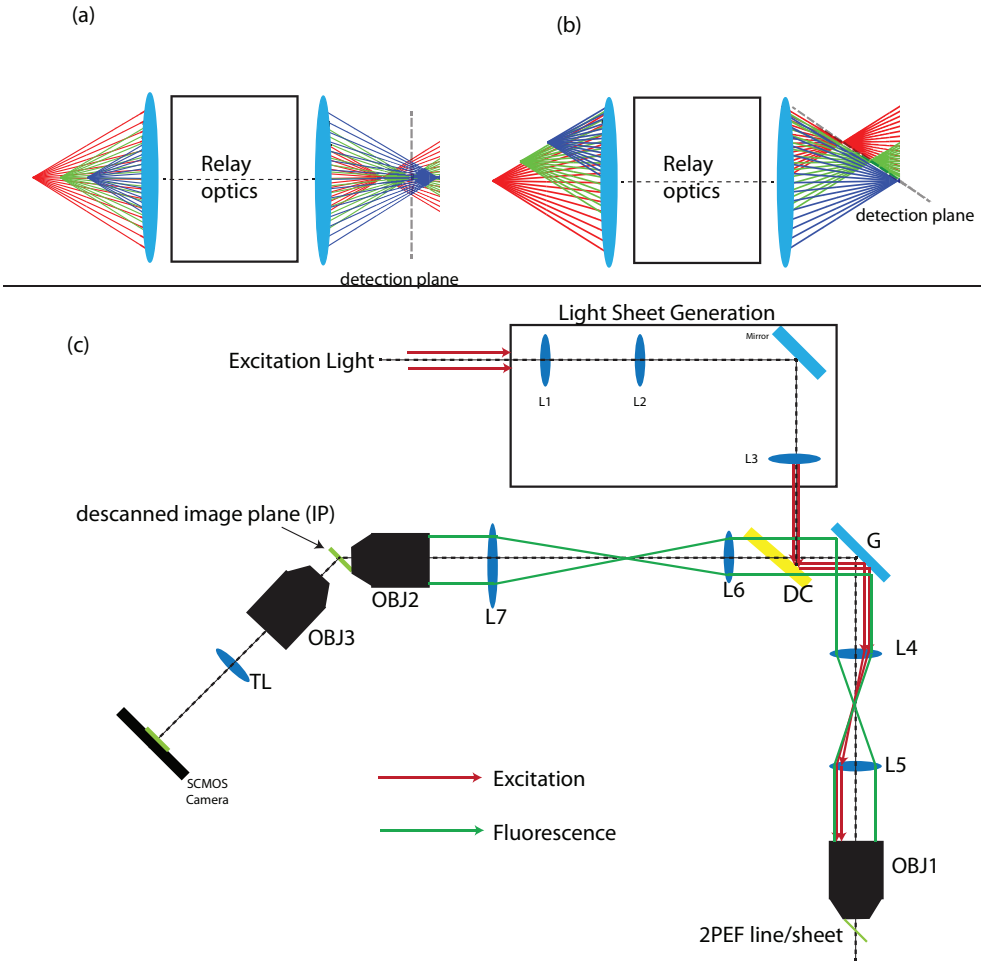

Figure 44: Optical sectioning and experimental setup.

(a) A ray trace for an imaging system with a magnification of -1, where the excitation is along the optical axis. Each color represents a different axial location. A detector placed on the focal plane of the imaging lens cannot distinguish between the three axial object points and this system does not confer optical sectioning. (b) A ray trace of an imaging system with a magnification of -1, where the excitation is tilted with respected to the optical axis. Each axial location appears spatially separated on a detector placed at a tilted angle, and this system confers optical sectioning. (c) Experimental beam path that uses the SCAPE geometry. An oblique 2PEF line or sheet is generated by feeding in a decentered low NA beam into the objective. The fluorescent light is de-scanned and an intermediate image plane is formed at the plane IP. The plane IP is magnified an imaged using a camera. L1, L2 and L3 are cylindrical lenses used when sheet excitation is desired. All other lenses are chosen so that the magnification m from the focal plane of OBJ1 to the focal plane of OBJ2 is in the range $\pm(1 \text{ to } 1.33)$*. DC is a dichroic beam splitter that allows the separation of excitation light and the fluorescent light. Additional filters are used after OBJ3 to remove reflected excitation light.*

3.7 Comparing line and sheet excitation

To understand how to best implement two-photon excitation in SCAPE, we must extend our analysis to consider excitation beams in the form or axially-extended lines and sheets of light .It can be shown that, since the process of two-photon excitation squares the intensity I, the lateral 2PEF profile length l_x is $w_x/\sqrt{2}$ accounting for the fact that squaring a Gaussian function changes its width by a factor of $\sqrt{2}$. The peak two-photon signal scaling with the lateral dimensions of the sheet are then given by the following.

$$S_{T,focus} \propto \frac{\sigma_{2p}}{f\tau l_x^2 l_y^2} P_0^2 T \quad (3.11)$$

Here l_x and l_y are the $1/e^2$ radii of the 2-photon excited fluorescence profile in the x and y dimension respectively. In order to generate a 2PEF line excitation that is ~300 μm along the z-axis, the lateral width has to be expanded so that $l_x = l_y \sim 5\ \mu m$. This value was computed from the Gaussian beam model presented above. Similar results can be obtained using the equations presented by Zipfel et al. [27]

One way to excite a plane is to drag the axially extended line across as shown in figure 45. Alternately, a sheet can be formed by expanding l_y by a factor of N. There are then two methods of achieving the same volume-rate. In one method, an axially extended line is scanned in two-dimensions to acquire a single volume. In the second method, a sheet excitation profile is scanned in one dimension to image a single volume.

The trade-offs in these two-cases can be compared in the following way using equation 3.11. The following arguments assume that the laser repetition rate is a constant 80 MHz between the considered cases. First, assume an axially extended line is excited by average power P_1 for an

integration time T_1 yielding a peak 2PEF signal of S_1. This line can be scanned to sequentially acquire a sheet-like region as shown in figure 45(b) and (c). To achieve this, the step size must be equal to half the FWHM of the line. Then scanning a line with FWHM of 5.3 μm to cover a 400 μm lateral width will require $2N$ steps, where N= $\frac{field\ of\ view}{beam\ lateral\ FWHM} \approx 75$. This will also require a time of $2N * T_1$ to scan a single plane. If a single plane is acquired

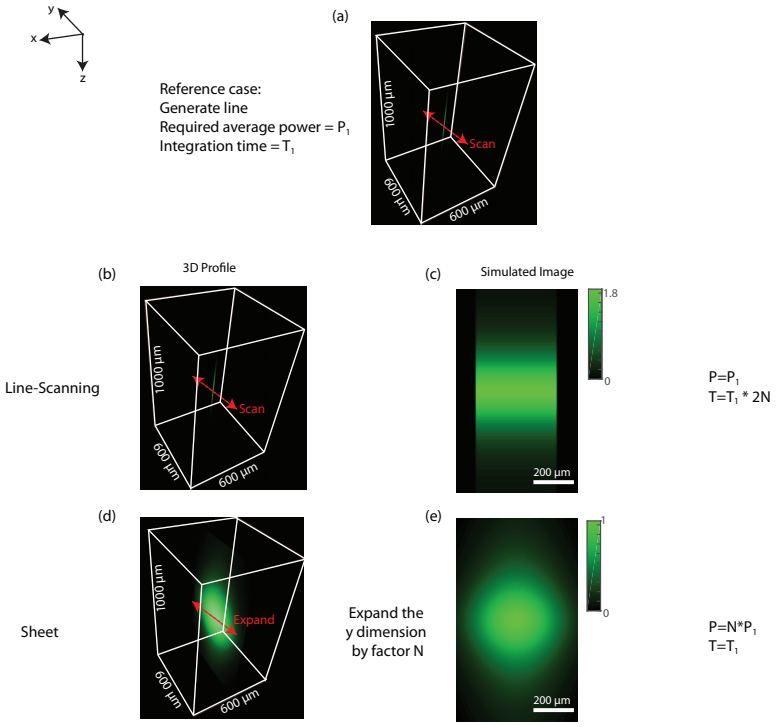

Figure 45: Comparison of line and sheet excitation (Numerical Simulation)

The relative differences of average power for line and sheet excitation was determined by numerically simulating a Gaussian beam. (a) Shows the reference image. A 2PEF line of lateral FWHM 5.3 µm was generated as the reference case. The fluorescence for one time unit in this case has a peak value of 1. (b) Scanning a line to image a plane. The simulated line was scanned with step size equal to half the lateral FWHM. (c) The simulated camera image from line-scanning. (d) The line was expanded into a sheet by expanding the y dimension by a factor of 75.4. The average power had to be increased by the same factor to maintain the 2PEF signal. Sheet excitation allows imaging a single plane in a fraction of the time it takes the line to scan a plan. Sheet excitation however requires a lot more power and results in a lateral profile that is Gaussian. $\lambda = 800\ nm, n = 1.33$.

with total integration time of T, and with the same signal S_1 per voxel, then the integration time per line is $T/(2N)$, and the average power will have to be increased to $P_1 * \sqrt{2N}$. If the same

frame-rate is to be achieved with sheet excitation by setting the sheet integration time to T, the line will have to be expanded by a factor of N as shown in figure 45(d) and (e). In this case, the average power must be increased by a factor of N in order to maintain the 2PEF signal per voxel of S_1. Then, at the same volume-rate, sheet excitation requires $\sqrt{N}$ times more average power compared to the line-excitation case at fixed laser repetition rate.

Given that line excitation is less expensive in terms of average power, this has been previously been determined the best solution for fast two-photon imaging. For example Truong et. al [89] combined a line excitation scheme with two-photon Selective Plane Illumination Microscopy (SPIM) to achieve a volumetric imaging rate ~0.04 Hz while imaging a volume of 254 x 570 x200 μm^3 in fly embryo. The above results were obtained with average power $P_0 \approx 200\ mW$ with a Ti:Sapphire laser ($f_l \approx 80\ MHz, \tau_p \sim 140\ fs$).

Using the above as a reference, the feasibility of line and sheet excitation can be discussed. With a standard Ti:Sapphire ($f_l \approx 80\ MHz$), it should be possible to perform line excitation with average power $P_0 \sim 100\ mW$ albeit at low volume rates. At $f_l \approx 80\ MHz$, there is no benefit to sheet excitation as such a scheme require more average power to achieve the same frame-rate, and the average power requirements become prohibitively high.

However, an alternative approach is suggested by equation 3.11 by treating the repetition rate as a variable. For the case of axial line excitation, the scan speed must be $\sim 1\ MHz$ in order to achieve 10 Hz volume rate. It is then possible to lower the repetition rate to increase the 2PEF signal collected in a time interval T, with $1\ MHz$ being the lower limit. For example, lowering the repetition rate f by a factor of N while keeping the average power P_0 and the integration time T constant yields a factor of N improvement in the generate 2PEF signal. For sheet excitation, in

order to achieve a ~10 Hz volume rate, the camera frame-rates of only ~1 kHz are required. Then, for sheet excitation, the laser repetition rate can be lowered down to the kHz range.

In both of these cases, lowering the repetition rate will yield more signal in line with equation 3.11 in the absence of saturation, photobleaching and photodamage. A realistic concern when following the strategy of lowering the laser repetition rate is that at fixed average power, the fluence $\mathbb{F} = \frac{P_0}{f_l A}$ increases as the inverse of the laser repetition rate and care must be taken to maintain fluence values below saturation and damage thresholds.

Finally, while the equation 3.11 and the example simulations shown in figure 45 assume an on-axis setup, these arguments still apply to off-axis excitation as demonstrated experimentally in section 3.8.

3.7.1 Axially-extended line Excitation Experiments

Preliminary experiments were carried out with line excitation in order to determine the achievable imaging speeds with a standard Ti:Sapphire (Mai Tai HP, Spectra Physics, parameters $f_l \approx 80\ MHz$ and $\tau_p \sim 100$ fs). For a low NA line corresponding approximately to the one shown in figure 45, the acquired images are shown in figure 46.

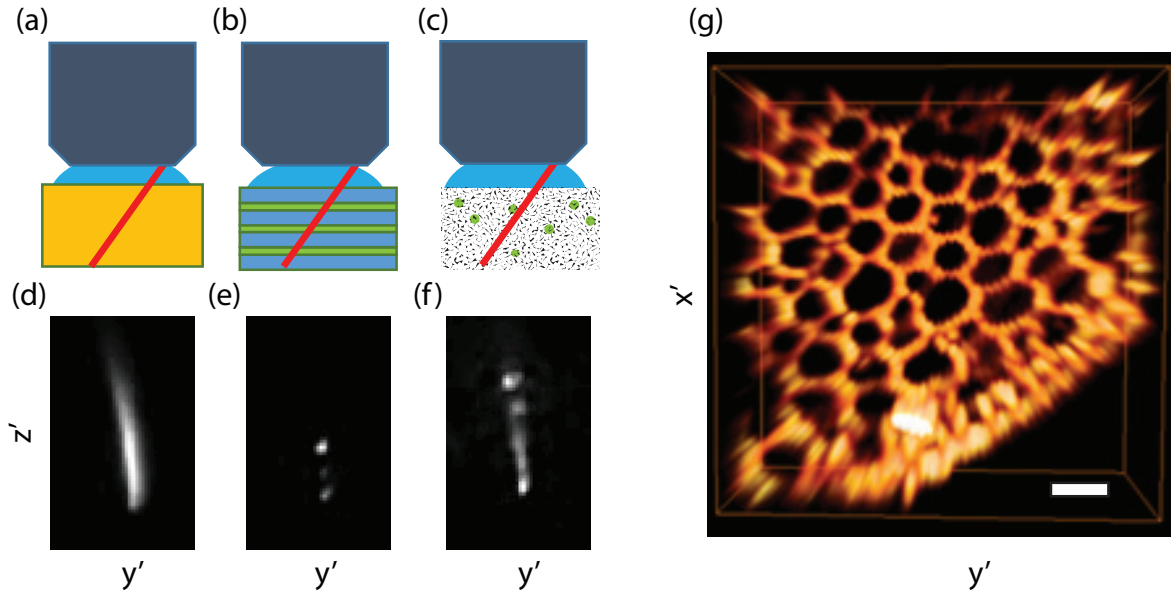

Figure 46: Volumetric 2PEF imaging with line excitation.

(a), (b) and (c) shows sample setups demonstrating optical sectioning ability and (d), (e) and (f) show the corresponding images on the camera. (a) Bulk fluorescence sample. (b) Sample with fluorescein layered in-between #1 coverslips. (c) Scattering phantom with 4 μm diameter beads in epoxy and intralipid. The optical sectioning ability is evident in images (e) and (f) that show different depth sections resolved. (g) shows a volume rendering of a stained convalaria sample. The sampling was 100x100 steps laterally and the integration time for each step was 0.4 ms yielding a volume rate of 0.25 Hz. λ~780 nm, $P_0 =$ 71 mW $f_l \approx 80\ MHz, \tau_p \sim 100\ fs$. Scalebar = 20 μm.

For the axially extended line with a $f_l = 80\ MHz$ laser, the typical values of average power required to achieve a signal that significantly exceeds the camera background with sub millisecond integration times was in the order of $100\ mW$. This is consistent with the results obtained by Truong et al.[89]. In addition to the above, imaging was performed in in-vivo mouse brain (not shown) with intravenously injected dextran-conjugated Fluorescein, achieving a volume imaging rate of 0.1 Hz over a 314x628x290 μm volume with 200x200x800 $pixel^3$ sampling with $P_0 =$ $200\ mW$ and $f_l \approx 80\ MHz$.

The volume-rate achieved above is a factor of 100 smaller than the desired volume-rate of 10 Hz. For the above, a camera was used as a detector here as it is part of the SCAPE geometry. However, the ideal detector to achieve imaging with axial line excitation is a photo-multiplier tube array or a silicon photomultiplier array capable of detecting weak signals while also providing large

($\sim MHz$) temporal bandwidth. Another way to achieve faster imaging is by lowering the repetition rate as described above in order to achieve larger two photon signal at constant average power. For example, lowering the repetition rate from 80 MHz to 1 MHz at constant average power and integration time sould increase the 2PEF signal by a factor of 80.

3.8 Characterizing a variable repetition rate source for 2P-SCAPE

In order to explore axially extended line excitation at lower laser repetition rates, subsequent experiments were conducted using a laser source with a tunable pulse repetition rate (16W Spirit laser from Spectra Physics). The laser operates at a wavelength of 1040 nm with $\tau_p \sim 400\ fs$. The laser repetition rate can be switched between 1 MHz and 400 kHz at constant average power ~16 W. Lower pulse repetition rates down to single shot are accessible through an on-board pulse-picker. These parameters are not ideal for biological imaging as longer pulse durations will increase thermal damage, while 1040 nm is both heavily absorbed by water and is inefficient for exciting standard fluorophores. However, using this laser allowed the testing of assumptions about both repetition rate and the feasibility of using line and sheet excitation in SCAPE.

The following experiment was set up to test the possibility of achieving axially extended line excitation at various repetition rates. As mentioned previously, the challenge of fast two-photon imaging is in increasing the 2PEF signal without incurring detrimental effects such as saturation and photodamage.

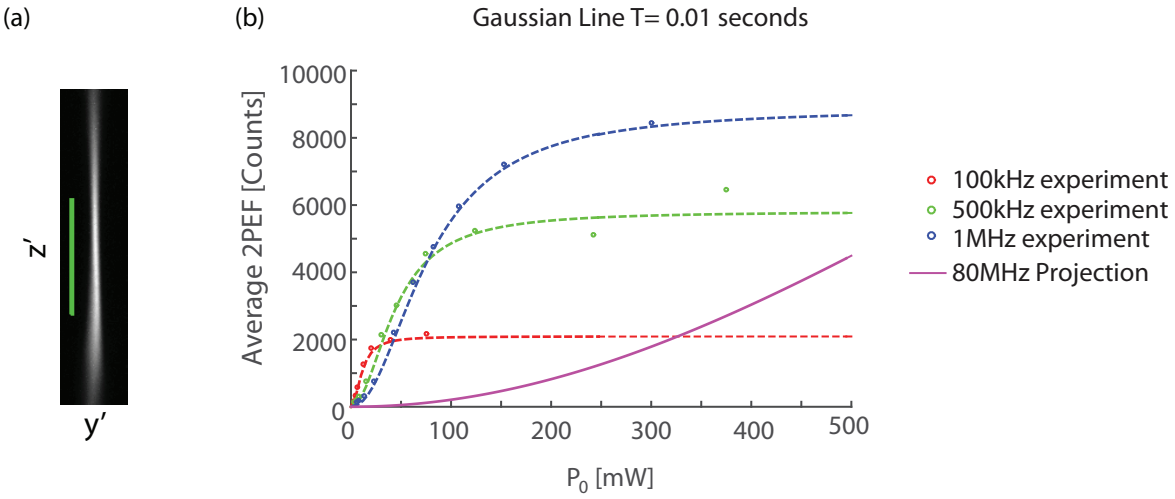

Figure 47: Saturation behavior for line excitation (experiment)

(a) Camera image of the line excitation profile. (b) The average 2PEF signal plotted against average power at the sample P_0 for several laser repetition rates. The repetition rate was changed using electronic pulse picking thus the spatial profile of the excitation beam is the same for all cases. The circles are measurements and dotted lines are fit to the model $S = K_1 \frac{P_0^2}{1+\frac{P_0^2}{P_{Sat}^2}}$. The solid curve is a projected curve for $f_l = 80\ MHz$. $\lambda = 1040$ nm. All measurements performed in 15 μM Rhodamine B. Objective1 NA =1. Objective3 NA=0.4. Camera: Andor Zyla (sCMOS). Camera integration time=0.01 seconds. All measurements were performed in steady state (several seconds after turning ont e laser shutter). Each data point is an average over 10 camera frames acquired at with 0.1 second intervals. Scalebar =155 μm.The variation of the 2PEF signal with average power at the sample P_0 was measured in a solution of 15μM Rhodamine-B. The particular dye was chosen as demonstrate good two photon absorption ($\sigma_{2P} = 25.5\ GM$ [18]) at the laser wavelength of 1040 nm. Experiments were performed by creating an oblique Gaussian line with a lateral 2PEF width (FWHM) of 8.37 μm as shown in Figure 47(a). The average signal in the line was measured as a function of average power at the sample for several pulse repetition rates between 100 kHz and 1 MHz. The variation signal traces are shown in figure 47 (b).

The variation of the 2PEF signal with average power at the sample P_0 was measured in a solution of $15\mu M$ Rhodamine-B. The particular dye was chosen as it demonstrates good two-photon absorption ($\sigma_{2P} = 25.5\ GM$ [18]) at the laser wavelength of 1040 nm. Experiments were performed by creating an oblique Gaussian line with a lateral 2PEF width (FWHM) of 8.37 μm as shown in Figure 47(a). The average 2PEF signal in the line was measured as a function of average power at the sample for several pulse repetition rates between 100 kHz and 1 MHz with a camera integration time of 0.01 seconds. The variation of signal traces are shown in figure 47 (b).

Results show that the signal saturates for $P_0 < 100\,mW$ for all measured repetition rates. Saturation is indicated by the deviation from the power-squared law and the data were fitted to a saturation model of the form $S = K_1 \frac{P_0^2}{1+\frac{P_0^2}{P_{sat}^2}}$ [19].

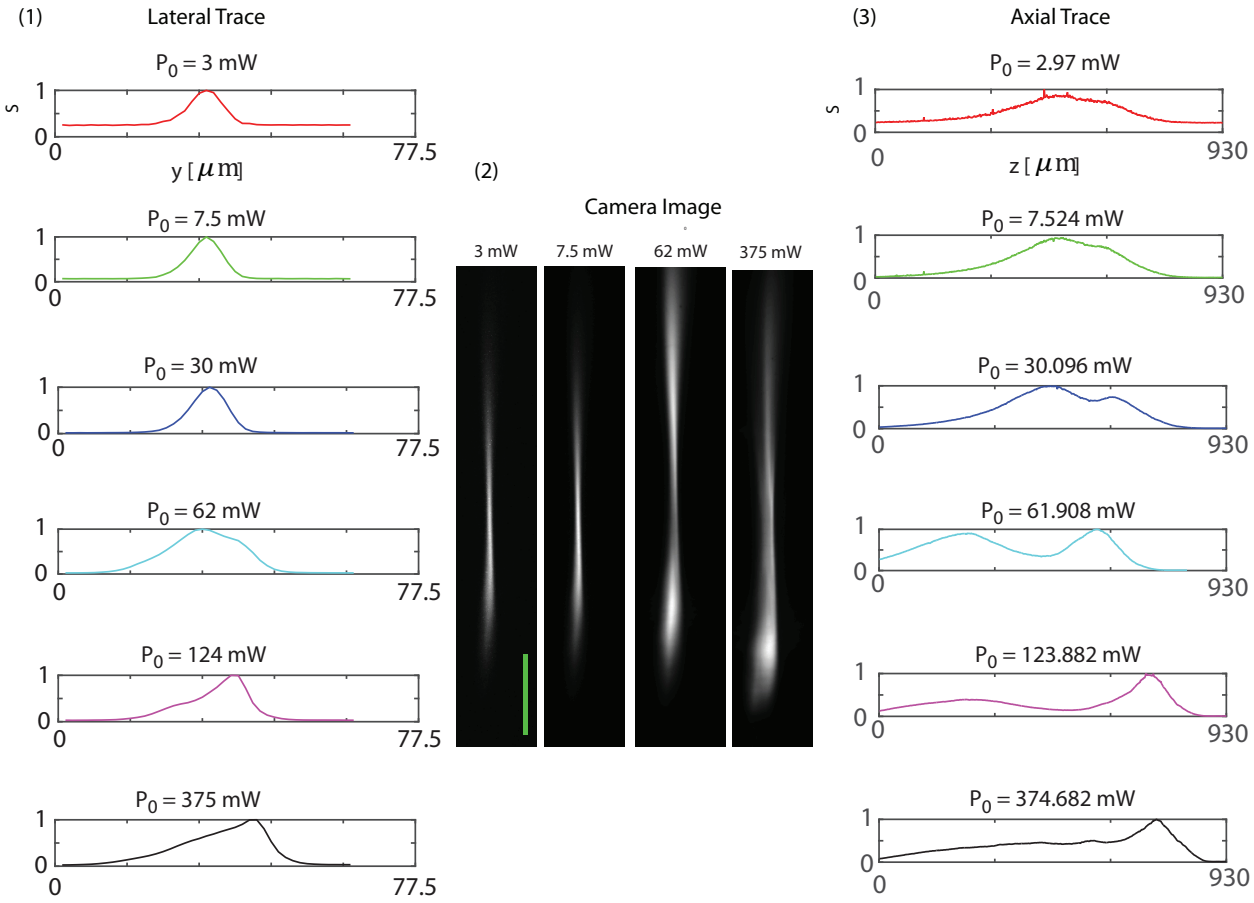

Figure 48: Excitation volume changes under strong excitation (Experiment).

Excitation patterns (average over 10 frames acquired at 0.1 second intervals) for various P_0 values at $f_l = 500$ kHz. Column (1) shows the lateral beam profile while columns (2) and (3) show the camera images and the axial beam profile respectively. The excitation profile becomes wider when P_0 exceeds 30 mW. $f_l = 500$ kHz. $\lambda = 1040$ nm. . $\tau_p \sim 400fs$. All measurements performed in 15 μM Rhodamine B. Scalebar = 155 μm.

In the range of repetition rates considered, $f_l = 1\,MHz$ provides the highest 2PEF signal. While operating at high power yields more signal, the excitation profile changes significantly. The expansion of the point-spread-function is expected under saturation and has been described previously [27]. Figure 48 shows the excitation profiles for $f_l = 500\,kHz$. The axial excitation

profile is seen to change at $P_0 = 30\,mW$ at the onset of saturation, which corresponds to $\mathbb{F}\sim 1\,nJ/\mu m^2$.

As shown in figure 47(b), operating at $f_l = 1\,MHz$ at $\mathbb{F}\sim 1\,nJ/\mu m^2$ ($P_0 \approx 70\,mW$) with an integration time $T = 0.01\,seconds$ yields approximately 4000 camera counts with the axially extended line configuration. The background counts on the camera are 103 at an integration time T=0.01 seconds and was found to be the same at T=10 μs. Useful data can be extracted provided the signal exceeds the background. Then imaging can be still performed with the above laser and sample parameters with a lower camera integration time of $500\,\mu s$, which would yield to 200 counts on the camera. These settings still only yields a volume-rate of 0.2 Hz at 100x100 x-y sampling, which is 50 times slower than the desired volume imaging rate. However, it should be noted that ignoring the camera background, which is believed to be caused by dark noise, and operating at the limit of the dynamic range of the camera (1 count per pixel), it would be possible, in principle, to achieve a line integration time of 2.5 μs corresponding to a volume-rate of 10 Hz. This hypothesis should be explored in future using a detector that can detect low light levels, such as a photo-multiplier array. Since the laser source provided access to kHz repetition rates, in subsequent experiments, sheet excitation profiles were tested.

3.8.1 Testing the feasibility of sheet-scanning 2P-SCAPE

.

3.8.1.1 *Comparison between lateral and axial sheet expansion*

The first aspect that was tested was the benefits of lateral and axial expansion of the two-photon profile. The benefit for axial expansion can be understood intuitively by considering the photon propagation direction and the orientation of the 2PEF excitation profile. In the disc-like lateral

excitation profiles used in wide-field temporal focusing [87], since the excitation profile is orthogonal to the beam propagation direction, a photon has only one opportunity become absorbed by a fluorephore. For an axial sheet on the other hand, since the sheet profile is extended along the direction of photon propagation, each photon has many opportunities to become absorbed. This advantage can be quantified analytically using properties of gaussian beams as follows.

According to equation 3.11, expanding the 2PEF profile by a factor of N laterally will require N times more power to maintain the same peak signal value. Recall the equation for a Gaussian light sheet intensity $I = \frac{2P_0}{\pi w_x(z) w_y(z)}$. If the width in the y-dimension is large enough to be considered to be collimated near the excitation region, then the beam width in that dimension can be considered constant so that, $I \approx \frac{2P_0}{\pi w_x(z) w_{0y}}$. Then the axial variation of the 2PEF profile, which scales as I^2, will have an axial FWHM $l_z = \frac{n\pi w_{0x}^2}{\lambda_0}$. Since the lateral 2PEF profile width is proportional to the beam width as shown above, $l_z \propto \frac{n\pi l_x^2}{\lambda_0}$ and $l_y \propto w_{0y}^2$. The peak 2PEF signal can be expressed in terms of the sheet dimensions in the y-dimension and the z-dimension.

$$S_{T,focus} \propto \frac{\sigma_{2p}}{f\tau l_z l_y^2} P_0^2 T \quad (3.12)$$

According the equation 3.12, if the 2PEF profile is expanded axially by a factor of N, P_0 only has to be increased by a factor of $\sqrt{N}$ to maintain the signal, unlike that lateral expansion case, which required a power increase by a factor of N. Figure 49 shows an experiment that was conducted to verify the prediction of equation 3.12.

The experiment shown in figure 49 determined the 2PEF signal drop-off at constant average power for a light-sheet expanded laterally vs. axially. The axial extent was controlled by changing the

beam width along the x-dimension. Analysis revealed that for axial expansion, the 2PEF signal drops off as $1/l_y^{1.95}$ while for axial expansion the 2PEF signal drops off as $1/l_z^{0.53}$ where l_y and l_z are the axial and lateral lengths of the sheet. The experimental scaling for axial expansion differs by a power of 0.5 compared to equation 3.12. This discrepancy can be explained in terms of the experimental setup. Equation 3.12 describes the peak 2PEF signal. On the other hand, the experimental setup measures the energy incident on a pixel of the camera. The numerical aperture of the 3rd objective was ~0.4 and the x dimension of the sheet is imaged using the axial direction of the 3rd objective. The experimental setup then does not measure the peak value right at the center of the sheet but measures some thickness which defined by the axial point-spread-function of the detection arm. Because the axial depth-of-focus ($\frac{\lambda n_{air}}{NA^2} \approx 3.5\,\mu m$) of the 3rd objective is comparable to the sheet thickness, the experiment result deviates from equation 3.12. Numerical simulations performed using the Gaussian beam model described above, and integrating along the x-dimension yields a signal drop-off factor of $1/l_z^{0.5}$ for axial expansion of the sheet, in good agreement with the experiment. Then expanding the sheet along the axial dimension provides an advantage over lateral expansion.

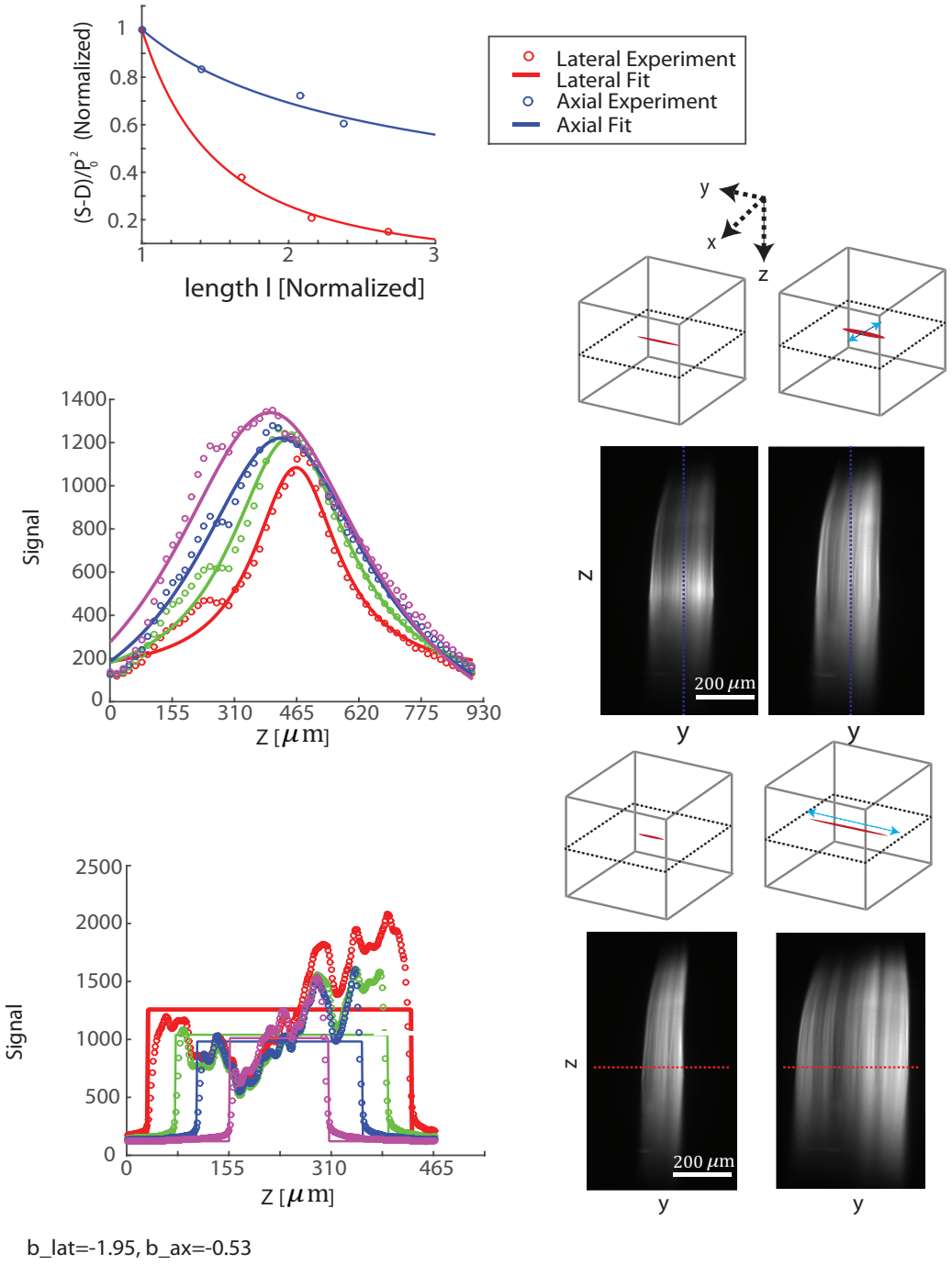

Figure 49: 2PEF signal scaling with lateral vs axial expansion of the excitation profile (Experiment).

A 2PEF sheet was generated. The sheet length in the axial dimension changed and the average power was changed to compensate for the change of signal. Similar experiment was performed for sheet expansion in the y dimension. Based on a power law fit, 2PEF signal for y expansion scales as $1/(length)^{1.95}$. *For axial expansion, the signal scales as* $1/(length)^{0.53}$. . $\lambda = 1040$ *nm. All measurements performed in 15 µM Rhodamine B. S=Signal, D=Dark counts.*

3.8.1.2 *Volumetric imaging with sheet excitation*

The scaling of the average 2PEF signal vs. average power in 15μM Rhodamine B for sheet excitation was then studied experimentally for the sheet profile shown in figure 50(a). As shown in (b), none of the experimental measures for the sheet show showed signs of saturation. The experiments reveal that, unlike the line excitation case, it is possible to achieve signal levels that far exceed the camera background with sheet excitation even with 1 ms integration time with average power levels less than 200 mW. Note that an integration time of 1 ms allows camera frame-rates ~kHz and imaging volume-rates ~10 Hz. Several other experiments were performed to compare imaging at various laser repetition rates.

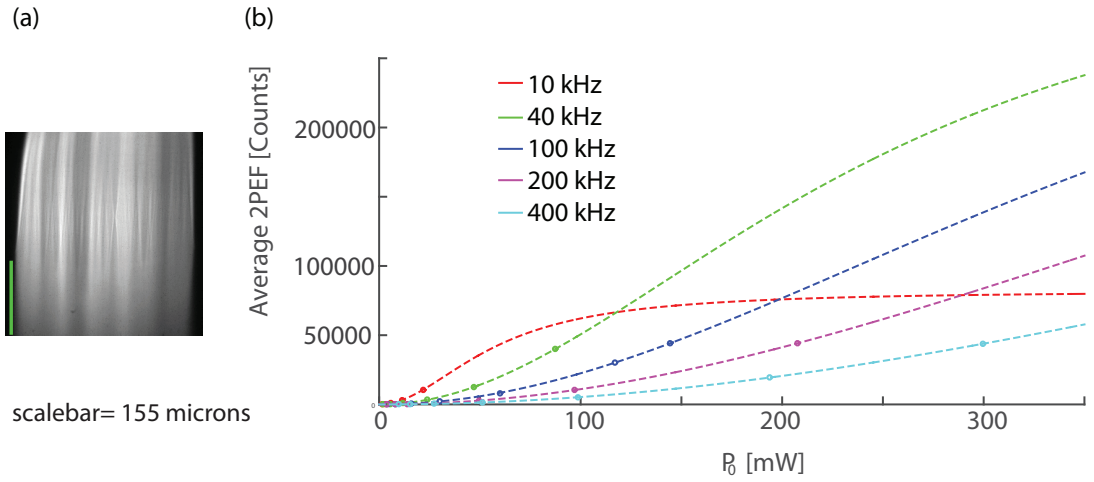

Figure 50: 2PEF signal vs. average power for varying pulse repetition rates (experiment)

(a) Camera image of the sheet excitation profile. (b) The average 2PEF signal plotted against average power at the sample P_0 for several laser repetition rates. The repetition rate was changed using electronic pulse picking thus the spatial profile is of the excitation beam is the same for all cases. The circles are measurements and dotted lines are fits to the model $= K_1 \frac{P_0^2}{1+\frac{P_0^2}{P_{sat}^2}}$. $\lambda = 1040\ nm$. . $\tau_p \sim 400 fs$. All measurements performed in 15 µM Rhodamine B. Objective1 NA =1. Objective3 NA=0.4. Camera: Andor Zyla (sCMOS). Camera integration time=0.01 seconds. All measurements were performed in steady state (several seconds after opening the laser shutter). Each data point is an average over 20 camera frames acquired at 0.1 second intervals. Scalebar= 155 µm.

3.8.1.3 *Photobleaching and Photodamage*

For this section, all experiments were carried on sample made of layers of agar and $15\mu M$ Rhodamine-B placed in-between layers of fluorinated ethylene propylene (FEP), which has a refractive index close to water. The laser parameters were λ =1040 nm with $\tau_p \sim 400\ fs$.

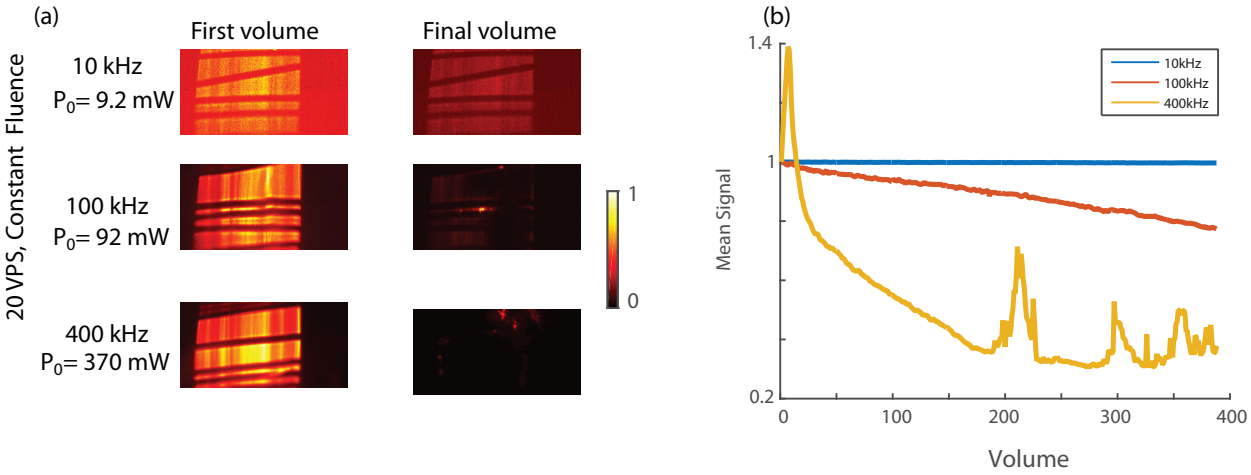

Figure 51: Photodamage and photobleaching propensity variation with pulse repetition rate f_l at the constant pulse energy.

(a) First (left) and last frame of the dataset at various pulse repetition rates. (b) The variation of mean signal during data acquisition (each curve has been independently normalized). The repetition laser repetition rate was changed through pulse-picking and hence the pulse energy is constant for all three cases with the average power changed.. The sample exhibited rapid degradation when imaging at $f_l = 400\ kHz$ and showed signs of photobleaching for $f_l = 100\ kHz$. $\lambda = 1040\ nm$. $\tau_p \sim 400 fs$. Sample: 15 μM Rhodamine B layered in FEP. Shown images are mean intensity projections to the y-z' plane. Camera framerate ~ 1 kHz

Figure 51 shows an experiment where the sample was imaged using different repetition rates but the same pulse energy of 0.92 μJ and same fluence $\mathbb{F} \sim 0.4\ nJ/\mu m^2$. For all experiements, the sheet length along y was 368 μm. The sheet length along x is not directly known but is estimated to be 8 μm at the waist based on the axial length of the sheet. Imaging was performed at approximately 20 Hz volume-rate with a camera frame-rate $\sim 1\ kHz$. At constant pulse energy, higher repetition rates provide higher signal. However, imaging at $f_l = 400\ kHz$ yielded obvious photodamage with $P_0 = 370\ mW$, for the laser parameters and the sample used for the experiment and $f_l = 100\ kHz$ with $P_0 = 92\ mW$ showed signs of significant photobleaching.

A second experiment was conducted where the 2PEF signal was held approximately constant (within an error of 25%) by changing the average power P_0 while imaging at various laser repetition rates. This experiment directly compares the effects of operating the microscope at different laser repetition rates. The camera framerate was $\sim 100\ Hz$. As shown in figure 52, for $f_l = 10\ kHz$ and $\mathbb{F} \sim 1 \frac{nJ}{\mu m^2}$, photodamage was observed, as determined by changes in the sample and signal decay over time. No photodamage was observed for $f_l = 100\ kHz$ and $400\ kHz$ (corresponding to $\mathbb{F} \sim 0.34 \frac{nJ}{\mu m^2}$ and $0.2 \frac{nJ}{\mu m^2}$).

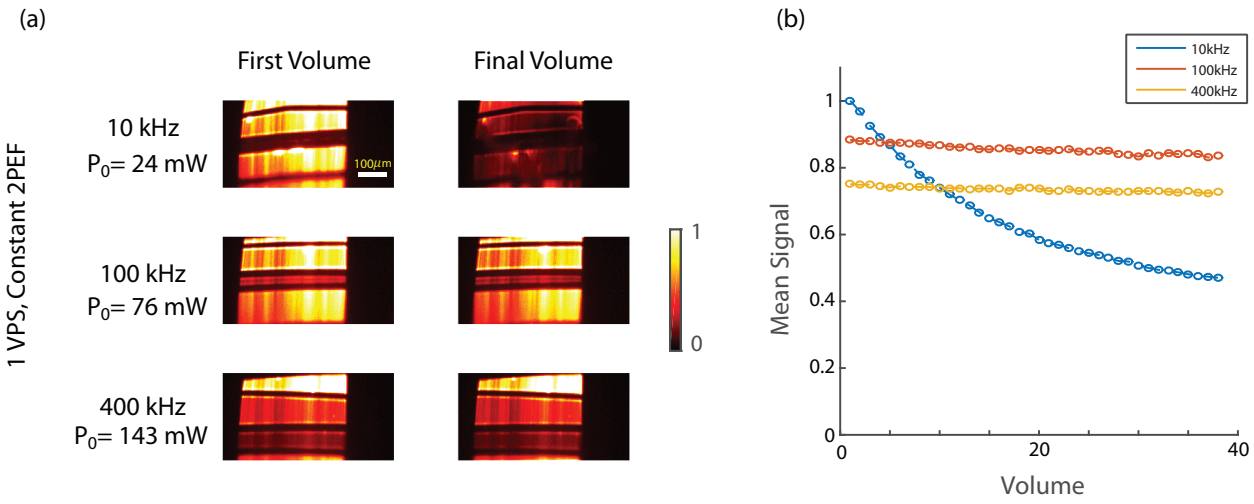

Figure 52: Photodamage and photobleaching propensity variation with pulse repetition rate f_l at approximately the same 2PEF signal

Each imaging run was performed at a different laser repetition rate. 2PEF signal was maintained to be approximately constant by changing the average power. Camera framerate= 100 Hz, $f_l = 10\ kHz$ yields photodamage while $f_l = 100\ kHz$ and $400\ kHz$ showed no signs of photodamage. $\lambda = 1040\ nm$. $\tau_p \sim 400 fs$. Sample: 15 µM Rhodamine B layered in FEP. Shown images are mean intensity projections to the y-z plane. Columns on the left show the first show mean intensity projections to the y-z' plane. Camera framerate ~ 100 Hz.

The results of all the photobleaching and photodamage experiments are shown in Table 3. Based on these results, it was determined that imaging at $\mathbb{F} \geq 0.4 \frac{nJ}{\mu m^2}$ yielded visible photodamage or photobleaching. Imaging at $f_l = 100\ kHz$ balances the fluence as well as the average power with adequate signal to image at high volume rates.

Table 3: Photobleaching and Photodamage Experiments

f_l	P_0	$\mathbb{F}$	**Frame-rate**	**Issues**
10 kHz	9.2 mW	~0.4 $nJ/\mu m^2$	~1 kHz	Low signal
100 kHz	92 mW	~0.4 $nJ/\mu m^2$	~1 kHz	Photobleaching
400 kHz	370 mW	~0.4 $nJ/\mu m^2$	~1 kHz	Photodamage/photobleaching
10 kHz	24 mW	~1 $nJ/\mu m^2$	~100 Hz	Photodamage/photobleaching
10 kHz	26 mW	~1 $nJ/\mu m^2$	~1 kHz	Photobleaching
100 kHz	76 mW	~0.3 $nJ/\mu m^2$	~100 Hz	none
400 kHz	143 mW	~0.2 $nJ/\mu m^2$	~100 Hz	none
100 kHz	75 mW	~0.3 $nJ/\mu m^2$	~1 kHz	none

3.8.1.4 *Imaging at 20 Hz volume-rate*

Fast volumetric imaging could be achieved using sheet-scanning 2P-SCAPE at $f_l = 100\ kHz$ and $\mathbb{F}\sim 0.34\frac{nJ}{\mu m^2}$ with no photodamage and negligible photobleaching as shown in figure 53. The sample was constructed with layered Rhodamine B and FEP as described above and the imaged volume was 210x378x310 μm^3 with the camera framerate ~ 1 kHz. The sampling density was 51*200x400 $pixel^3$ with a total run-time of 20 seconds. Achieving the same signal at 10 kHz required increasing the fluence to $\mathbb{F}\sim 1\frac{nJ}{\mu m^2}$, which yielded photobleaching. Then $f_l \approx 100\ kHz$ appears to be the optimal repetition rate for sheet-excitation for the sample and the laser parameters described above.

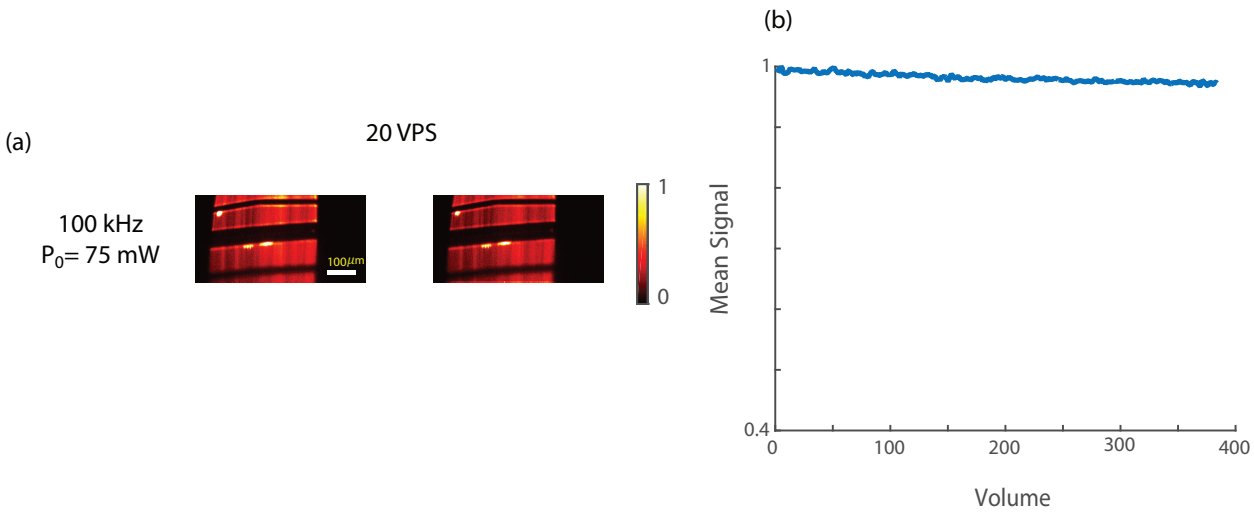

Figure 53: Imaging at 20 Hz volume-rate with no photodamage and negligible photobleaching.

Imaging at $f_l = 100\ kHz$ allows high SNR images to be acquired a 20 Hz volume-rate with $P_0 < 100\ mW$ with no visible photodamage and negligible photobleaching. Shown images are mean intensity projections to the y-z plane. Sample: 15 μM Rhodamine B layered in FEP. $f_l = 100\ kHz$. $\lambda = 1040\ nm$. $\tau_p \sim 400 fs$.

3.9 Discussion

The results obtained in the experiments presented in this chapter indicate that sheet excitation at a laser repetition rate of approximately 100 kHz yields volumetric imaging rates of 20 Hz in a non-scattering sample over a 210x378x310 μm^3 volume. In this case, imaging was achieved with negligible photobleaching and no visible photodamage with average laser power of less than 100 mW over a 20 second duration. These experiments lay the foundation for future experiments in mouse brain imaging. While the mechanism of the photodamage was observed in the experiments is not obvious, both photodamage and photobleaching was correlated with high fluence.

Initial tests suggest that avoiding photodamage in the mouse brain will require a better optimized laser source. Both the excitation wavelength and the pulse-width for these experiments were non-optimal and were limited by the laser source. The wavelength of 1040 nm yields significantly stronger absorption from water than the more commonly used wavelength range of 800- 920 nm.

In addition, the pulse width used for these experiments were in the order of $400\ fs$. A tunable light source with a large enough spectral bandwidth to achieve short ($\tau_P < 100\ fs$) such as an Optical Parametric Amplifier (OPA), will allow experiments with lower pulse-widths at wavelengths with much lower water absorption. Neglecting saturation, lowering the pulse width by a factor N will increase the 2PEF by a factor N at fixed average power.

The above experiments were performed using samples made up of dye solutions at physiological concentrations. The results can be used to estimate system performance when imaging vessels with injected dyes. More experiments are needed to obtain the performance of fluorophores such as GFP and GCaMP that are used to study the structure and function of neurons. One of the main challenges with the sheet excitation approach as well as other widefield two-photon approaches is that visible spectrum fluorescent light will undergo heavy scattering within the mouse brain. Since the experiments performed above were conducted in non-scattering samples, no information exists about how scattering effects the formation and the imaging of the sheet excitation profile. Hence, imaging performance in the presence of scattering should be characterized in future work. Fluorophores with red-shifted emission profiles might offer a way of mitigating some of the scattering effects [90].

For the axially extended line excitation experiments, testing the possibility of achieving fast volume-rates was hindered by the use of an sCMOS camera as a substitute linear detector, as the signal levels fell below the camera background for the short integration times needed for x-y raster scanning. Even with sufficient signal to noise, a camera does not provide the necessary temporal bandwidth (e.g. a maximum of 26 kHz rather than the 1 MHz per line for a 300 x 300 x-y scan) to record data and hence is ill-suited for a line-excitation setup. It is possible that using a photo-multiplier device that provides high gain will allow the determination of the limits of linear 2P-

SCAPE in future experiments. Potential feasibility of this configuration is supported by recently reported experiments performed by Lu et al. [72] which suggest that Bessel-line excitation combined with a photo-multiplier detector scheme can yield fast volumetric imaging, albeit integrated over all depths rather than being depth-resolved. Nevertheless, presented results suggest that an axially-extended beam can generate sufficient photons for depth-resolved detection without exceeding photodamage limits. In addition to using a more suitable detector technology, linear-SCAPE could also benefit from optimization of the detection arm of the SCAPE setup for line excitation, for example by direct-detection of the intermediate image plane rather than secondary image rotation optics that are required to generate a high quality 2D image for sheet-scanning. Linear detection relaxes this image quality requirement since depth is spatially encoded in the descanned arm, but x-y resolution is primarily governed by the excitation beam exciting a small volume (as in Lu et al). In such a setup, each array element would detect a different depth in the sample with axial resolution requirements relaxed in the case of using a linear detector array with fewer elements than a camera – e.g. using 16 elements to cover a 400 micron depth range would yield 16 depths each covering a 25 micron thick depth plane. Using a linear detector further offers the ability to tune the gain applied to different depths to account for variations of signal due to scattering can provides an advantage over using a camera. In addition, line excitation can be combined with a confocal slit to provide background reduction, reducing the effects of emission light scattering in the same way as line-scanning confocal and recent synchronous camera line read-out SPIM approaches [91, 92]. Comparing the scaling between resolution, power and two-photon signal when using Bessel-like beams might also reveal whether there is an advantage to using such a scheme rather than the Gaussian beam setup used above.

Summary and Future Directions

This dissertation studied two ways of optimizing two-photon excited fluorescence for volumetric biological imaging. Wavefront correction with Zernike functions resulted in fluorescence improvements in the 40-100% range as well as improvement in resolution. One of the important characteristics of these corrections is that they remain useful for hundreds of microns inside the brain, which means that a single correction can be used to image a whole volume. This scheme could easily be improved by including more Zernike modes in the optimization. A drawback of modal optimization is that the correction modes can have cross-talk which would mean that it is not possible to independently measure the effect of each optimization mode. Given this, it would be possible to construct a system that uses modal optimization to perform a quick optimization process which is then further supplemented with a slower local optimization. Recent demonstration of wavefront-sensing [37] in the mouse brain is also of importance and it would be interesting to compare wavefront sensing to wavefront-sensorless optimizations.

The system demonstrated in Chapter 2 performs wavefront correction as well as wavefront encoding. Given the recent interest in utilizing two-photon excitation combined with wavefront encoding for optogenetic stimulation, combining wavefront with wavefront correction would be an easy next step. Since a typical correction is valid over a volume, the optogenetic stimulation efficiency could potentially be improved over a volume.

In terms of improving the volumetric imaging speed of two-photon microscopy via SCAPE-type imaging geometries, we developed models and tested their predictions using different laser sources

and optical configurations to test the feasibility of this approach. We found that a sheet excitation 2P-SCAPE setup proved to be compatible with camera based detection setup utilized in the above experiments. It was also determined that the sheet excitation approach used here, which extends the imaging area along the axial direction rather than laterally, is far more energetically efficient compared to wide-field two-photon excitation as used in multi-focal and temporal focusing systems. This result is due to the fact that extending the sheet in the axial direction provides each photon multiple chances to be absorbed by a fluorophore. On the other hand, in wide-field two-photon microscopy, the profile is extended laterally and this advantage is not present. The trade-offs between the two situations were demonstrated analytically and numerically using a Gaussian beam model and confirmed experimentally. Using a laser source with a 100 kHz repetition rate, we demonstrated that it was possible to image at 20 Hz volume-rate with pulse energies ~1 μJ in a non-scattering sample. Achieving volume imaging in scattering samples would require accounting for the attenuation introduced by scattering. Imaging a mouse brain at similar repetition rates and pulse energies with $\lambda \approx 800\, nm$ with τ_p~$100\, fs$ with sheet excitation is expected to yield promising results, as the shorter pulse width will yield much higher peak power with similar pulse energies (up to 4 x more signal), while water absorption would be significantly lower compared to 1040 nm. Testing using an intravenously injected dye initially would enable the concentration and volume of the dye to be controlled, prior to imaging genetically encoded fluorophores. This configuration could be further improved by reducing losses in the SCAPE detection arm to improve detection NA, paving the way for imaging in scattering samples.

The use of a camera as the detector prevented testing the ultimate limit of line excitation and the scheme merits more investigation in future experiments. As mentioned in the Discussion in Chapter 3, the use of a photo-multiplier array would provide the ability to detect low light levels

and should provide the higher temporal bandwidth that is required to perform volume imaging with a line excitation setup. Some of the effects of scattering could be mitigated by using line excitation with a spatial filter. Finally, using a Bessel-like beam instead of a Gaussian beam might provide improvements. A numerical and experimental study comparing Bessel beam excitation for long ($\sim 500\ \mu m$) depth of focus could enable comparison of how resolution, 2PEF signal and power scale in a Bessel beam, with the final goal of achieving fast 2PEF imaging of calcium transients in the mouse brain.

Publications and presentations related to this dissertation

Peer-reviewed journal publications:

- P. T. Galwaduge, S. H. Kim, L. E. Grosberg, and E. M. C. Hillman, "Simple wavefront correction framework for two-photon microscopy of in-vivo brain", Biomed. Opt. Express 6, 2997-3013 (2015). https://doi.org/10.1364/BOE.6.002997

- Claure N. Lunardi, Anderson J. Gomes, Sandeep Palepu, P. Thilanka Galwaduge, Elizabeth M.C. Hillman, "PLGA nano/microparticles loaded with cresyl violet as a tracer for drug delivery: Characterization and insitu hyperspectral fluorescence and 2-photon localization", Materials Science and Engineering: C, Volume 70, Part 1, 1 January 2017, Pages 505-511. DOI:10.1016/j.msec.2016.09.020

Conference presentations and abstracts:

- P. T. Galwaduge, Hang Yu, Venkatakaushik Voleti, Kripa Patel, Wenze Li, Elizabeth M. Hillman. "Single and two-photon swept confocally aligned planar excitation (SCAPE) microscopy for high-speed 3D imaging of neural activity". SPIE BiOS, January 2017. [Talk]

- P. T. Galwaduge, H. Yu, K. Patel, V. Voleti, M. A. Shaik, E. M. C. Hillman, "Towards Two-Photon Swept Confocally Aligned Planar Excitation Microscopy (2P-SCAPE)", Optics and the Brain. Optical Society of America, 2016. [Talk] https://doi.org/10.1364/BRAIN.2016.BTu2D.5

- A. Tsao, P. T. Galwaduge, S. Kim, M. A. Shaik, and E. M. Hillman, "Measuring the thermodynamic effects of neurovascular coupling in the awake, behaving mouse brain", Optics and the Brain. Optical Society of America, 2016. [Poster] https://doi.org/10.1364/CANCER.2016.JW3A.19

- P. T. Galwaduge, S. H. Kim, L. E. Grosberg, and E. M. Hillman, "Simple Signal-Based Wavefront Correction for In-Vivo Two-Photon Microscopy in Mouse Brain", in Optics in the Life Sciences. Optical Society of America, 2015. [Talk] https://doi.org/10.1364/BRAIN.2015.BrW3B.3

- P. Galwaduge, S. H. Kim, L. E. Grosberg, E. M. C. Hillman, "Signal-based adaptive optics two-photon microscopy of in-vivo mouse brain", Neuroscience 2014. Society for Neuroscience, 2014. [Poster]

- P. T. Galwaduge, L. E. Grosberg, and E. M. Hillman, "Signal-Based Adaptive Optics Optimization for in-vivo Two-Photon Microscopy of the Brain", Biomedical Optics. Optical Society of America, 2014. [Poster] https://doi.org/10.1364/BIOMED.2014.BT3A.10s

Bibliography

1. Grosberg, L.E.a.R., Andrew J. and Asfaha, Samuel and Wang, Timothy C. and Hillman, Elizabeth M. C., *Spectral Characterization and Unmixing of Intrinsic Contrast in Intact Normal and Diseased Gastric Tissues Using Hyperspectral Two-Photon Microscopy.* PLoS ONE, 2011. **6**(5): p. e19925.

2. McCaslin, A.F.H., et al., *In vivo 3D morphology of astrocyte-vasculature interactions in the somatosensory cortex: implications for neurovascular coupling.* J Cereb Blood Flow Metab, 2011. **31**(3): p. 795-806.

3. Chen, T.-W., et al., *Ultrasensitive fluorescent proteins for imaging neuronal activity.* Nature, 2013. **499**(7458): p. 295-300.

4. Nakai, J., M. Ohkura, and K. Imoto, *A high signal-to-noise Ca2+ probe composed of a single green fluorescent protein.* Nat Biotech, 2001. **19**(2): p. 137-141.

5. St-Pierre, F., et al., *High-fidelity optical reporting of neuronal electrical activity with an ultrafast fluorescent voltage sensor.* Nat Neurosci, 2014. **17**(6): p. 884-889.

6. Saleh, B.E. and M.C. Teich, *Fundamentals of photonics. 2007.* Wiley Series in Pure and Applied Optics, Wiley. **10**: p. 0471213748.

7. Siegman, A.E., *Lasers.* Mill Valley, CA, 1986. **37**: p. 462-466.

8. Goodman, J.W. and S.C. Gustafson, *Introduction to fourier optics.* Optical Engineering, 1996. **35**(5): p. 1513-1513.

9. Goodman, D.S., *Theory and Practice of Scanning Optical Microscopy.* Journal of the Optical Society of America A, 1987. **4**(3): p. 551-552.

10. Mertz, J., *Introduction to optical microscopy*. Vol. 138. 2010: Roberts.

11. Wilson, T. and C. Sheppard, *Theory and practice of scanning optical microscopy*. Vol. 180. 1984: Academic Press London.

12. Theer, P. and W. Denk, *On the fundamental imaging-depth limit in two-photon microscopy.* Journal of the Optical Society of America A, 2006. **23**(12): p. 3139-3149.

13. Lunardi, C.N., et al., *PLGA nano/microparticles loaded with cresyl violet as a tracer for drug delivery: Characterization and in-situ hyperspectral fluorescence and 2-photon localization.* Materials Science and Engineering: C, 2017. **70**: p. 505-511.

14. Xu, C. and W.W. Webb, *Multiphoton excitation of molecular fluorophores and nonlinear laser microscopy*, in *Topics in fluorescence spectroscopy*. 2002, Springer. p. 471-540.

15. Göppert-Mayer, M., *Über elementarakte mit zwei quantensprüngen.* Annalen der Physik, 1931. **401**(3): p. 273-294.

16. Kaiser, W. and C. Garrett, *Two-photon excitation in Ca F 2: Eu 2+*. Physical review letters, 1961. **7**(6): p. 229.

17. Denk, W., J. Strickler, and W. Webb, *Two-photon laser scanning fluorescence microscopy.* Science, 1990. **248**(4951): p. 73-76.

18. The Developmental Resource for Biophysical Imaging Opto-Electronics , C.U. *Two-photon action cross sections*. 2017 [cited 2017 06/22/2017]; Available from: http://www.drbio.cornell.edu/cross_sections.html.

19. Kirkpatrick, S.M., R.R. Naik, and M.O. Stone, *Nonlinear saturation and determination of the two-photon absorption cross section of green fluorescent protein.* The Journal of Physical Chemistry B, 2001. **105**(14): p. 2867-2873.

20. Jackson, J.D., *Electrodynamics*. 1975: Wiley Online Library.

21. Shi, L., et al., *Transmission in near-infrared optical windows for deep brain imaging.* Journal of biophotonics, 2016. **9**(1-2): p. 38-43.

22. Jacques, S.L., *Optical properties of biological tissues: a review.* Physics in medicine and biology, 2013. **58**(11): p. R37.

23. Boyd, R., *Nonlinear optics.* 1992.

24. Hillman, E.M.C., *Optical brain imaging in vivo: techniques and applications from animal to man.* Journal of Biomedical Optics, 2007. **12**(5): p. 051402-051402-28.

25. Chen, Z., et al., *Extending the fundamental imaging-depth limit of multi-photon microscopy by imaging with photo-activatable fluorophores.* Opt. Express, 2012. **20**(17): p. 18525-18536.

26. Ellen Robey, S.R. *1-photon vs. 2-photon*. Available from: http://mcb.berkeley.edu/labs2/robey/content/2-photon-imaging.

27. Zipfel, W.R., R.M. Williams, and W.W. Webb, *Nonlinear magic: multiphoton microscopy in the biosciences.* Nat Biotech, 2003. **21**(11): p. 1369-1377.

28. Spectra-Physics, *Mai Tai User Manual*. 2003.

29. Born, M., et al., *Principles of Optics: Electromagnetic Theory of Propagation, Interference and Diffraction of Light*. 1987: Pergamon Press.

30. Mahajan, V.N., *Aberration theory made simple*. Vol. 6. 1991: SPIE Press.

31. Vellekoop, I.M. and A. Mosk, *Focusing coherent light through opaque strongly scattering media.* Optics letters, 2007. **32**(16): p. 2309-2311.

32. Ji, N., T.R. Sato, and E. Betzig, *Characterization and adaptive optical correction of aberrations during in vivo imaging in the mouse cortex.* Proceedings of the National Academy of Sciences, 2011.

33. Tang, J., R.N. Germain, and M. Cui, *Superpenetration optical microscopy by iterative multiphoton adaptive compensation technique.* Proceedings of the National Academy of Sciences, 2012.

34. Wang, C., et al., *Multiplexed aberration measurement for deep tissue imaging in vivo.* Nat Meth, 2014. **11**(10): p. 1037-1040.

35. Wang, K., et al., *Rapid adaptive optical recovery of optimal resolution over large volumes.* Nat Meth, 2014. **11**(6): p. 625-628.

36. Aviles-Espinosa, R., et al., *Measurement and correction of in vivo sample aberrations employing a nonlinear guide-star in two-photon excited fluorescence microscopy.* Biomedical Optics Express, 2011. **2**(11): p. 3135-3149.

37. Wang, K., et al., *Direct wavefront sensing for high-resolution in vivo imaging in scattering tissue.* Nature communications, 2015. **6**.

38. Ji, N., D.E. Milkie, and E. Betzig, *Adaptive optics via pupil segmentation for high-resolution imaging in biological tissues.* Nat Meth, 2010. **7**(2): p. 141-147.

39. Cornea, A. and P.M. Conn, *Fluorescence Microscopy: Super-Resolution and other Novel Techniques*. 2014: Elsevier.

40. Debarre, D., et al., *Image-based adaptive optics for two-photon microscopy.* Opt. Lett., 2009. **34**(16): p. 2495-2497.

41. Zeng, J., et al., *3D resolved mapping of optical aberrations in thick tissues.* Biomed. Opt. Express, 2012. **3**(8): p. 1898-1913.

42. Binding, J., et al., *Brain refractive index measured in vivo with high-NA defocus-corrected full-field OCT and consequences for two-photon microscopy.* Optics Express, 2011. **19**(6): p. 4833-4847.

43. Facomprez, A.e.l., E. Beaurepaire, and D. D\'{e}barre, *Accuracy of correction in modal sensorless adaptive optics.* Opt. Express, 2012. **20**(3): p. 2598-2612.

44. Navarro, R., J. Arines, and R. Rivera, *Direct and inverse discrete Zernike transform.* Optics express, 2009. **17**(26): p. 24269-24281.

45. Tsai, P., et al., *Spherical aberration correction in nonlinear microscopy and optical ablation using a transparent deformable membrane.* Applied Physics Letters, 2007. **91**(19): p. 191102.

46. Xu, C. and W.W. Webb, *Measurement of two-photon excitation cross sections of molecular fluorophores with data from 690 to 1050 nm.* Journal of the Optical Society of America B, 1996. **13**(3): p. 481-491.

47. Katz, O., et al., *Focusing and compression of ultrashort pulses through scattering media.* Nat Photon, 2011. **5**(6): p. 372-377.

48. Brainard, D.H., *The psychophysics toolbox.* Spatial vision, 1997. **10**: p. 433-436.

49. Pelli, D.G., *The VideoToolbox software for visual psychophysics: transforming numbers into movies.* Spatial Vision, 1997. **10**(4): p. 437-442.

50. Kleiner, M., D. Brainard, and D. Pelli, *What's new in Psychtoolbox-3?*, in *What's new in Psychtoolbox-3?* 2007.

51. Cooper, P.R., *Refractive-index measurements of paraffin, a silicone elastomer, and an epoxy resin over the 500-1500-nm spectral range.* Appl Opt, 1982. **21**(19): p. 3413-5.

52. Booth, M.J., M.A.A. Neil, and T. Wilson, *Aberration correction for confocal imaging in refractive-index-mismatched media.* Journal of Microscopy, 1998. **192**(2): p. 90-98.

53. Booth, M.J. and T. Wilson, *Strategies for the compensation of specimen-induced spherical aberration in confocal microscopy of skin.* Journal of Microscopy, 2000. **200**(1).

54. Popoff, S.M., et al., *Measuring the Transmission Matrix in Optics: An Approach to the Study and Control of Light Propagation in Disordered Media.* Phys. Rev. Lett., 2010. **104**: p. 100601.

55. Nimmerjahn, A., et al., *Sulforhodamine 101 as a specific marker of astroglia in the neocortex in vivo.* Nat Meth, 2004. **1**(1): p. 31-37.

56. Masamoto, K., et al., *Repeated longitudinal in vivo imaging of neuro-glio-vascular unit at the peripheral boundary of ischemia in mouse cerebral cortex.* Neuroscience, 2012. **212**(0): p. 190-200.

57. Mathiesen, C., et al., *Spontaneous calcium waves in Bergman glia increase with age and hypoxia and may reduce tissue oxygen.* J Cereb Blood Flow Metab, 2013. **33**(2): p. 161-169.

58. Nikolenko, V., et al., *SLM Microscopy: Scanless Two-Photon Imaging and Photostimulation with Spatial Light Modulators.* Frontiers in Neural Circuits, 2008. **2**.

59. Packer, A.M., et al., *Two-photon optogenetics of dendritic spines and neural circuits.* Nat Meth, 2012. **9**(12): p. 1202-1205.

60. Yang, W., et al., *Simultaneous Multi-plane Imaging of Neural Circuits.* Neuron. **89**(2): p. 269-284.

61. Rickgauer, J.P., K. Deisseroth, and D.W. Tank, *Simultaneous cellular-resolution optical perturbation and imaging of place cell firing fields.* Nat Neurosci, 2014. **17**(12): p. 1816-1824.

62. Arrenberg, A.B., F. Del Bene, and H. Baier, *Optical control of zebrafish behavior with halorhodopsin.* Proceedings of the National Academy of Sciences, 2009. **106**(42): p. 17968-17973.

63. Packer, A.M., et al., *Simultaneous all-optical manipulation and recording of neural circuit activity with cellular resolution in vivo.* Nat Meth, 2015. **12**(2): p. 140-146.

64. Fienup, J.R., *Phase retrieval algorithms: a comparison.* Applied Optics, 1982. **21**(15): p. 2758-2769.

65. Gerchberg, R.W., *A practical algorithm for the determination of phase from image and diffraction plane pictures.* Optik, 1972. **35**: p. 237.

66. Whyte, G. and J. Courtial, *Experimental demonstration of holographic three-dimensional light shaping using a Gerchberg–Saxton algorithm.* New Journal of Physics, 2005. **7**(1): p. 117.

67. Shabtay, G., *Three-dimensional beam forming and Ewald's surfaces.* Optics communications, 2003. **226**(1): p. 33-37.

68. Maschio, M.D., et al., *Simultaneous two-photon imaging and photo-stimulation with structured light illumination.* Opt. Express, 2010. **18**(18): p. 18720-18731.

69. Thibos, L.N., PhD, et al., *Standards for reporting the optical aberrations of eyes.* Journal of Refractive Surgery, 2002. **18**(5): p. S652--60.

70. Erickson, M.J., *Introduction to combinatorics*, in *Wiley-Interscience series in discrete mathematics and optimization*. 1996, Wiley: New York. p. 170-176.

71. Grosberg, L.E., B.R. Chen, and E.M.C. Hillman, *Simultaneous multiplane in vivo nonlinear microscopy using spectral encoding.* Opt. Lett., 2012. **37**(14): p. 2967-2969.

72. Lu, R., et al., *Video-rate volumetric functional imaging of the brain at synaptic resolution.* Nat Neurosci, 2017. **20**(4): p. 620-628.

73. Song, A., et al., *Volumetric two-photon imaging of neurons using stereoscopy (vTwINS).* Nat Meth, 2017. **14**(4): p. 420-426.

74. Kong, L., et al., *Continuous volumetric imaging via an optical phase-locked ultrasound lens.* Nature methods, 2015. **12**(8): p. 759-762.

75. Prevedel, R., et al., *Fast volumetric calcium imaging across multiple cortical layers using sculpted light.* Nat Meth, 2016. **13**(12): p. 1021-1028.

76. Bouchard, M.B., et al., *Swept confocally-aligned planar excitation (SCAPE) microscopy for high-speed volumetric imaging of behaving organisms.* Nat Photon, 2015. **9**(2): p. 113-119.

77. Kochkina, E., et al., *Modeling of the general astigmatic Gaussian beam and its propagation through 3D optical systems.* Applied Optics, 2013. **52**(24): p. 6030-6040.

78. Hawkes, P. and J.C. Spence, *Science of microscopy*. 2008: Springer Science & Business Media.

79. Cheng, L.-C., et al., *Measurements of multiphoton action cross sections for multiphoton microscopy.* Biomedical Optics Express, 2014. **5**(10): p. 3427-3433.

80. Diaspro, A., *Confocal and two-photon microscopy: foundations, applications and advances.* Confocal and Two-Photon Microscopy: Foundations, Applications and Advances, by Alberto Diaspro (Editor), pp. 576. ISBN 0-471-40920-0. Wiley-VCH, November 2001., 2001: p. 576.

81. Harris Lab, J.R.C. *Two-Photon Fluorescent Probes*. 2017 [cited 2017; Available from: https://www.janelia.org/lab/harris-lab-apig/research/photophysics/two-photon-fluorescent-probes.

82. Hopt, A. and E. Neher, *Highly nonlinear photodamage in two-photon fluorescence microscopy.* Biophysical journal, 2001. **80**(4): p. 2029-2036.

83. Macias-Romero, C., et al., *Wide-field medium-repetition-rate multiphoton microscopy reduces photodamage of living cells.* Biomedical Optics Express, 2016. **7**(4): p. 1458-1467.

84. Tsai, P.S., et al., *Plasma-mediated ablation: An optical tool for submicrometer surgery on neuronal and vascular systems.* Current opinion in biotechnology, 2009. **20**(1): p. 90-99.

85. Podgorski, K. and G. Ranganathan, *Brain heating induced by near-infrared lasers during multiphoton microscopy.* Journal of neurophysiology, 2016. **116**(3): p. 1012-1023.

86. Botcherby, E., R. Juškaitis, and T. Wilson, *Scanning two photon fluorescence microscopy with extended depth of field.* Optics communications, 2006. **268**(2): p. 253-260.

87. Schrodel, T., et al., *Brain-wide 3D imaging of neuronal activity in Caenorhabditis elegans with sculpted light.* Nat Meth, 2013. **10**(10): p. 1013-1020.

88. Radosevich, A.J., et al., *Hyperspectral in vivo two-photon microscopy of intrinsic contrast.* Opt. Lett., 2008. **33**(18): p. 2164-2166.

89. Truong, T.V., et al., *Deep and fast live imaging with two-photon scanned light-sheet microscopy.* Nat Meth, 2011. **8**(9): p. 757-760.

90. Dana, H., et al., *Sensitive red protein calcium indicators for imaging neural activity.* Elife, 2016. **5**: p. e12727.

91. Mei, E., et al., *A line scanning confocal fluorescent microscope using a CMOS rolling shutter as an adjustable aperture.* Journal of microscopy, 2012. **247**(3): p. 269-276.

92. De Medeiros, G., et al., *Confocal multiview light-sheet microscopy.* Nature communications, 2015. **6**.

Appendix

Gaussian Beam Equations:

The intensity of a Gaussian beam is given by [6]:

$$I(x,y,z) = \frac{2P_0}{\pi w^2(z)} \exp[-2\frac{(\mathrm{x}^2 + y^2)}{w^2(z)}]$$

Here P_0 is the power, $w(z)$ is the $1/e^2$ beam radius.

$$w(z) = w_0\sqrt{1 + \left(\frac{z}{z_0}\right)^2}$$

$$w_0 = \sqrt{\frac{\lambda z_0}{\pi}}$$

w_0 is the beam waist radius and z_0 is the Rayleigh range.